A Study of Lattice Dynamics in Iron-based Superconductors by Inelastic Light Scattering

Von der Fakultät Mathematik und Physik der Universität Stuttgart
zur Erlangung der Würde eines Doktors der Naturwissenschaften
(Dr. rer. nat.) genehmigte Abhandlung

vorgelegt von

Youngje Um
aus Busan (Südkorea)

Hauptberichter: Prof. Dr. Bernhard Keimer
Mitberichter: Prof. Dr. Harald Giessen
Tag der mündlichen Prüfung: 13. Dezember 2013

Max-Planck-Institut für Festkörperforschung

Stuttgart 2013

Max-Planck-Institut für Festkörperforschung

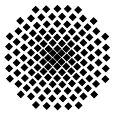

Universität Stuttgart

Abstract

A Study of Lattice Dynamics in Iron-based Superconductors by Inelastic Light Scattering

by

Youngje Um

Doctor of Philosophy in Physics
Max-Planck-Institut für Festkörperforschung, Stuttgart
Universität Stuttgart, Stuttgart
2013

After the discovery of high temperature (high T_c) superconductivity in copper oxide-based materials (cuprates) in 1986, this phenomenon was a unique property of the cuprates for more than 20 years. The origin of high T_c superconductivity is still under debate. In 2008, high T_c superconductivity was discovered in iron-based compounds. This discovery presents new opportunities for the development of a fundamental understanding of high T_c superconductivity. Density functional calculations indicate a weak electron-phonon coupling strength in iron-based superconductors and these suggest that superconductivity is not mediated by phonons. However, experimental report of a large isotope effect of the iron atoms on the superconductivity T_c suggests that phonons play an important role in iron-based superconductors.

Motivated by these findings, this thesis presents a Raman scattering study of the lattice dynamics of the iron-based superconductors $Fe_{1+y}Te_{1-x}Se_x$, LiFeAs and $NaFe_{1-x}Co_xAs$ as a function of chemical composition and temperature.

In $Fe_{1+y}Te_{1-x}Se_x$, an unconventional linewidth broadening of the c-axis polarized Fe phonon of B_{1g} symmetry is found with decreasing temperature, which indicates an unusual coupling between the phonon and iron excess-induced magnetic fluctuations in this compound.

In LiFeAs, the Raman scattering data provide evidence for a weak electron-phonon coupling, which is consistent with non-phonon mediated Cooper pairing in this compound.

In $NaFe_{1-x}Co_xAs$, upon cooling two features are observed: (i) an unconventional linewidth broadening of several phonons, which is indicative of spin fluctuation-phonon coupling, and (ii) a superconductivity-induced phonon lineshape renormalization, which can not be explained by standard model calculations.

Zusammenfassung

Eine Untersuchung der Gitterdynamik in eisenbasierten Supraleitern durch ineleastische Lichtstreuung

by

Youngje Um

Doktor der Naturwissenschaften
Max-Planck-Institut für Festkörperforschung, Stuttgart
Universität Stuttgart, Stuttgart
2013

Nach der Entdeckung der Hochtemperatursupraleitung in Kupferoxid-basierten Materialien (Kuprate) im Jahr 1986, war dieses Phänomen für mehr als 20 Jahre eine einzigartige Eigenschaft der Kuprate. Der Ursprung der Hochtemperatursupraleitung ist noch immer umstritten. Im Jahr 2008 wurde Hochtemperatursupraleitung in eisenbasierten Verbindungen entdeckt. Diese Entdeckung stellt neue Möglichkeiten für die Entwicklung eines fundamentalen Verständnisses der Hochtemperatursupraleitung bereit. Dichtefunktionalrechnungen ergeben eine schwache Elektron-Phonon Kopplungsstärke in eisenbasierten Supraleitern, was nahe legt, dass die Supraleitung nicht durch Phononen vermittelt wird. Jedoch zeigen Experimente einen starken Isotopen-Effekt der Eisen-Atome auf die supraleitende Sprungtemperatur T_c, was andeutet, dass Phononen doch eine wichtige Rolle in eisenbasierten Supraleitern spielen.

Motiviert von diesen Erkenntnissen, wird in der vorliegenden Doktorarbeit eine Untersuchung der Gitterdynamik der eisenbasierten Supraleiter $Fe_{1+y}Te_{1-x}Se_x$, LiFeAs und $NaFe_{1-x}Co_xAs$ als Funktion der chemischen Zusammensetzung und der Temperatur vorgestellt.

In $Fe_{1+y}Te_{1-x}Se_x$, wurde eine unkonventionelle Vergrößerung der Linienbreite des c-Achsen polarisierten Fe Phonons mit B_{1g} Symmetrie bei abnehmender Temperatur entdeckt, was eine außergewöhnliche Kopplung zwischen dem Phonon und den durch Eisenexzess induzierten magnetischen Fluktuationen in der Verbindung anzeigt.

In LiFeAs erbringen Raman-Streudaten den Nachweis für eine schwache Elektron-Phonon Kopplung, was mit der nicht-Phonon-vermittelten Cooper-Paarung in dieser Verbindung konsistent ist.

In $NaFe_{1-x}Co_xAs$ werden beim Abkühlen zwei Besonderheiten beobachtet: (i) Eine unkonventionelle Vergrößerung der Linienbreite mehrerer Phononen, was eine Spinfluktuations-Phononkopplung anzeigt und (ii) eine supraleitungsinduzierte Renormierung der Phonon-Linienform, die nicht durch Standardmodellrechnungen erklärt werden kann.

Contents

List of Figures

LIST OF FIGURES

LIST OF FIGURES

List of Tables

LIST OF TABLES

1

Introduction

1.1 Iron-based Superconductors

1.1.1 Discovery

Following the discovery of copper oxide-based superconductors (cuprates) in 1986 (6), high temperature (high T_c) superconductivity was believed to be unique in cuprates for more than 20 years. However, in 2008, $LaFeAsO_{1-x}F_x$ (T_c = 26 K) was discovered by Hosono and co-workers (7) as the first members of a new class of high T_c superconductors, so-called iron-based superconductors. So far, numerous families of iron-based superconductors such as REFeAs($O_{1-x}F_x$) (1111-family, RE = rare earth) (8, 9), $M$$Fe_2As_2$ (122-family, M = Ba, Ca, Sr, K, Cs ...) (10, 11), LiFeAs/NaFeAs (111-family) (12, 13) and $Fe_{1+y}Te_{1-x}Se_x$ (11-family) (14, 15, 16) have been found and investigated (see Fig. 1.1).

The discovery of superconductivity in iron-based compounds raises many questions about the origin of superconductivity. Historically, scientists have believed that magnetism easily destroys superconductivity (magnetic impurities are always pair-breaking for singlet superconductors). As a consequence, researchers have avoided using magnetic materials, in particular ferromagnetic materials, for exploration of new superconductors. Since the early 1970's, superconductivity next to a magnetic phase has been already found in several systems such as heavy fermions (material superconducting transition temperature $T_c^{max} \sim 2.3$ K), organics ($T_c^{max} \sim 33$ K) and cuprates ($T_c^{max} \sim 153$ K) quite before iron-based compounds, but it was at low temperature except for cuprates. Appearance of high T_c superconductivity in iron-based superconductors has

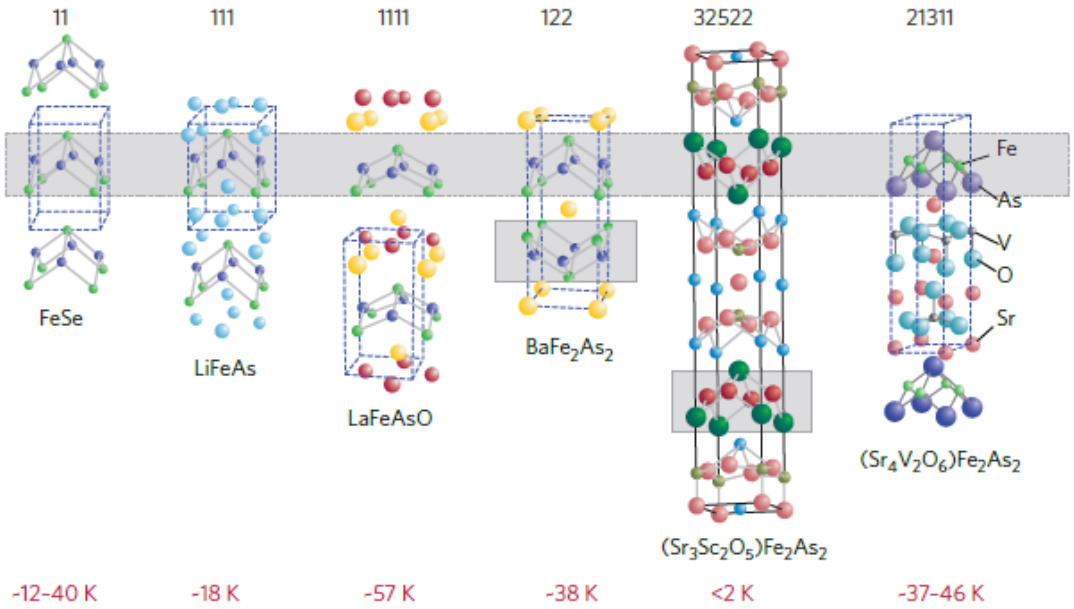

Figure 1.1: Iron based-superconductors - Various types of iron based-superconductors from Ref. (17). Highest achieved T_c for each family is listed below each structure.

indicated that our fundamental understanding in the origin of superconductivity is still lacking.

1.1.2 General Properties

Although there are various compounds of iron-based superconductors which can be classified into several families based on their chemical compositions as shown in Fig. 1.1, all iron-based superconductors share several common properties.

1.1.2.1 Crystallographic properties

First of all, the iron-arsenic (in general iron-pnictogen (P, As) or iron-chalcogen (S, Se, Te)) basal plane, which exhibits tetrahedral coordination of iron and arsenic atoms, is commonly shared in all iron-based superconductors (19). Iron atoms form a square lattice and occupy the central planar positions, and arsenic atoms occupy alternately the position above or below the iron plane (see Fig. 1.2(a)). In the real tetragonal unit cell, two iron and two arsenic atoms are present, but one can consider the primitive unit cell where one iron and one arsenic atoms are contained because of highly symmetric

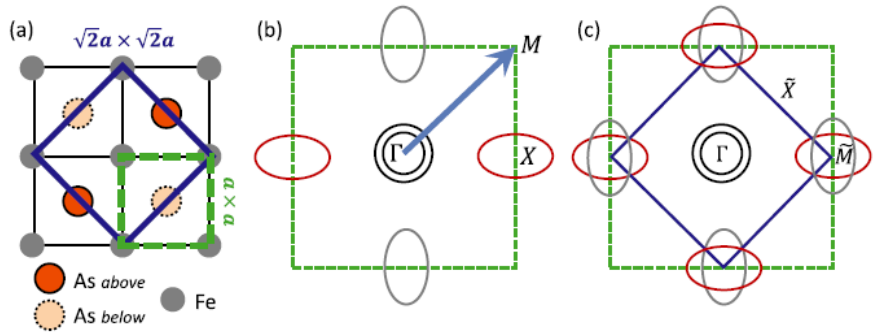

Figure 1.2: Unit cells of iron-based superconductors - Crystallographic and reciprocal unit cells of iron-based superconductors from Ref. (18). (a) Iron-arsenic lattice. The solid blue square is the real tetragonal unit cell where two iron and two arsenic atoms are contained. The dashed green square indicate the primitive unit cell containing one iron and one arsenic atoms. (b) Schematic 2D Fermi surface of 1-Fe(dashed green square) Brillouin zone. The Γ point (hole pockets) is at the center of the Brillouin zone and the X point (electron pockets) is at (π,0). (c) 2D Fermi surface of 2-Fe(solid blue square) Brillouin zone. The M point (electron pockets) is at (π,π).

positions of arsenic atoms. In this thesis, I am going to mainly use the 2-Fe real tetragonal unit cell notation. The corresponding schematic Fermi surfaces of both the tetragonal and primitive unit cells are sketched in Fig. 1.2(b)-(c) (18). All iron-based superconductors adopt the tetragonal structure at room temperature. As the materials are cooled down, the system undergoes structural phase transitions from the tetragonal structure to the orthorhombic structure, except for LiFeAs (see Chap. 4).

1.1.2.2 Electronic properties

As shown in Fig. 1.3, the initial band calculation by density functional theory (DFT) on $LaFeAsO_{1-x}F_x$ compound has predicted that the contribution of the iron 3d-orbital bands is dominant near the Fermi level and two electron pockets and two (or three) hole pockets are preset at M and Γ points in the tetragonal unit cell, respectively (20). Experimentally, such prediction has been confirmed by Angle-resolved photoemission spectroscopy (ARPES) measurement (see Fig. 1.3(d)-(f)). In addition, along (π,π), the Fermi surface nesting between the electron and hole pockets has been found in all iron-based superconductors (21, 22), and it is believed to be one of the main driving force for the spin-density wave (SDW) (23) and superconductivity in these materials (24).

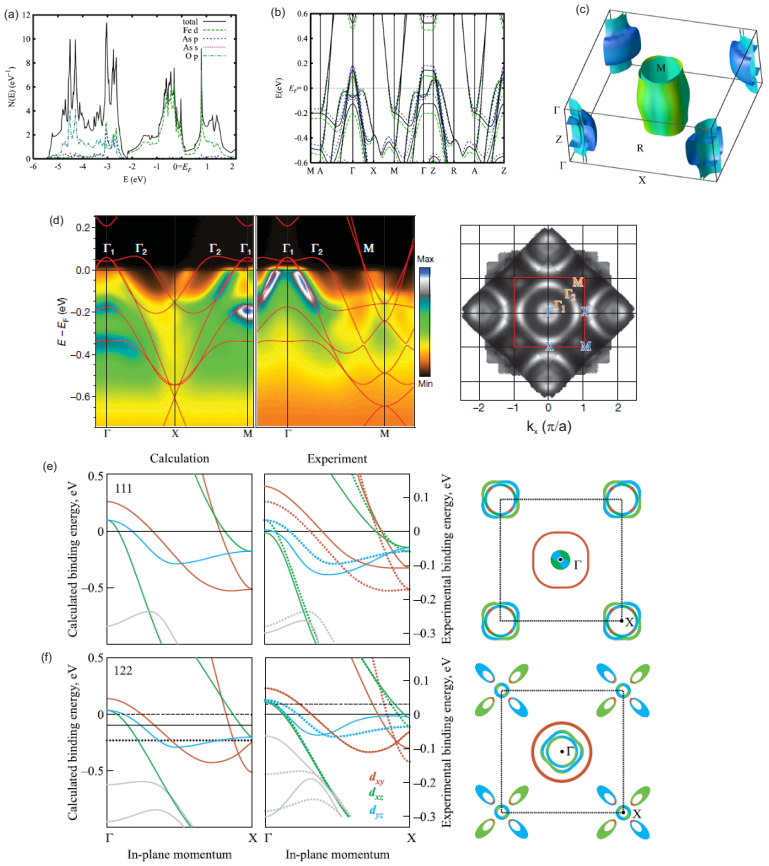

Figure 1.3: Electronic structure of iron-based superconductors - (a) DFT density of state (b) Band structure (c) Fermi surface of $LaFeAsO_{1-x}F_x$ from Ref. (20). The symmetry points are $\Gamma = (0,0,0), Z = (0,0,\pi), X = (\pi,0,0), R = (\pi,0,\pi), M = (\pi,\pi,0), A = (\pi,\pi,\pi)$. (d) ARPES data and Fermi surface map of LaFePO from Ref. (21). Two hole pockets at Γ point are derived from Fe-d_{xz}/d_{yz} bands (Γ_1) and $d_{3z^2-r^2}$ band (Γ_2). (e)-(f) Band calculation and ARPES data of LiFeAs and $BaFe_2As_2$ from Ref. (22). In cases of LiFeAs and $BaFe_2As_2$, Fe-d_{xy} and d_{xz}/d_{yz} bands are pronounced near the Fermi level.

1.1.2.3 Magnetic properties

- **Magnetic order**

The parent compounds of iron-based superconductors (except for LiFeAs) undergo antiferromagnetic (AFM) order (especially SDW) transition below magnetic transition temperature T_N. As shown in Fig. 1.4, the magnetic ordering vector is present along (π,π) in the tetragonal unit cell. Weak magnetic moment of 0.36 μ_B has been found at low temperature (26). The high temperature ($T > T_N$) paramagnetic state ex-

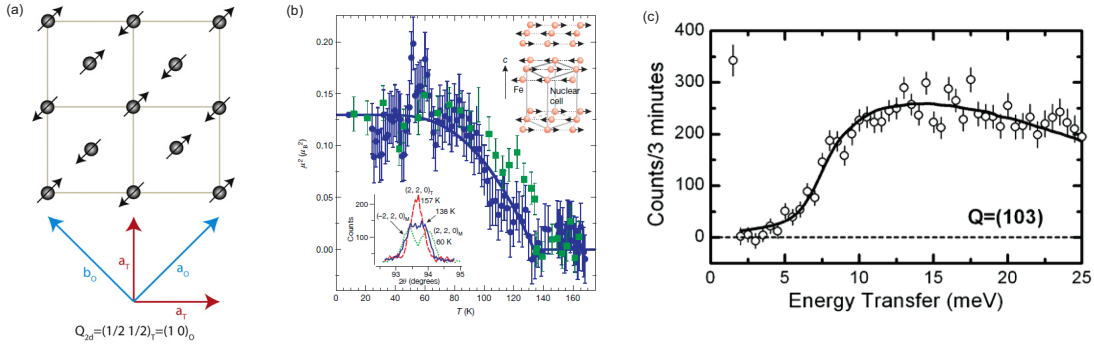

Figure 1.4: Magnetic structure of iron-based superconductors - (a) In-plane magnetic structure from Ref. (25). Collinear magnetic ordering vector is (π,π) in the tetragonal unit cell. It is equivalent to (π,0) in the orthorhombic unit cell. (b) Temperature dependence of magnetic Bragg peak from Ref. (26). (c) Magnetically scattered neutron intensity at Q_{AFM} = (1 0 3) in the orthorhombic notation from Ref. (27). The low-energy spin excitation is gapped with 7 meV.

hibits an unusual linear temperature dependence of the magnetic susceptibility χ (28). This linear behavior is characterized neither by Pauli- nor Curie-Weiss-paramagnetism. Instead, SDW moment fluctuation scenario (29) has been suggested for the linear dependence of the magnetic susceptibility.

The nature of the ordered state is one of the important topic in iron-based superconductors. It is commonly believed to be an itinerant SDW induced by Fermi surface nesting (23), as the magnetic ordering wave vector is consistent with the nesting vector. However, the magnetic frustration induced by nearest-neighbor and next-nearest-neighbor interactions between local Fe moments also provides an explanation for the structural transition and a small magnetic moment (30), and suggests the extent of a nematic phase slightly above T_N (31). In addition to the magnetic frustration model, a ferro-orbital ordering also has been proposed to account for the recently observed highly anisotropic magnetic coupling (32).

- **Spin dynamics**

In addition to the magnetic ground state, the magnetic excitation spectrum is also important issue in high T_c superconductors as it gives insights into the role of magnons in superconductivity. The spin dynamics of the materials has been revealed by inelastic neutron scattering (INS) experiments. In parent compounds, the low-energy

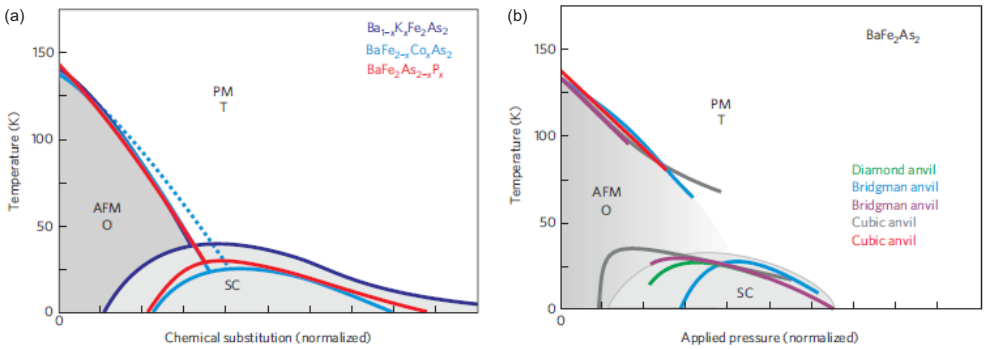

Figure 1.5: Phase diagram of iron-based superconductors - Phase diagram as a function (a) chemical doping (b) pressure from Ref. (19).

spin excitations are gapped with the spin-gap of 5 - 10 meV below T_N (33) (see also Fig. 1.4(c)). Above the spin-gap energy, the magnetic excitation peaks are centered at the AFM wave vector.

1.1.2.4 Superconducting properties

- **Phase diagram**

In iron-based superconductors, superconductivity can be achieved by chemical doping or applying pressure as shown in Fig. 1.5. Upon chemical doping or by applying pressure, superconductivity appears with suppressing AFM ordering, and superconducting transition temperature T_c reaches the maximum value. Then, T_c gradually decreases.

- **Superconducting gap**

The determination of superconducting order parameters (superconducting gap size and symmetry) is critical issue in superconductors. ARPES is widely employed for the investigation of the superconducting gap size. The initial ARPES measurement on iron-based superconductors has revealed the isotropic gaps of 5.5 meV and 12.5 meV without nodes (34) and suggested s-wave rather than d-wave pairing. In addition to the ARPES measurements, a resonant spin excitation by INS has been observed in superconducting state, which indicates a sign change of the superconducting gap

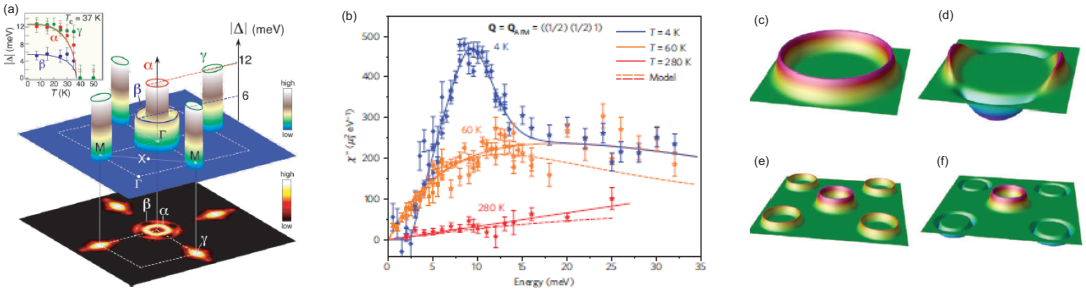

Figure 1.6: Superconducting order parameters of iron-based superconductors - (a) Superconducting gap from Ref. (34). Isotropic gaps of 5.5 meV and 12.5 meV without nodes have been observed. (b) Resonant spin excitation which indicates the sign change of the superconducting gap function from Ref. (36). (c)-(f) Several superconducting gap symmetries from Ref. (37). (c) s-wave (d) d-wave (e) s_{++}-wave (f) $s_{\pm}$-wave symmetries.

function (35) (sign change between electron and hole pockets for iron-based superconductors). Taken together, these experimental facts have led to propose an isotropic $s_{\pm}$-wave gap for iron-based superconductors (see Fig. 1.6(f)).

1.1.3 Motivation

When superconductivity in iron-based compounds was discovered, the first step was to check whether it is phonon-mediated or not. Early work in this discussion has been done by Boeri et al. in Ref. (38). In this paper, the authors have calculated the electron-phonon coupling strength λ in $LaFeAsO_{1-x}F_x$ and obtained $\lambda = 0.21$. Fig. 1.2 shows the calculated electron-phonon coupling strength in $LaFeAsO_{1-x}F_x$. The radius of the red circle denotes the electron-phonon coupling strength of the phonon mode. They have found that the obtained λ gives a maximum T_c of 0.8 K, which is much lower than the experimental $T_c = 26$ K. Hence, they have claimed the electron-phonon coupling is not enough to generate such high T_c in the compound.

Experimentally, Liu et al. in Ref. (39) has investigated the isotope effect, which gives insights into the role of phonons in superconductivity, in both $SmFeAsO_{1-x}F_x$ and $Ba_{1-x}K_xFe_2As_2$ compounds. Interestingly, they have found a large isotope effect on the iron atom (and on the other hand a weak isotope effect on the oxygen atom). Fig. 1.3 shows the observed isotope effects on both parent and superconducting samples of $SmFeAsO_{1-x}F_x$ and $Ba_{1-x}K_xFe_2As_2$. By substituting ^{56}Fe to ^{54}Fe, the isotope values are $\alpha_{SDW}, \alpha_c \sim 0.36$. Compared with full isotope value within the BCS framework of

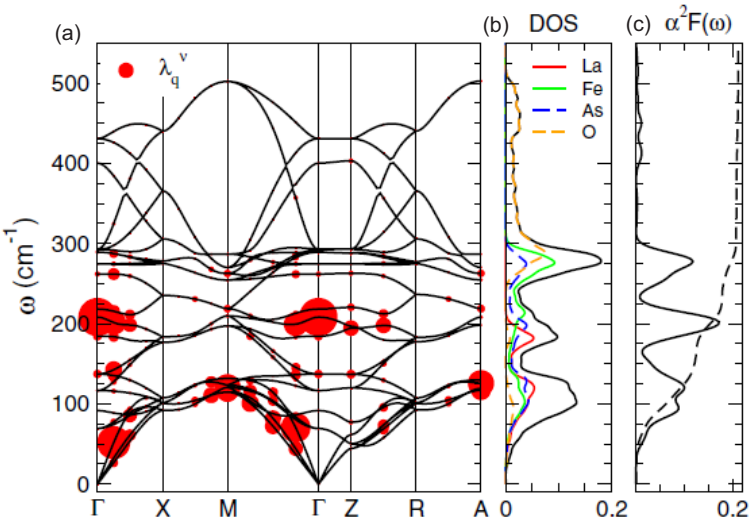

Figure 1.7: Electron-phonon coupling strength in $LaFeAsO_{1-x}F_x$ - Calculation of electron-phonon coupling strength in $LaFeAsO_{1-x}F_x$ from Ref. (38). (a) Phonon dispersion with electron-phonon coupling constant λ. The red circle and its radius denote calculated λ and its strength, respectively. (b) Atom-projected phonon density-of-state (DOS). (c) Eliashberg function $\alpha^2F(\omega)$ (solid line) and frequency-dependent $\lambda(\omega)$ (dashed line).

0.5, the obtained value of 0.36 is rather large. Hence, the authors have claimed that phonons play a key role in both magnetic and superconducting states.

These divergent results motivate the present work, where the role of phonons in the the iron-based superconductors is investigated.

1.2 Organization of this Thesis

The large majority of the experimental work on iron-based superconductors has been performed on the 122 compounds. To which extent the properties of this family are shared with other families of iron-based compounds remains unclear. In this thesis, I will focus specifically on the 111 and 11 families of compounds, which I have studied by means of Raman spectroscopy. The primary goals of the present thesis are: (i) investigating the lattice dynamics in these compounds, and (ii) understanding different physical properties via their lattice dynamics.

In chapter 2, I will describe the microscopic theory and experimental techniques for Raman scattering. First, I will introduce classical and quantum mechanical approaches

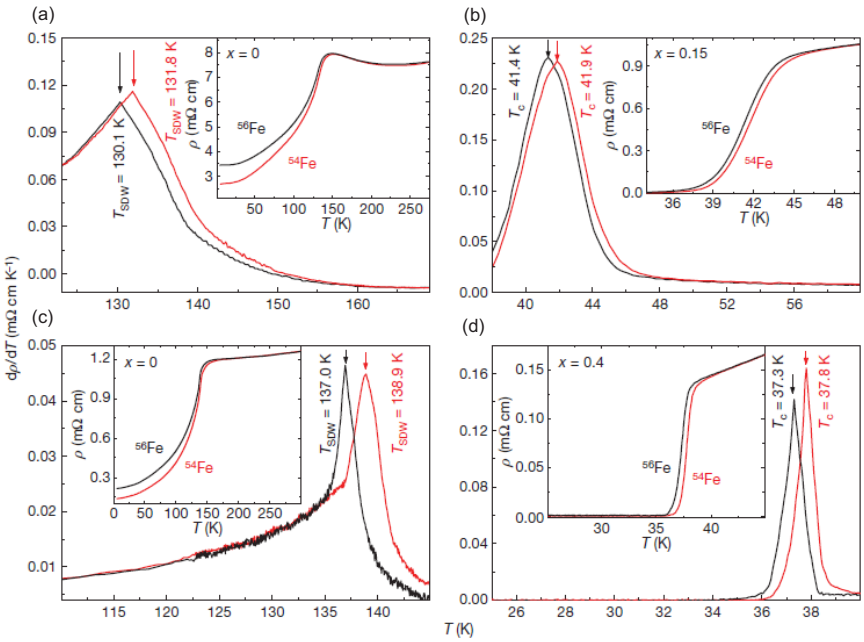

Figure 1.8: Isotope effect on $SmFeAsO_{1-x}F_x$ and $Ba_{1-x}K_xFe_2As_2$ - Resistivity ρ and $d\rho/dT$ for isotopically substituted $SmFeAsO_{1-x}F_x$ and $Ba_{1-x}K_xFe_2As_2$ from Ref. (39). (a) For parent SmFeAsO. (b) For superconducting $SmFeAsO_{0.85}F_{0.15}$. (c) For parent $BaFe_2As_2$. (d) For superconducting $Ba_{0.6}K_{0.4}Fe_2As_2$.

for Raman scattering. In particular, I will describe how phonons can be proved by Raman scattering, and derive the corresponding Raman scattering cross-section. Second, I will point out selection rules that indicate the symmetry of specific phonons. Third, I will discuss interactions of phonons in a material, especially anharmonic effects. Finally, I will describe the experimental setup and techniques (including data analysis) that are used in this thesis.

Chapter 3 will be focussed on the $Fe_{1+y}Te_{1-x}Se_x$ compound. First, I will introduce general properties and issues investigated by several techniques in this compound. In particular, I will outline the results of prior Raman scattering studies, and point out some of their limitations. Then, I will present our systematic experimental study and observations. Here, I have found unconventional linewidth broadening of the Fe B_{1g} mode with decreasing temperature, which indicated an unusual coupling between the mode and iron excess-induced magnetic fluctuations in this compound.

Chapter 4 will be focussed on LiFeAs. In this compound, there have been contro-

versial arguments about the strength of the electron-phonon coupling, but no Raman study has been reported. Here, I present the first Raman study and conclude that the electron-phonon coupling is weak, which is consistent with the unconventional superconductivity in this compound.

Finally, in chapter 5, I will discuss $NaFe_{1-x}Co_xAs$, which is isostructural and isoelectronic with LiFeAs, but has different properties from LiFeAs. Similarly to LiFeAs, the strength of electron-phonon coupling is controversial. Here, I report the first Raman study, and have found interesting features: (i) unconventional linewidth broadening with decreasing temperature, (ii) superconductivity-induced phonon renormalization. These observations suggest (i) a spin fluctuation-phonon coupling, and (ii) an important role of intra- and inter-band scattering in the compound.

2

Raman Scattering

2.1 Introduction

Photons interact with matter in two ways: absorption and scattering. Most of the scattered photons are elastically scattered (Rayleigh scattering), *i.e.* without change in energy (frequency). However, a small fraction of the photons ($\sim 10^6$ times weaker than the intensity of elastic scattering) can be inelastically scattered *i.e.* with some energy shift. The energy difference is used to create or annihilate an excitation in the studied material, which can be of various origins: a phonon, a magnetic excitation, an electron-hole pair.... The present work mainly discusses Raman scattering by the lattice vibrations in a crystal.

In this chapter, I will introduce the theoretical description of Raman scattering and the experimental techniques which are used for the present work. In Sec. 2.2, I will describe Raman scattering in classical electromagnetics and quantum mechanics. In particular, I will introduce the differential scattering cross-section in Sec. 2.2.1.2 and Sec. 2.2.2.1. In Sec. 2.3, I will introduce the Raman selection rules, then in Sec. 2.4, I will describe interactions of phonon with the environment. In Sec. 2.6, I will describe the experimental setup and the data analysis, that are used in present work.

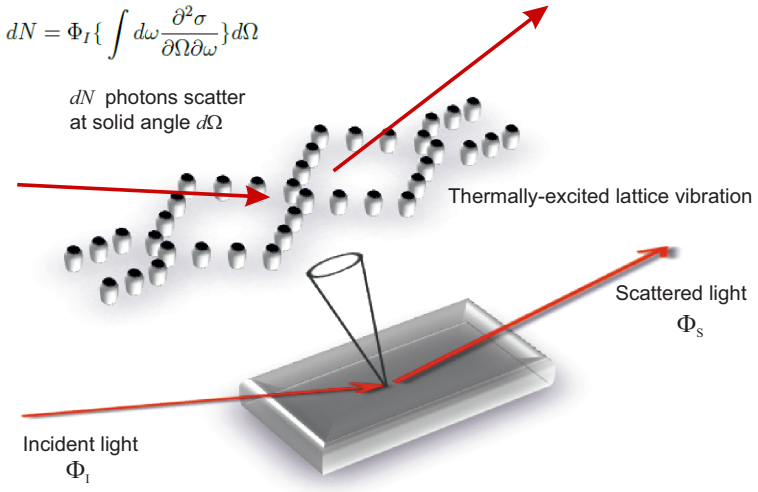

Figure 2.1: Schematic light scattering process - A small fraction of the incident photon scatters inelastically by phonons.

2.2 Basic Principles of Raman Scattering

2.2.1 Classical Approach

When light irradiates a material, a dipole moment is induced, and the induced-dipole re-emits the light (scattered light). Classically, the induced-dielectric polarization density per unit volume of the material $\mathbf{P}$ is proportional to the incident electric field $\mathbf{E}_i = E_i\hat{\mathbf{e}}_i$ ($\hat{\mathbf{e}}_i$ is the unit vector of the polarization of the incident light), and can be written as

$$\mathbf{P}_{ind} = \varepsilon_0 \chi \mathbf{E}_i \tag{2.1}$$

where ε_0 is the electric permittivity of free space, and χ is the electric susceptibility of the material (which is a tensor).

The incident electric field at given time t can be expressed by

$$\mathbf{E}_i = \mathbf{E}_0 \cos(\mathbf{k}_i \cdot \mathbf{r} - \omega_i t) \tag{2.2}$$

where $\mathbf{k}_i$ and ω_i are the propagating vector and frequency of the incident light, respectively.

At a non-zero temperature, the electric susceptibility χ can be expanded by a Taylor series expansion in terms of atomic displacements from their equilibrium position $\mathbf{u}$, and it is written as

$$\chi = \chi_0 + \sum_l \left(\frac{\partial \chi}{\partial \mathbf{u}_l}\right)_{u=0} \mathbf{u}_l + \frac{1}{2!} \sum_{l,m} \left(\frac{\partial^2 \chi}{\partial \mathbf{u}_l \mathbf{u}_m}\right)_{u=0} \mathbf{u}_l \mathbf{u}_m + \cdots \tag{2.3}$$

where

$$\mathbf{u} = \sum_l \mathbf{u}_{l0} \cos(\mathbf{q}_l \cdot \mathbf{r} - \Delta\omega_l t) \tag{2.4}$$

where l and m are different lattice sites.

Combining 2.1 with 2.2 and 2.3, we obtain

$$\begin{aligned}
\mathbf{P}_{ind} &= \varepsilon_0 \chi \mathbf{E}_i \\
&= \varepsilon_0 \chi_0 \mathbf{E}_0 \cos(\mathbf{k}_i \cdot \mathbf{r} - \omega_i t) \\
&\quad + \varepsilon_0 \sum_l \left(\frac{\partial \chi}{\partial \mathbf{u}_l}\right)_{u=0} \mathbf{u}_l \mathbf{E}_0 \cos(\mathbf{k}_i \cdot \mathbf{r} - \omega_i t) \\
&\quad + \frac{\varepsilon_0}{2} \sum_{l,m} \left(\frac{\partial^2 \chi}{\partial \mathbf{u}_l \mathbf{u}_m}\right)_{u=0} \mathbf{u}_l \mathbf{u}_m \mathbf{E}_0 \cos(\mathbf{k}_i \cdot \mathbf{r} - \omega_i t) \\
&\quad + \cdots \\
&= \mathbf{P}^0_{ind} + \mathbf{P}^1_{ind} + \mathbf{P}^2_{ind} + \cdots
\end{aligned} \tag{2.5}$$

The first term $\mathbf{P}^0_{ind}$ describes the induced-dipole moment oscillating at the same frequency as the incident light without any contribution of the lattice fluctuations. From the second term, the contribution of the lattice fluctuation is taken into account in the induced-dipole moment (first-order induced-dipole moment, second-order induced-dipole moment, $\cdots$).

2.2.1.1 First-order induced-dipole moment

From Eq. 2.5, the contribution of single atomic displacements to the polarizability of the material is described as

$$\mathbf{P}^1_{ind} = \varepsilon_0 \sum_l \left(\frac{\partial \chi}{\partial \mathbf{u}_l}\right)_{u=0} \mathbf{u}_{l0} \mathbf{E}_0 \cos(\mathbf{k}_i \cdot \mathbf{r} - \omega_i t) \cos(\mathbf{q}_l \cdot \mathbf{r} - \Delta\omega_l t) \tag{2.6}$$

By substituting 2.4 into 2.5, we obtain

$$\mathbf{P}^1_{ind} = \frac{1}{2}\varepsilon_0 \sum_l \left(\frac{\partial \chi}{\partial \mathbf{u}_l}\right)_{u=0} \mathbf{u}_{l0}\mathbf{E}_0 \Big[\cos\Big((\mathbf{k}_i + \mathbf{q}_l)\cdot\mathbf{r} - (\omega_i + \Delta\omega_l)t\Big) + \cos\Big((\mathbf{k}_i - \mathbf{q}_l)\cdot\mathbf{r} - (\omega_i - \Delta\omega_l)t\Big)\Big] \tag{2.7}$$

where $\mathbf{q}$ and $\Delta\omega$ denote the transferred momentum and energy between light and matter, respectively. Note that the induced-dipole re-emits the light (scattered light) with a propagating vector $\mathbf{k}_s = \mathbf{k}_i \pm \mathbf{q}$ and a frequency $\omega_s = \omega_i \pm \Delta\omega$. In this case, the first and second terms represent the energy gain process (anti-Stokes scattering) and the energy loss process (Stokes scattering), respectively. Typically, Raman scattering experiment is carried out with visible light of wavelength $\lambda = 300 \sim 600\ nm$. The corresponding momentum of the photon is 10^3 times smaller than the typical size of the Brillouin zone, and consequently, only phonons near the zone center (*i.e.* $\mathbf{q} = 0$) can be studied.

The material dependent information is included in the Raman tensor $R = \left(\frac{\partial \chi}{\partial \mathbf{u}}\right)_{u=0}$.

2.2.1.2 Classical scattering cross-section

In light scattering, the number of the scattered particles per unit time N_s in a given solid angle $d\Omega$ is defined as

$$dN_s = \Phi_i \frac{d\sigma}{d\Omega} d\Omega \tag{2.8}$$

where $\frac{d\sigma}{d\Omega}$ is the differential cross-section, Ω is the solid angle, and Φ_i denotes the energy flux of the incident light.

Classically, the energy flux of the light through a closed surface S is defined as

$$\Phi(r) = \oint_S \mathbf{S}\cdot d\mathbf{a} = \frac{1}{\mu_0}\oint_S (\mathbf{E}\times\mathbf{B})\cdot d\mathbf{a} \tag{2.9}$$

where $\mathbf{S}$ is the Poynting vector, and $d\mathbf{a}$ is a vector representing an infinitesimal element of area. The energy flux of the light emitted by the dipole moment is written as

$$d\Phi = \frac{\omega^4}{16\pi^2\varepsilon_0 c^3 r^2}|\mathbf{P}|^2 \sin^2\theta \hat{\mathbf{r}}\cdot d\mathbf{a} \tag{2.10}$$

where

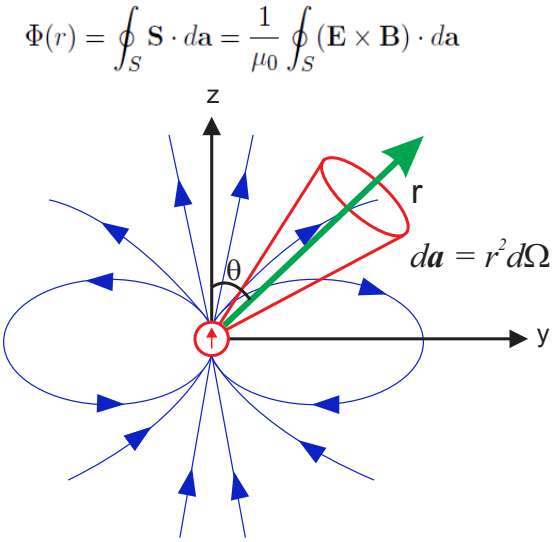

Figure 2.2: Schematic electric dipole radiation - The induced-electric dipole rera-diates light. The red arrow is the induced-electric dipole and the blue arrows denote the electric field. The energy flux of the re-emitted light propagating to r direction (the green arrow) in polar coordinates r, θ and ϕ can be defined.

$$\mathbf{E} = \frac{-\omega^2}{4\pi\varepsilon_0 c^2 r} |\mathbf{P}| \sin\theta \hat{\theta} \tag{2.11}$$

and

$$\mathbf{B} = \frac{-\mu_0 \omega^2}{4\pi c r} |\mathbf{P}| \sin\theta \hat{\phi} \tag{2.12}$$

where $\hat{\theta}$ and $\hat{\phi}$ are unit vectors in the polar coordinate system.

In a classical approach, the scattered light can be considered as the re-emitted light by the induced-electric dipole moment as shown in Fig. 2.2. As a consequence, the energy flux of the scattered light, where the scattered light propagates, can be written as

$$d\Phi_s = \frac{\omega_s^4}{16\pi^2 \varepsilon_0 c^3 r^2} \left| \hat{\mathbf{e}}_s \cdot \mathbf{P}_{ind} \right|^2 \hat{\mathbf{r}} \cdot d\mathbf{a} \tag{2.13}$$

where $\hat{\mathbf{e}}_s$ is unit vector of the polarization of the scattered light, ω_s is frequency of the scattered light, and as $\frac{d\mathbf{a}}{r^2} = d\Omega$, we obtain

$$d\Phi_s = \frac{\omega_s^4}{16\pi^2 \varepsilon_0 c^3} \left| \hat{\mathbf{e}}_s \cdot \mathbf{P}_{ind} \right|^2 d\Omega \tag{2.14}$$

Replacing 2.1 into 2.14, we obtain

$$d\Phi_s = \Phi_i \frac{\omega_s^4}{16\pi^2 c^4} \left| \hat{\mathbf{e}}_s \cdot \chi \cdot \hat{\mathbf{e}}_i \right|^2 d\Omega \tag{2.15}$$

where $\Phi_i = \varepsilon_0 c E_i^2$ (40).

Thus, by definition, we can obtain the differential scattering cross-section as

$$\frac{d\sigma}{d\Omega} = \frac{\omega_s^4}{16\pi^2 c^4} \left| \hat{\mathbf{e}}_s \cdot \chi \cdot \hat{\mathbf{e}}_i \right|^2 \tag{2.16}$$

In the case of the first order induced-dipole moment, as $\chi = R\mathbf{u}$ for a single mode, the differential scattering cross-section is written by (40)

$$\frac{d\sigma}{d\Omega} = \frac{\omega_s^4}{16\pi^2 c^4} \left| \hat{\mathbf{e}}_s \cdot R \cdot \hat{\mathbf{e}}_i \right|^2 \langle \mathbf{u}^2 \rangle \tag{2.17}$$

where $\langle\ \rangle$ represents the thermodynamical average over the ground state of the system. In particular, in spectroscopy, for a single mode with a frequency $\Delta\omega$, the differential scattering cross-section can be written as (40)

$$\frac{\partial^2 \sigma}{\partial\Omega \partial\omega} = \frac{\omega_s^4}{16\pi^2 c^4} \left| \hat{\mathbf{e}}_s \cdot R \cdot \hat{\mathbf{e}}_i \right|^2 \langle \mathbf{u}^2 \rangle \delta(\omega - \Delta\omega) \tag{2.18}$$

where δ is the delta function, as the system fluctuates with a single frequency (normal mode). Furthermore, the differential scattering cross-section implies the Raman intensity would be

$$I_s \propto \left| \hat{\mathbf{e}}_s \cdot R \cdot \hat{\mathbf{e}}_i \right|^2 \tag{2.19}$$

As we shall discuss later, the Raman intensity depends on the relative orientation of incident and scattered light polarization. This dependence is called Raman selection rules.

2.2.1.3 Classical intensity ratio

The scattered Raman intensity is directly proportional to the differential scattering cross-section, and therefore we estimate the ratio between Stokes and anti-Stokes scattering intensities to be

$$\frac{I_{Stokes}}{I_{anti-Stokes}} = \frac{(\omega_i - \Delta\omega)^4}{(\omega_i + \Delta\omega)^4} \tag{2.20}$$

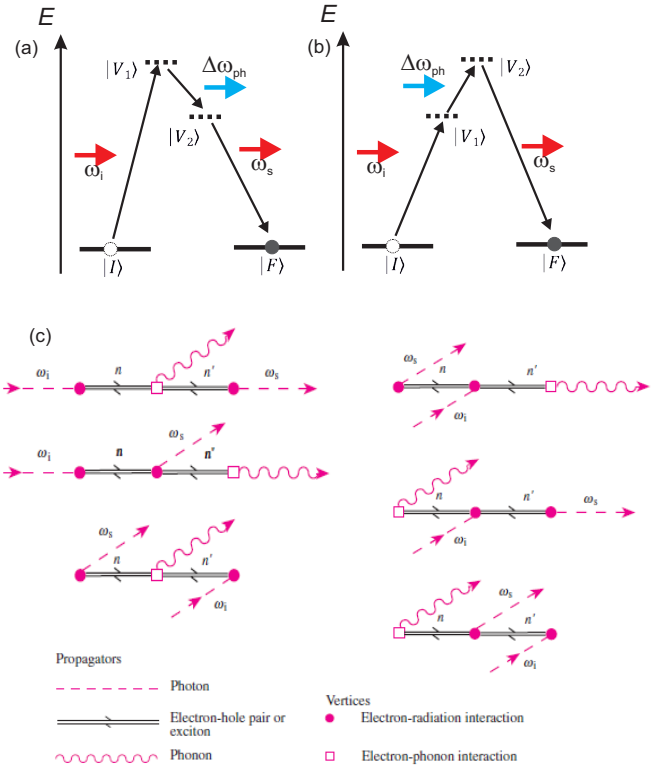

Figure 2.3: Schematic Raman scattering process - (a) Stokes scattering. (b) anti-Stokes scattering. (c) Feynman diagrams for Stokes scattering from Ref. (41).

which is temperature independent. However, the experimentally measured intensity ratio depends on temperature. As a consequence, a quantum mechanical description is required.

2.2.2 Quantum Mechanical Approach

The light scattering process can be considered as the interaction of a photon of momentum $\mathbf{k}$ (energy $\hbar\omega = \hbar ck$) and polarization $\mathbf{e}$ with N electrons in the solid. The photon can be absorbed in the system and re-emitted with momentum $\mathbf{k}'$ (different energy) and polarization $\mathbf{e}'$.

Quantum mechanically, the Hamiltonian of the system can be written as

$$H = H_p + H_e + H_{ph} + H_{e-p} + H_{e-ph} \tag{2.21}$$

where H_e, H_{ph}, and H_p are the Hamiltonian of electron, phonon, and photon,

respectively. H_{e-p} and H_{e-ph} represent interactions between electron and photon, and electron and phonon, respectively. Note that the direct coupling between the photons and the lattice vibrations is negligible, hence we do not include any photon-phonon coupling term in 2.21. As shown in Fig. 2.3, Stokes (anti-Stokes) Raman scattering event involving phonon can be described in a three-step process.

(i) The system in an initial state of the system $|I\rangle = |p_0\rangle|e_0\rangle|ph_0\rangle$ (where $|p\rangle, |e\rangle$ and $|ph\rangle$ denote photon, electron and phonon states, respectively), can be excited into either a virtual or a real excited state (see Sec. 2.2.2.3) $|V_1\rangle = |p_1\rangle|e_1\rangle|ph_0\rangle$ by electron-photon coupling.

(ii) The system in $|V_1\rangle$ can decay into another intermediate excited state $|V_2\rangle = |p_1\rangle|e_2\rangle|ph_2\rangle$ by electron-phonon coupling.

(iii) The system in $|V_2\rangle$ decays into the final ground state $|F\rangle = |p_0\rangle|e_0\rangle|ph_2\rangle$ by electron-photon coupling.

To calculate the corresponding cross-section, it is useful to use Feynman diagrams (see Fig. 2.3(c)) (41). Note that as phononic processes are time reversal symmetric, the time order of the three interaction steps is arbitrary, and $3! = 6$ possible permutations are therefore possible.

In order to describe the differential scattering cross-section of Raman scattering, we should consider transition probability between initial and final states. Using Fermi's Golden rule, the transition probability can be obtained for each process.

(I) For the first vertex of Stokes scattering (photon-electron coupling),

$$P_{I\to V_1} \sim \left| \frac{\langle V_1|H_{e-p}|I\rangle}{[\hbar\omega_i - (E_{V_1} - E_I)]} \right|^2 \tag{2.22}$$

where E_{V_1} and E_I denote the energy of states $|V_1\rangle$ and $|I\rangle$.

(II) For the second vertex (electron-phonon coupling),

$$P_{V_1\to V_2} \sim \left| \frac{\langle V_2|H_{e-ph}|V_1\rangle}{[\hbar\omega_i - \hbar\Delta\omega_{ph} - (E_{V_2} - E_I)]} \right|^2 \tag{2.23}$$

where E_{V_2} denotes the energy of states $|V_2\rangle$, and $-\hbar\Delta\omega_{ph}$ implies the emission of phonon.

(III) For the third vertex (electron-photon coupling),

$$P_{V_2\to F} \sim \left| \frac{\langle F|H_{e-p}|V_2\rangle}{[\hbar\omega_i - \hbar\Delta\omega_{ph} - \hbar\omega_s - (E_F - E_I)]} \right|^2 \tag{2.24}$$

where E_F denotes the energy of state $|F\rangle$.

Furthermore, as shown by Fig. 2.3(a)(b), the final state is the same as the initial state, and the energy conservation therefore requires $\delta(\hbar\omega_i - \hbar\Delta\omega_{ph} - \hbar\omega_s)$.

Thus, we obtain the transition rate of Stokes Raman process, and it can be written as (41)

$$P_{I\to F} = \frac{2\pi}{\hbar} \left| \frac{\langle F|H_{e-p}|V_2\rangle\langle V_2|H_{e-ph}|V_1\rangle\langle V_1|H_{e-p}|I\rangle}{[\hbar\omega_i - (E_{V_1} - E_I)][\hbar\omega_i - \hbar\Delta\omega_{ph} - (E_{V_2} - E_I)]} + 5 \text{ permuts} \right|^2 \delta(\hbar\omega_i - \hbar\Delta\omega_{ph} - \hbar\omega_s) \tag{2.25}$$

Similar to the Stokes process, the transition rate of anti-Stokes process can be written as

$$P_{I\to F} = \frac{2\pi}{\hbar} \left| \frac{\langle F|H_{e-p}|V_2\rangle\langle V_2|H_{e-ph}|V_1\rangle\langle V_1|H_{e-p}|I\rangle}{[\hbar\omega_i - (E_{V_1} - E_I)][\hbar\omega_i + \hbar\Delta\omega_{ph} - (E_{V_2} - E_I)]} + 5 \text{ permuts} \right|^2 \delta(\hbar\omega_i + \hbar\Delta\omega_{ph} - \hbar\omega_s) \tag{2.26}$$

where $+\hbar\Delta\omega_{ph}$ implies the absorption of a phonon.

2.2.2.1 First-order Raman scattering

In order to gain further insights into Stokes and anti-Stokes scattering, one can write the Hamiltonian of the electron-phonon coupling as (42)

$$H_{e-ph} = \sum_{k,q,\nu,\sigma} g^{\nu}_{k,q} c^{\dagger}_{k+q,\sigma} c_{k,\sigma} (b_{q,\nu} + b^{\dagger}_{-q,\nu}) \tag{2.27}$$

where k, q, ν, and σ represent the momentum of the electron, the momentum of the phonon, the phonon branch, and the spin of the electron, respectively. $g^{\nu}_{k,q}$ is the

matrix element determined by the interaction Hamiltonian, $c^{\dagger}_{k+q,\sigma}(b^{\dagger}_{-q,\nu})$ and $c_{k,\sigma}(b_{q,\nu})$ are the creation and annihilation operators of the electron (phonon). Note that in the second quantized-notation, the annihilation a and creation $a^{\dagger}$ operators satisfy following conditions:

$$\begin{aligned} a^{\dagger}|n\rangle &= \sqrt{n+1}|n+1\rangle \\ a|n\rangle &= \sqrt{n}|n-1\rangle \\ a^{\dagger}a|n\rangle &= n|n\rangle \end{aligned} \tag{2.28}$$

where $|n\rangle$ and n denote the n^{th} excited state and the number of particles in the state.

Using 2.27 and 2.28, for the single phonon case, the electron-phonon coupling term in 2.25 and 2.26 can be written as

$$\begin{aligned} \langle V_2|H_{e-pn}|V_1\rangle_{Stokes} &= \langle V_2|\sum_{k,\sigma} g^{\nu}_{k,q} c^{\dagger}_{k+q,\sigma} c_{k,\sigma} b^{\dagger}_{-q,\nu}|V_1\rangle \\ &= \sqrt{n+1}\langle ph_2|\langle e_2|\langle p_1|\sum_{k,\sigma} g^{\nu}_{k,q} c^{\dagger}_{k+q,\sigma} c_{k,\sigma}|p_1\rangle|e_1\rangle|ph_2\rangle \end{aligned} \tag{2.29}$$

$$\begin{aligned} \langle V_2|H_{e-pn}|V_1\rangle_{anti-Stokes} &= \langle V_2|\sum_{k,\sigma} g^{\nu}_{k,q} c^{\dagger}_{k+q,\sigma} c_{k,\sigma} b_{q,\nu}|V_1\rangle \\ &= \sqrt{n}\langle ph_2|\langle e_2|\langle p_1|\sum_{k,\sigma} g^{\nu}_{k,q} c^{\dagger}_{k+q,\sigma} c_{k,\sigma}|p_1\rangle|e_1\rangle|ph_2\rangle \end{aligned} \tag{2.30}$$

where n is the thermal population of phonon following Bose-Einstein distribution $\frac{1}{e^{\frac{\hbar\Delta\omega_{pn}}{k_B T}}-1}$. Note that Stokes and anti-Stokes processes have different thermal factor in the transition probability.

2.2.2.2 Quantum mechanical intensity ratio

From 2.29 and 2.30, we estimate the ratio of intensities between Stokes and anti-Stokes scattering

$$\frac{I_{Stokes}}{I_{anti-Stokes}} \propto \frac{n+1}{n} = e^{\frac{\hbar\Delta\omega_{pn}}{k_B T}} \tag{2.31}$$

The intensity ratio between Stokes and anti-Stokes scattering depends on the temperature of the scattering medium, in contrast to the classical approach. As a consequence, one can determine the temperature of the medium by measuring the ratio between Stokes and anti-Stokes intensity.

2.2.2.3 Resonant Raman scattering

The quantum mechanical approach also allows one to understand resonant Raman scattering, which can not be captured in the classical approach. When the incoming photon energy is not enough to excite electrons in a material into a real electronic state of the system, the electrons can be excited into a virtual intermediate state, and this is called non-resonant Raman scattering. However, when either the incoming or the scattered photon energy matches an energy gap between the occupied ground state and unoccupied excited state (in case of a semiconductor, the energy gap between valence and conduction bands), the electrons can be excited into a real electronic state, and this is called resonant Raman scattering. In this case, the Raman intensity can be tremendously enhanced compared with that of non-resonant Raman scattering.

2.3 Selection Rules

As shown in 2.19, the Raman intensity depends on the polarization of incident and scattered light fields and the Raman tensor. The symmetry of the phonon involved in the Raman scattering process can be well characterized by the irreducible representations of the point group symmetry of the material, as the phonon is directly related to the atomic positions of the materials. As a consequence, the number of phonons involved in the materials corresponds to the number of atoms in the unit cell of the materials, and it is given by

$$N_{ph} = Dimension \times N_a \tag{2.32}$$

where N_{ph} and N_a are total number of phonons and number of atoms in the unit cell. The total number of phonons is also divided into the number of acoustic phonons (number of degree of freedom (dimension) D) and optical phonons ($N_{ph} - D$).

Symbol	Property
A	singly degenerate state
	symmetric upon rotation about the principal rotational axis
B	singly degenerate state
	anti-symmetric upon rotation about the principal rotational axis
E	doubly degenerate states
T (or F)	triply degenerate states
1	symmetric upon rotation about the center of the atom
2	anti-symmetric upon rotation about the center of the atom
g	symmetric under inversion through the center of the atom
u	anti-symmetric under inversion through the center of the atom

Table 2.1: Irreducible representations of groups (Mulliken Symbols)

2.3.1 Porto Notation

In Raman scattering, the Porto notation, which describes both the direction and polarization of the incident and scattered light with respect to the orientation of the crystal, is generally used. The Porto notation is defined as

$$k_i(e_i e_s)k_s \tag{2.33}$$

where $k_i(k_s)$ and $e_i(e_s)$ denote a direction of the propagation and polarization of the incident (scattered) light, respectively.

For example, one can use (i) either $z(xy)\bar{z}$ or $c(ab)\bar{c}$ notation, if the incident light propagates along the c-axis of the sample with polarization along the a-axis of the sample, and the scattered light propagates in the opposite direction to the incident light with polarization along the b-axis, (ii) either $z(x'y')\bar{z}$ or $c(a'b')\bar{c}$ notation, if the incident light propagates along the c-axis of the sample with rotated polarization by 45° from the a-axis, and the scattered light propagates in the opposite direction to the incident light with rotated polarization by 45° from the b-axis.

2.3.2 Symmetry of Raman Tensor

In general, a center of inversion is present in a vibrational spectroscopy. In Raman spectroscopy, the even mode of the Raman tensor $R_{ij} = R_{ji}$ is Raman active, while

the odd mode $R_{ij} = -R_{ji}$ is Raman inactive. In infrared (IR) spectroscopy, it is vice versa. In Table. 2.1, Mulliken Symbols, which describe the irreducible representations of symmetry groups (43), are summarized. In particular, the irreducible representations of the Raman tensor in D_{4h} point group, where most of iron-based superconductors belong to, are shown in Table. 2.2 (1). Further information for various point groups is well summarized in Ref. (44).

2.4 Interactions of Phonons

In Raman spectroscopy, phonon features are characterized by their integrated intensity, frequency (which corresponds to the phonon energy), linewidth (which inversely corresponds to the phonon lifetime), and lineshape. As mentioned in 2.18, the lineshape of a non-interacting phonon is a delta-function. However in a real matieral, the phonon interacts with the environment. In most cases, the phonon interacts with other phonons and electrons (in some cases, magnon or other electronic excitations). Defects are also another source of phonon broadening. As a consequence, the spectrum of phonon broadens, and the delta-function must be replaced by an appropriate lineshape function. Eq. 2.18 can then be modified as

$$\frac{\partial^2\sigma}{\partial\Omega\partial\omega} = \frac{\omega_s^4 V^2}{16\pi^2 c^4}|\hat{\mathbf{e}}_s \cdot R \cdot \hat{\mathbf{e}}_i|^2 \langle \mathbf{u}^2 \rangle L(\omega - \Delta\omega) \tag{2.34}$$

where $L(\omega - \Delta\omega)$ is the lineshape function.

Tetragonal (D_{4h})			
$\begin{pmatrix} \alpha_{xx} & 0 & 0 \\ 0 & \alpha_{yy} & 0 \\ 0 & 0 & \alpha_{zz} \end{pmatrix}$	$\begin{pmatrix} 0 & \alpha_{xy} & 0 \\ -\alpha_{yx} & 0 & 0 \\ 0 & 0 & 0 \end{pmatrix}$	$\begin{pmatrix} \alpha_{xx} & 0 & 0 \\ 0 & -\alpha_{xx} & 0 \\ 0 & 0 & 0 \end{pmatrix}$	$\begin{pmatrix} 0 & \alpha_{xy} & 0 \\ \alpha_{xy} & 0 & 0 \\ 0 & 0 & 0 \end{pmatrix}$
A_{1g}	A_{2g}	B_{1g}	B_{2g}
$\begin{pmatrix} 0 & 0 & \alpha_{xz} \\ 0 & 0 & 0 \\ \alpha_{zx} & 0 & 0 \end{pmatrix}$	$\begin{pmatrix} 0 & 0 & 0 \\ 0 & 0 & \alpha_{xz} \\ 0 & \alpha_{zx} & 0 \end{pmatrix}$		
E_g	E_g		

Table 2.2: Irreducible representations of the Raman tensor in the D_{4h} point group from Ref. (1).

The temperature dependence of the phonon spectrum is widely used to investigate the interactions of phonon with the environment. In particular, the broadening of phonon features by defect is generally weakly temperature dependent, in contrast to broadening by dynamical excitations.

2.4.1 Phonon-phonon interactions

The most general feature appearing in the temperature dependent phonon spectrum is due to phonon-phonon interaction, which is usually called anharmonic effect (45, 46). Within the harmonic approximation, all phonons are independent. However, in a real material, phonons interact with each other, and this leads to a temperature dependent shift in frequency and linewidth in Raman spectrum. In particular, with increasing temperature, the number of possible phonon decay channels increases. This leads to a broadening and softening of the phonon features.

First, the phonon frequency including the anharmonic effect can be written by (46)

$$\omega_{ph}(\Omega) = \omega_0 + \Sigma(\Omega) \qquad \text{with} \qquad \Sigma(\Omega) = \Delta(\Omega) + i\Gamma(\Omega) \tag{2.35}$$

where Ω is the damping parameter caused by the anharmonic effect and $\Sigma(\Omega)$ is the phonon self-energy describing the changes in the phonon frequency and linewidth caused by the anharmonic interactions. The phonon self-energy is complex. The real and imaginary parts of the self-energy correspond to the phonon energy and lifetime, and they are related by Kramers-Kronig relations.

Due to the anharmonic effect, the lineshape of the Stokes peak can be written as (46)

$$L_S \propto \frac{\frac{1}{2}\Gamma(\Omega)}{[\omega_0 + \Delta(\Omega) - \Omega]^2 + [\frac{1}{2}\Gamma(\Omega)]^2}[n(\Omega)+1] \quad \text{with} \quad n(\Omega) = \frac{1}{e^{\frac{\hbar\Omega}{k_B T}} - 1} \tag{2.36}$$

Note that the inverse phonon lifetime τ^{-1} is proportional to the half-width-at-half-maximum (HWHM) of the phonon profile.

Second, in order to understand the temperature dependence, an approach suggested by Klemens is widely accepted (45). Within the Klemens approach, the optical phonon

with ω_0 at $\mathbf{q} \approx 0$ (at $T = 0$) can decay into two acoustic phonons with identical frequencies ($\omega_0/2$) and opposite momenta. As a consequence, the optical phonon frequency and linewidth are renormalized by the following equations.

$$\omega_{ph}(T) = \omega_0 - C\left[1 + \frac{2}{e^{\frac{\hbar\omega_0}{2k_BT}} - 1}\right] \tag{2.37}$$

$$\Gamma_{ph}(T) = \Gamma_0 + \Gamma\left[1 + \frac{2}{e^{\frac{\hbar\omega_0}{2k_BT}} - 1}\right] \tag{2.38}$$

where C and Γ are positive constants. ω_0 is the bare phonon frequency, Γ is FWHM of the spectrum, and Γ_0 a residual (temperature independent) linewidth originating from sample imperfections or electron-phonon interactions.

2.4.2 Electron-phonon interaction

An additional prominent interaction is the electron-phonon interaction. Most phonons couple only weakly to the electrons at Fermi level, leading to a symmetric Lorentzian lineshape. If the phonon couples strongly to the electrons, the phonon lineshape becomes asymmetric. The resulting Fano profile (47) can be written as

$$L_F = C_F \frac{(q + \epsilon)^2}{1 + \epsilon^2} \tag{2.39}$$

where $\epsilon = (\omega - \omega_0)/\frac{1}{2}\Gamma$, $q \sim (V_E N(E))^{-1}$ is the asymmetric parameter with the strength of the electron-phonon coupling V_E and electronic density-of-state (DOS) at the Fermi level $N(E)$.

- **Phonon self-energy in the superconducting state**

In the superconducting state, a gap opens at the Fermi energy level. Because of the gap, there are no available electronic state to couple to the phonons. This leads to a renormalization of the phonon frequency and linewidth, which is presented in Fig. 2.4 based on calculation of a single band superconductor with $d_{x^2-y^2}$-wave superconducting gap symmetry (cuprate $YBa_2Cu_3O_7$) (49). Fig. 2.4 implies (i) for phonon energy $\omega_{ph} <$ superconducting gap energy $2\Delta_{SC}$, the phonon mode softens and narrows, as the phonon can not decay into electron-hole pair, (ii) for $\omega_{ph} > 2\Delta_{SC}$, the

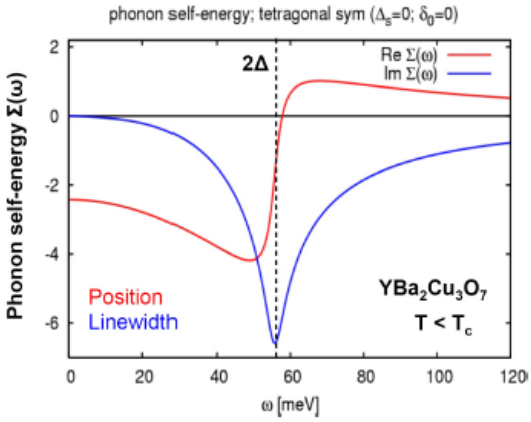

Figure 2.4: Superconductivity-induced phonon self-energy - Superconductivity-induced phonon self-energy in the $d_{x^2-y^2}$-wave superconducting state of $YBa_2Cu_3O_7$ from Ref. (48)

phonon mode hardens and broadens, as the decay probability is enhanced due to the pileup of electronic structure above the gap ("pair-breaking peak").

Furthermore, the integrated phonon intensity is also affected by the electron-phonon interaction in the superconducting state. It can be written as (50)

$$I_{ph} = \left[\sqrt{I^0_{ph}} + \frac{V_E}{\omega_{el} - \omega_{ph}}\sqrt{I_{el}}\right] \tag{2.40}$$

where V_E is electron-phonon coupling constant, I^0_{ph} and ω_{ph} are the bare phonon intensity and frequency, and I_{el} and ω_{el} are the integrated intensity and maximum frequency of the pair-breaking peak, respectively.

2.5 Electronic Raman scattering

In a material, photons can also be scattered by resonant inter-band and non-resonant intra-band electronic excitations. Such effect creates a background of the Raman spectrum, so called electronic Raman scattering. In most of high T_c superconductors, typical electronic inter-band gaps are around 1 eV, and the contribution for electronic Raman scattering therefore originates mainly from intra-band transitions near the Fermi level. In metallic materials, the intensity of electronic signal is weak as the incoming photon is screened by the electrons of the metal (48).

The differential scattering cross section for electronic Raman scattering can be written as (2)

$$\frac{\partial^2\sigma}{\partial\Omega\partial\omega} = \frac{\omega_s}{\omega_i} r_0^2 S_{\gamma\gamma}(\mathbf{q},\omega) \tag{2.41}$$

where

$$S_{\gamma\gamma}(\mathbf{q},\omega) = -\frac{\hbar}{\pi}[1+n(\omega)]\ \mathrm{Im}\chi_{\gamma\gamma}(\mathbf{q},\omega) \tag{2.42}$$

where $r_0^2 = e^2/mc^2$ is the Thompson radius, ω_i and ω_s are the frequency of the incoming and scattered photon, respectively. $\mathbf{q}$ is the momentum transfer by the photon (in Raman scattering $\mathbf{q} \to 0$), $S_{\gamma\gamma}(\mathbf{q},\omega)$ is the dynamical structure factor which is related to the imaginary part of the Raman response function $\chi_{\gamma\gamma}(\mathbf{q},\omega)$, and $n(\omega)$ is the Bose-Einstein distribution function.

Furthermore, for the non-interacting electrons the Raman response function $\chi_{\gamma\gamma}(\mathbf{q},\omega)$ can be a two-particle effective density correlation function, and be written as (51)

$$\chi_{\gamma\gamma}(\mathbf{q},\omega) = < [\rho(\mathbf{q}),\rho(-\mathbf{q})] >_\omega \tag{2.43}$$

where $<>$ denotes a thermodynamic average, and

$$\rho(\mathbf{q}) = \sum_{\mathbf{k},\sigma} \gamma(\mathbf{k},\mathbf{q}) c^\dagger_{k+q,\sigma} c_{k,\sigma} \tag{2.44}$$

where $c^\dagger_{k+q,\sigma}$ and $c_{k,\sigma}$ are the creation and annihilation operators of electrons, and σ denotes the spin state.

For the small momentum transfers (non-resonant scattering), the Raman vertex $\gamma(\mathbf{k},\mathbf{q})$ can be written in terms of the curvature of the energy band dispersion (2)

$$\gamma(\mathbf{k},\mathbf{q}\to 0) = \frac{m}{\hbar^2}\sum_{\alpha,\beta} e^s_\alpha \frac{\partial^2\varepsilon_{\mathbf{k}}}{\partial k_\alpha \partial k_\beta} e^i_\beta \tag{2.45}$$

where m is the electron mass, e^s and e^i denote the polarization of the scattered and incident photon, respectively. The Raman vertex γ under the tetragonal symmetry, where most of high T_c superconductors belong to, is listed in Table. 2.4.

Below superconducting transition, the low energy electronic background undergoes a redistribution in energy due to the superconducting gap Δ opening. In the case of BCS

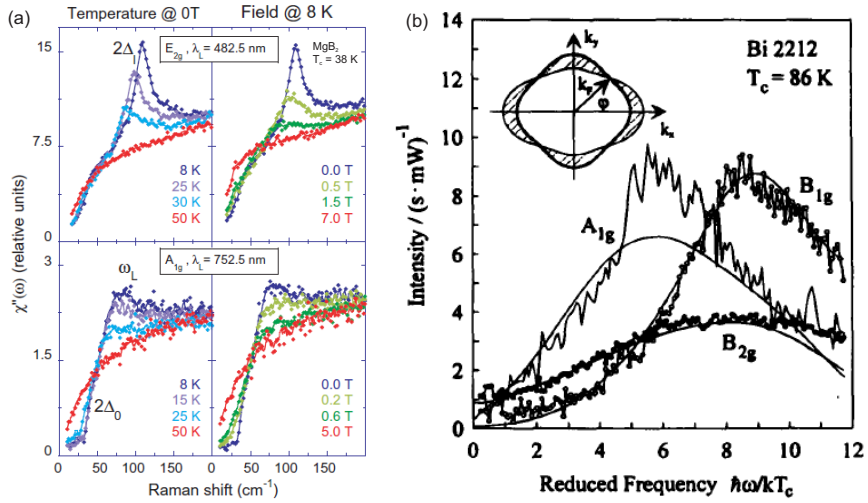

Figure 2.5: Electronic Raman scattering in superconductors - (a) Electronic Raman spectra in BCS superconductor from Ref. (52). Sharp peak appears at the twice of the superconducing gap Δ below T_c. (b) Electronic Raman spectrum in high T_c superconductor from Ref. (2). Pair-breaking 2Δ peaks appear at different frequency in different symmetries. This observation indirectly give an insight into the symmetry of the superconducting gap, and suggests $d_{x^2-y^2}$-wave gap.

superconductors, the electronic Raman intensity dramatically increases at the energy of 2Δ (52) (see Fig. 2.5(a)). This 2Δ peak is called as pair-breaking peak. However, for high T_c superconductors (especially d-wave superconductors), the pair-breaking peak is different from that in BCS superconductors. In the cuprate superconductors, the pair-breaking peak appears at different position in different symmetries, and the peak frequency in B_{1g} symmetry is maximum (2) (see Fig. 2.5(b)). This observation can not be understood within a conventional BCS gap symmetry, and supports the $d_{x^2-y^2}$-wave gap in the cuprate superconductors.

$\gamma_{A_{1g}}$	$\frac{1}{2}t[\cos k_x + \cos k_y] + 2t' \cos k_x \cos k_y$
$\gamma_{B_{1g}}$	$\frac{1}{2}t[\cos k_x - \cos k_y]$
$\gamma_{A_{2g}}$	0
$\gamma_{B_{2g}}$	$2t' \sin k_x \sin k_y$

Table 2.3: Raman vertex in the tetragonal symmetry from Ref. (2). t and t' are the nearest and next-nearest neighbor hopping parameters, respectively.

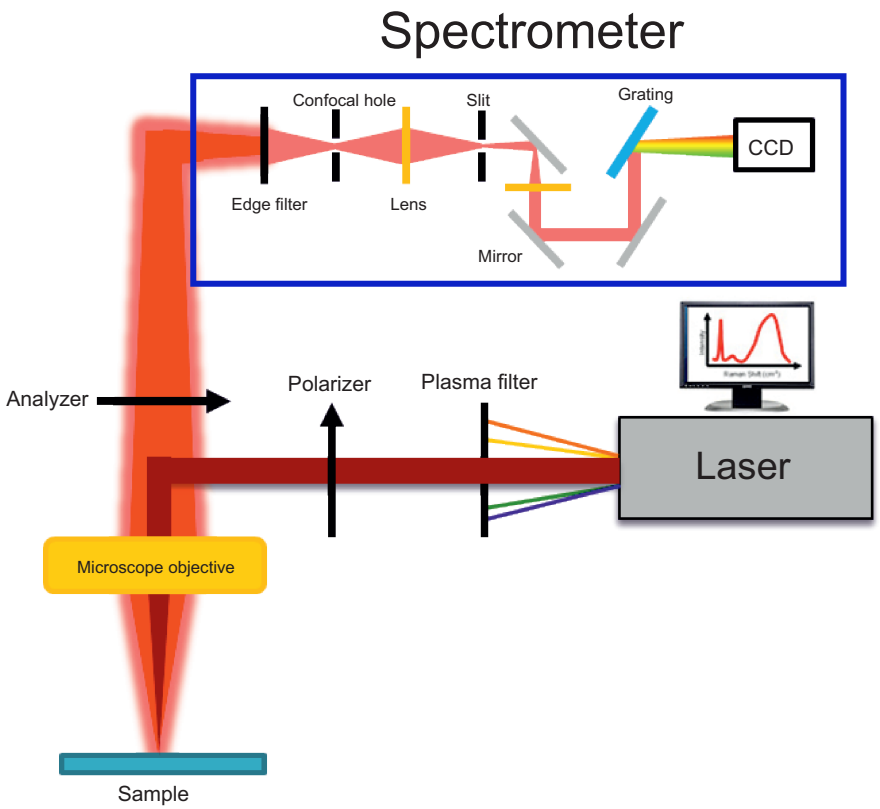

Figure 2.6: Schematic Raman scattering experiment - Schematic diagram of a high-resolution micro-Raman scattering experiment.

2.6 Experimental Techniques

2.6.1 Experimental Setup

Micro-Raman setups are widely employed, as they combine high spatial resolution, and high intensity, and require a very small sample size ($\sim$ 10 μm). Fig. 2.6 shows a schematic diagram of such a Raman scattering experiment. The micro-Raman setup can be divided into four main parts: light source, polarizers, sample and sample environment, and spectrometer.

- **Light source**

In order to measure inelastic scattering, which is $\sim 10^6$ times weaker than the intensity of elastic scattering, an intense and monochromatic light source, *i.e.* a laser, is required for Raman measurement. In addition to the laser, two filters (an interferential

filter (plasma filter) and an optical density filter) are located between the laser and a sample. First, the plasma filter is used for blocking all undesired light from the laser, such as fluorescence and laser induced-plasma emission. The undesired light acts like a secondary source and causes undesired effects, in particular, it overshadows the Raman spectrum as it is superimposed on the Raman spectrum of the sample. Second, the optical density filter is used for controlling the power of the incident light.

Usually, He^+/Ne^+ and Ar^+/Kr^+ mixed gas lasers are widely used, and they provide several wavelengths listed in Table. 2.4. In present experiment, the 632.817 nm line of the He^+/Ne^+ mixed gas laser was used.

- **Polarizers**

The Raman selection rules depend on the relative orientation of incident and scattered light polarization. As a consequence, two polarizers are used in typical Raman experiments (see Fig. 2.6). The first one is located between the laser and the sample, and allows one to select a certain polarization of the incident light. In the present experiment, in order to change the direction of the incident light polarization, a half-wave plate was employed. The second one, so-called the analyzer, is located between the sample and the spectrometer, and used for selecting a certain polarization of the scattered light.

- **Sample and Sample Environment**

The incident laser beam is focused through a microscope objective on the sample surface, and its position can be monitored by a camera. The samples are mounted on a helium-flow cryostat (CryoVac micro-Raman cryostat) allowing measurements between 5 K and room temperature. The scattered light from the sample is collected through the microscope objective which is also used for the incident light. The spectra are

Mixed-gas laser	Wavelength (nm)
He^+/Ne^+	632.8
Ar^+/Kr^+	454.5, 457.9, 465.8, 472.7, 476.5, 488.0,
	496.5, 501.7, 514.5, 520.8, 530.9, 568.2, 647.1

Table 2.4: Laser lines provided by He^+/Ne^+ and Ar^+/Kr^+ mixed gas lasers.

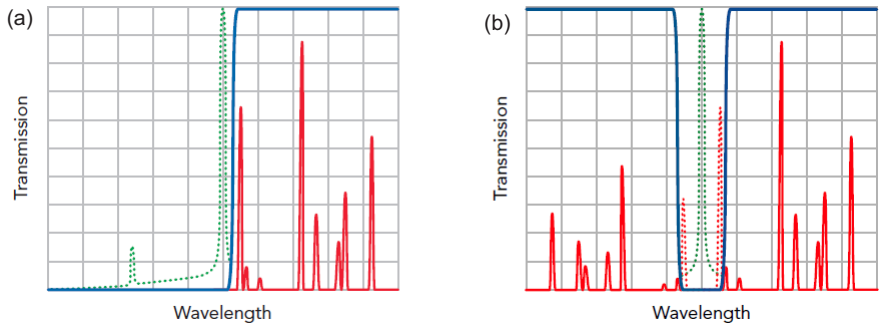

Figure 2.7: Filters used in Raman scattering experiment - (a) A razor-edge filter blocks short wavelength light below a certain wavelength and is used to measure Stokes scattering part. (b) A notch filter blocks only a certain wavelength light and is usually used to block the elastically scattered light.

taken in a backscattering geometry, and the propagating direction of the incident and the scattered light is perpendicular to the sample surface.

- **Spectrometer**

The primary purpose of the spectrometer is to resolve inelastically scattered light with high resolution. For that purpose, as shown in Fig. 2.6, the spectrometer consists of an edge filter (or a notch filter), a confocal hole, a slit, a grating, and a charge-coupled device (CCD) camera.

First, the scattered light (both elastic and inelastic light) passes through a razor-edge filter or a notch filter. The razor-edge filter blocks all light below (or above) a certain wavelength and allows one to measure only the Stokes scattering (or the anti-Stokes scattering) part. In general, a long-wavelength-pass razor-edge filter is used to measure the Stokes scattering part. The notch filter is used to block the elastically scattered light and allows one to measure both anti-Stokes and Stokes scattering parts (see Fig. 2.7). In our experimental setup, two razor-edge filters were used. As a consequence, the spectrum below $\sim$ 50 cm^{-1} was suppressed and thea spectrum for $\sim$ 50 - 100 cm^{-1} was partly overshadowed.

Second, in order to get high spatial resolution of the scattered light, a confocal hole and a slit were used. As the incident light penetrates into the sample, it scatters from different positions (layers) of the sample. When the scattered light from the different positions is collected by the microscope objective, it is refocused on a different position.

As a consequence, the confocal hole is located where the scattered light from a certain position is focused, and blocks other defocused light. Hence, the spatial resolution of the scattered light can be enhanced. In addition to the confocal hole, additional slit is used. By adjusting the size of the slit, one can compromise between the resolution and the intensity.

Finally, the scattered light reaches a single holographic grating (1800 or 600 lines/mm), and the dispersed scattered light is detected by a CCD camera which consists of two-dimensional arrays of millions of individual detectors, so called pixels. In Raman spectroscopy, the CCD camera is widely used, as it converts the photon signal into an electrical signal and allows multichannel detection, which means that a wide range of light frequencies (up to $\sim$ 1000 cm^{-1} with 1800 gratings and $\sim$ 3500 cm^{-1} with 600 gratings) can be detected in a single acquisition.

In the present experiment, a JobinYvon LabRam 1800 single grating spectrometer was used, and the measurement conditions are listed in Table. 2.5.

2.6.2 Data Analysis

As mentioned in 2.4, the phonon spectrum is characterized by its integrated intensity, frequency, linewidth and lineshape. In particular, the frequency of the phonon is considered as the most important parameter in the phonon spectrum. Experimentally, the phonon frequency is typically written in wavenumber; which is units of inverse length (cm^{-1}), and is written as

$$\Delta\omega = 10^7 \times \left(\frac{1}{\lambda_0} - \frac{1}{\lambda_R}\right) \tag{2.46}$$

where $\Delta\omega$ (cm^{-1}) is the Raman shift expressed in wavenumbers, λ_0 (nm) is the laser wavelength used for the excitation, and λ_R (nm) is the wavelength of the Raman spectrum.

Laser	Filter	Hole	Slit	Acquisition	Grating	Objective
632.817 nm	D0.6 ($<$ 1 mW)	1000 μm	100 μm	4 $\times$ 300 sec (20 min)	1800	50$\times$ ($\sim$ 5 μm spot size)

Table 2.5: Measurement conditions of the micro-Raman setup for the present work.

- **Neon correction**

In the experiment, the measured frequency of the phonon depends on the calibration of the spectrometer, as the spectrometer has a systematic inaccuracy of ~ 1 cm^{-1}. Without reference measurement one would see the same phonon at a different frequency, when one uses a different spectrometer. A reference frequency, which does not depend on the environment of the experiment, is required to overcome this error. In general, Argon or Neon gas emission lines are used to calibrate the spectrometer, as they are tabulated (53). In present work, I have used a line of $\lambda_N = 6{,}421.7108$ nm which is found at $\Delta\omega = 182.84$ (cm^{-1}) in the Raman spectrum. Therefore, Neon emission lines were recorded between measurements at different temperatures.

- **Fitting**

Most of the Raman peaks presented in this work could be well fitted by Lorentzian profiles (46), because the phonon damping in the materials investigated is dominated by anharmonic decay (see Sec. 2.4.1). If the width of the phonon profile is comparable to the instrumental resolution (which is approximately described by a Gaussian), a Voigt profile must be used. The Voigt profile is a line profile resulting from the convolution of Gaussian and Lorentzian profiles, and is defined as

$$V(x) = \int_{-\infty}^{\infty} G(x')L(x - x')dx' \tag{2.47}$$

where $G(x')$ and $L(x - x')$ represent the Gaussian and Lorentzian profiles, respectively. In the present work, the Gaussian line of 2 cm^{-1} FWHM was used to fit the data. In addition, the fitting error bars were estimated manually (usually, ~ 0.5 cm^{-1} for the frequency and ~ 1 cm^{-1} for the linewidth).

3

$\mathbf{Fe_{1+y}Te_{1-x}Se_x}$

3.1 Introduction

The recently discovered iron chalcogenide $Fe_{1+y}Te_{1-x}Se_x$ (11-type) is a remarkable family among iron-based superconductors due to several distinct features: (i) the simplest structure among iron-based superconductors, (ii) a different magnetic structure which can not be explained within the simple Fermi nesting-induced itinerant spin-density-wave (SDW) scenario, and (iii) $Fe_{1+y}Te_{1-x}Se_x$ does not contain any arsenic and is therefore less toxic. This indicates the arsenic is not essentially necessary to introduce superconductivity in iron-based superconductors. Despite these features and even though the chemical doping mechanism is quite different from that of other families of iron-based superconductors, it has a very similar phase diagram and displays analogous superconducting properties.

In this chapter, I will report on experiments I have performed with Raman scattering spectroscopy to understand the nature of the lattice dynamics of iron chalcogenide $Fe_{1+y}Te_{1-x}Se_x$. In Sec. 3.2, I will discuss general properties and issues in $Fe_{1+y}Te_{1-x}Se_x$, and in Sec. 3.3, I will summarize prior Raman scattering studies. In Sec. 3.4, I will introduce the samples which are used in this work, and in Sec. 3.5, 3.6, 3.7, I will discuss our experimental observations, and then finally, in Sec. 3.8, I will state conclusions.

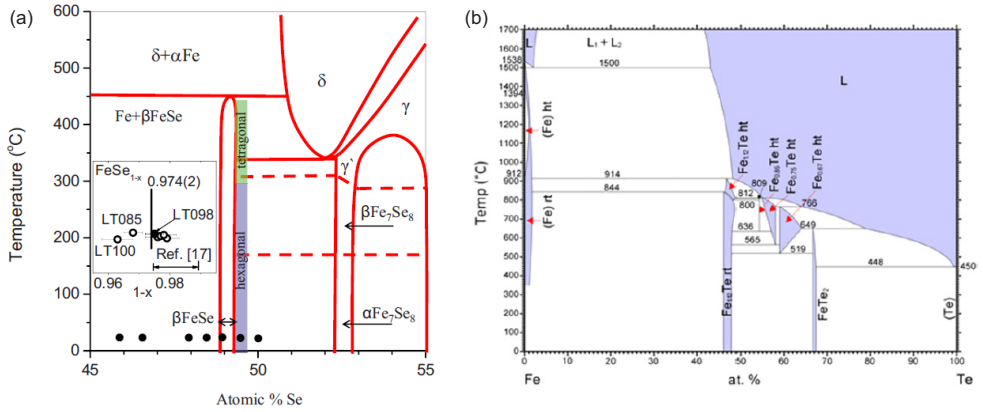

Figure 3.1: Phase diagram of Fe - Se and Fe - Te system - (a) Complex phase of FeSe system from Ref. (54) (b) FeTe system from Ref. (55)

3.2 Properties and Issues in $Fe_{1+y}Te_{1-x}Se_x$

3.2.1 Crystal Structure

When superconductivity in iron chalcogenides FeSe and FeTe was discovered, iron chalcogenides were considered as the simplest iron-based superconductors as they consist only of tetrahedral layers containing iron and selenium or tellurium without any separating atoms or building blocks (14, 15, 16). In fact, iron chalcogenides have been synthesized and studied a long time ago (56, 57, 58). In particular, $Fe_{1+y}Te$ was known as an antiferromagnetic (AFM) compound already in the 1970's (59). However, the phase diagram of these compounds is complex, and it is difficult to synthesize the stoichiometric compounds (see Fig. 3.1) (54, 55).

Fig. 3.2 shows the crystal structure of $Fe_{1+y}Te/Se$ at room temperature. The parent $Fe_{1+y}Te/Se$ compound adopts the tetragonal anti-PbO-type structure (space group P4/nmm (D_{4h}^7)) with Fe, Te/Se, and excess Fe atoms which occupies an additional Fe(2) site on the Te/Se plane located at the 2a, 2c, and 2c Wyckoff positions, respectively. The lattice parameters are a = 3.826 Åand c = 6.273 Å (60). Two iron and two tellurium atoms (one iron and one tellurium atoms) are present in the tetragonal unit cell (primitive unit cell). The Fe(1) and Te/Se sites are fully occupied while the interstitial Fe(2) sites are partially occupied by iron excess on the Te/Se plane. The iron concentration varies from 0.9 to 1.14 (but the parent compound always contains iron excess ($y \leq 0.02$)), depending on the sample preparations (61, 62, 63, 64, 65, 66, 67, 68, 69).

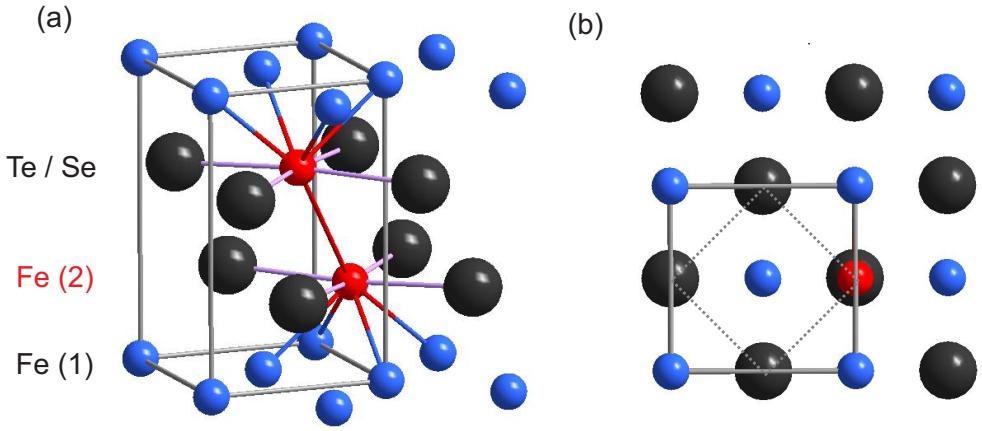

Figure 3.2: Crystal structure of $Fe_{1+y}Te_{1-x}Se_x$ - Tetragonal anti-PbO-type structure (space group P4/nmm (D_{4h}^7)). The blue, red, black atoms and gray line represent the Fe(1), Fe(2), Te/Se atoms and the unit cell, respectively. Two iron and two tellurium atoms are present in the tetragonal unit cell. The Fe(1) and Te/Se sites are fully occupied while the interstitial Fe(2) sites are partially occupied by iron excess. The iron excess are located on the Te/Se plane. (a) 3D view. (b) Top view. The gray dashed line represents the primitive unit cell containing one iron and one tellurium atoms

For instance, single crystals grown using the Bridgman method usually contain a relatively large amount of interstitial iron ($y \geq 0.07$) compared to those grown using a self-flux method ($y \leq 0.04$) (70). As we shall discuss later (see Sec. 3.2.4), this influences quite dramatically the structural, magnetic and superconducting properties of these compounds (60, 61, 62, 63, 64, 71). Below structural transition ($T_s \sim 70$ K), the tetragonal $Fe_{1+y}Te$ distorts to the orthorhombic or monoclinic structure (62) (see Sec. 3.2.4).

3.2.2 Electronic and Magnetic Structure

The resistivity of $Fe_{1+y}Te$ slowly increases with decreasing temperature, but below the magnetic transition the resistivity steeply drops down and then shows metallic behavior (see Fig. 3.3(a)) (63). Furthermore, the magnetic transition is accompanied by a structural transition as shown in Fig. 3.3(c)(d) (61).

- **Electronic structure**

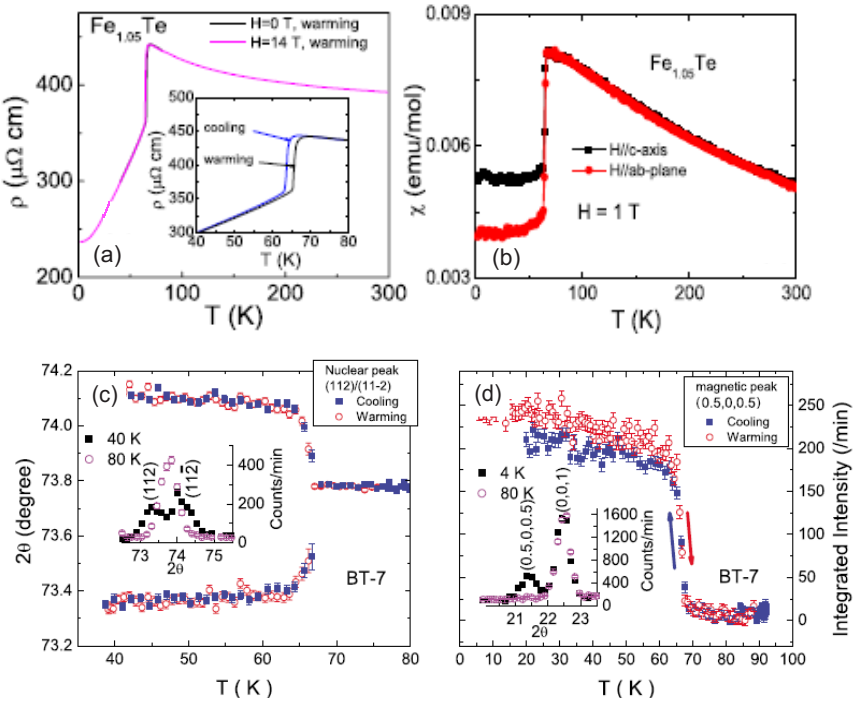

Figure 3.3: Structural and magnetic transitions in $Fe_{1+y}Te$ - (a) (b) The in-plane resistivity and magnetic susceptibility of $Fe_{1.05}Te$, respectively from Ref. (63). The magnetic transition occurs at $\sim$ 65 K. (c) (d) Splitting of nuclear peaks and intensity of magnetic Bragg peak of of $Fe_{1.07}Te$, respectively from Ref. (61). Structural and AFM transitions occur at the same temperature of $\sim$ 67 K.

The initial band structure calculations predicted a similar Fermi surface topology to that of other iron pnictides (two hole pockets at the Γ point and two electron pockets at the M point) as shown in Fig. 3.4(72), and this has been confirmed by several Angle-resolved photoemission spectroscopy (ARPES) measurements (see Fig. 3.5) (66, 69, 73). One would therefore expect the 11 compound to have electronic and magnetic properties similar to those of other families of iron pnictides.

- **Magnetic structure**

Magnetically ordered iron pnicties typically have small magnetic moments ($\sim$ 0.4 - 1.0 μ_B/iron) and a collinear AFM stripe order along (π,π) in the tetragonal unit cell, which coincides approximately with the Fermi surface nesting vector (20, 26, 74). Interestingly, contrary to the iron pnictides, $Fe_{1+y}Te$ compounds have large magnetic

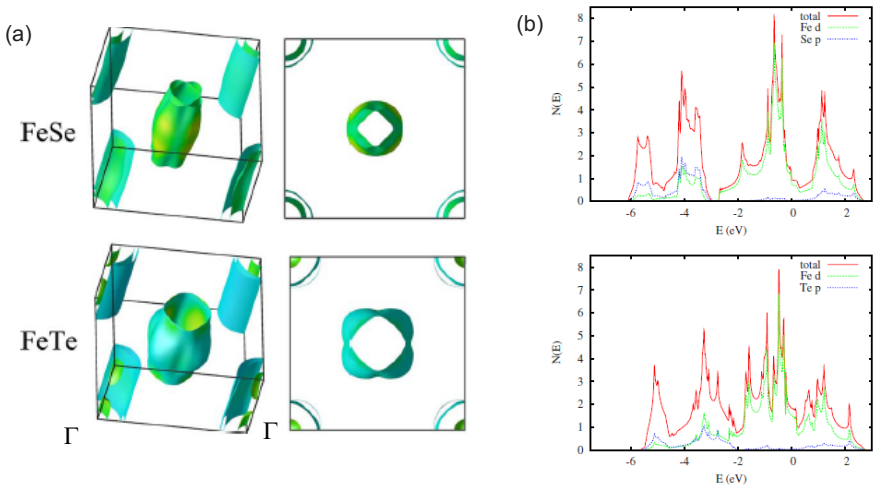

Figure 3.4: Electronic structure of iron chalcogenides - Electronic structure of FeSe/Te from Ref. (72). (a) LDA Fermi surface of FeSe and FeTe. The corners are Γ points. (b) Electronic density-of-state (DOS).

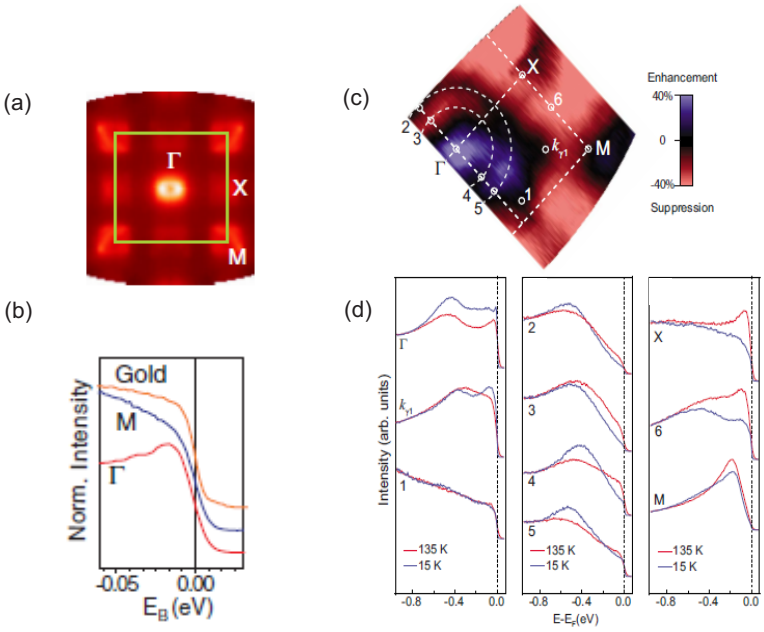

Figure 3.5: Fermi surface topology of $Fe_{1+y}Te$ - (a) (b) Fermi surface of $Fe_{1+y}Te$ and the energy distribution curves (EDCs) at 10 K from Ref. (66). (c) (d) Fermi surface of $Fe_{1.06}Te$ and the EDCs from Ref. (69). Both ARPES measurements indicate the absence of SDW gap.

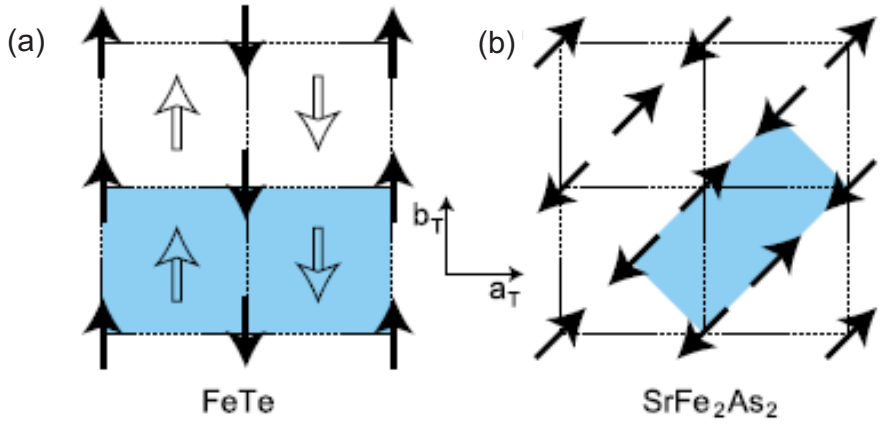

Figure 3.6: Magnetic structure of $Fe_{1+y}Te$ - Schematic in-plane spin structure for 11 and 122 from Ref. (61). (a) Double AFM stripe along (π,0) in the tetragonal unit cell rotated by 45° from the nesting vector is present in $Fe_{1+y}Te$. (b) Collinear AFM stripe along (π,π) in the tetragonal unit cell in 122 families. The shaded area represents the magnetic unit cell.

moments ($\sim$ 2.0 - 2.5 μ_B) and a double AFM stripe order along (π,0) in the tetragonal unit cell, *i.e.* rotated by 45° from the nesting vector (see Fig. 3.6) (59, 61, 75). Moreover, ARPES measurements have observed no Fermi nesting-induced SDW gap along the magnetic ordering vector (π,0) (see Fig. 3.5) (66, 69). However, a magnetic moment of 2.0 μ_B is very large for an itinerant system. A simple itinerant nesting picture, which is widely accepted for the iron pnictides, can not account for these different magnetic features. Recent first principles calculations have highlighted the importance of local moments and Hund's exchange coupling. These calculations provide better agreement with the experimental observations (76, 77).

3.2.3 Superconducting State

- **Chemical doping**

In most iron-based superconductors, superconductivity appears upon chemical doping of a stoichiometric compound. Usually, chemical doping means the introduction of additional charge carriers (electrons or holes) into the system, and is achieved by substituting existing atoms with non-isovalent atoms. Along with LiFeAs (see Chap. 4), FeSe appears to be a rare example of a stoichiometric iron-based superconductors. In this system, the substitution of non-isovalent atoms does not enhance, but rather destroys

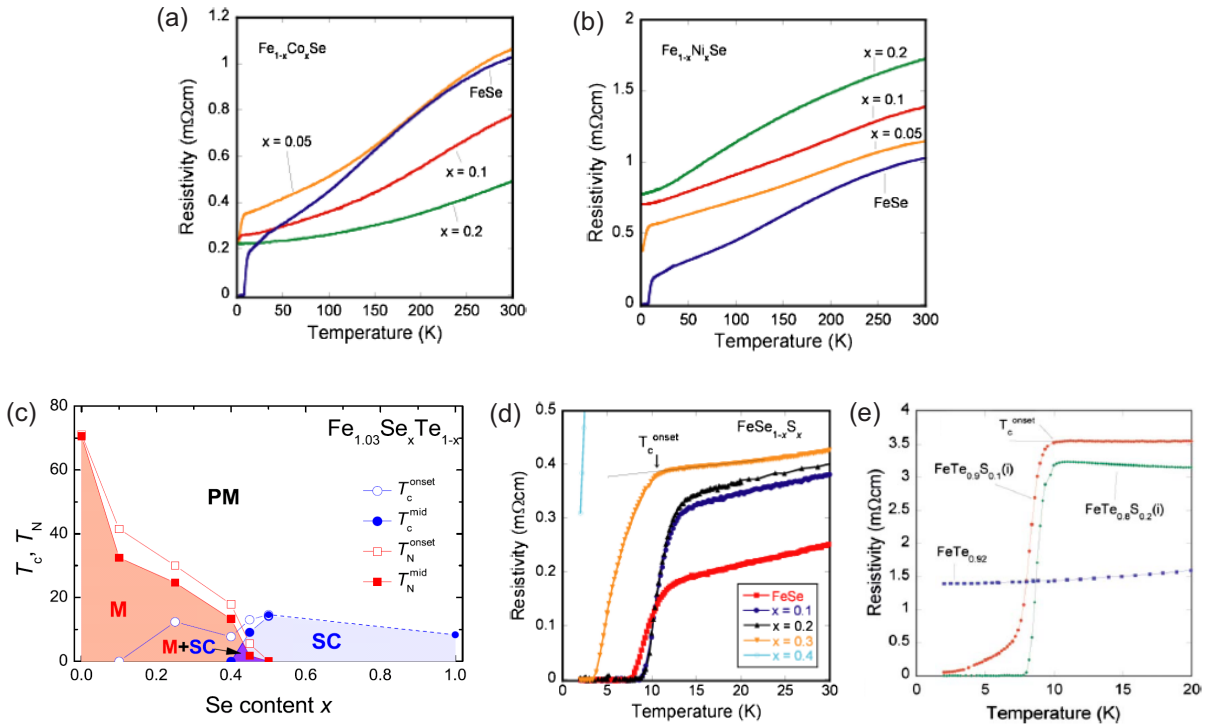

Figure 3.7: Superconductivity in chalcogenides upon chemical doping - (a) (b) Superconductivity of FeSe as a function of Co and Ni doping at Fe site from Ref. (78), respectively. Superconductivity is gradually suppressed upon Co and Ni doping. (c) Phase diagram of $Fe_{1.03}Te_{1-x}Se_x$ as a function of Se contents from Ref. (64). Upon Se doping, superconductivity appears with suppressing the static magnetic order. Superconductivity and short-range magnetic order coexist in $0.2 \leq$ Se ≤ 0.5 region. (d) Superconductivity of $FeSe_{1-x}S_x$ as a function of S contents from Ref. (78). (e) Superconductivity of $FeTe_{1-x}S_x$ as a function of S contents from Ref. (79). In both (d) and (e) cases, superconductivity enhances upon S doping.

superconductivity as shown in Fig. 3.7(a)(b), where substituting Co or Ni to Fe site gradually suppresses superconductivity, in contrast with other families of iron pnictides where superconductivity is enhanced by Co or Ni substitution (78, 79, 80, 81, 82).

Interestingly, in iron chalcogenides, superconductivity appears when isovalent atoms (Se, S) are substituted to Te without introducing any additional charge carriers into the system. Fig. 3.7(c) shows the phase diagram of $Fe_{1.03}Te_{1-x}Se_x$ as a function of Se contents. Upon substitution of isovalent Se at the Te 2b Wyckoff position, the static magnetic order accompanying the structural transition is progressively suppressed and superconductivity appears with a $T_c^{max} \sim 14$ K (at ambient pressure) at the optimum

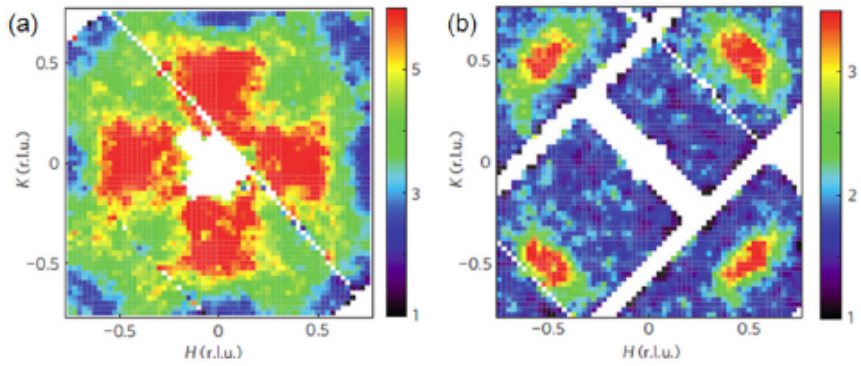

Figure 3.8: Magnetic excitations in $Fe_{1+y}Te_{1-x}Se_x$ - (a) Magnetic excitation in non-superconducting $Fe_{1.04}Te_{0.73}Se_{0.27}$ at (π,0) at 5 K. (b) Resonant spin excitation in superconducting $FeTe_{0.51}Se_{0.49}$ at (π,π) at 3.5 K from Ref. (83).

doping (Se $\sim$ 0.5) (15, 16). Interestingly, in certain region (0.2 $\leq$ Se $\leq$ 0.5), superconductivity coexists with the magnetic order and survives even in $Fe_{1+y}Se$ (14, 64). Similar to Se substitution, superconductivity also appears upon substituting S to Se/Te site. In $FeSe_{1-x}S_x$, superconductivity is enhanced up to 0.2 of S doping and then is suppressed, and in $FeTe_{1-x}S_x$, superconductivity appears upon S doping, as well (see Fig. 3.7(d)(e)) (78, 79).

- **Magnetic excitations and superconducting gap**

Fig. 3.8 shows magnetic excitations in non-superconducting and superconducting $Fe_{1+y}Te_{1-x}Se_x$. In non-superconducting $Fe_{1.04}Te_{0.73}Se_{0.27}$, it is clearly shown that the spectral weight is mostly centered at (π,0), as in $Fe_{1+y}Te$ where the magnetic order is present. However, in superconducting $FeTe_{0.51}Se_{0.49}$, a resonant spin excitation was observed in the superconducting state at (π,π), where the resonance spin excitations are observed in several other families of iron pnictides (36, 84, 85). Such a resonant spin excitation in the superconducting state indicates the sign change of the superconducting gap function (35), and therefore a simple isotropic s_+-wave gap can be ruled out and a nodal d-wave or isotropic $s_\pm$-wave gap can be the possible gap function.

The superconducting gap size has been measured by several techniques: ARPES ($\Delta \sim$ 4 meV) (73), scanning tunneling microscopy (STM) ($\Delta \sim$ 1.7 meV (86), 1 meV (87), and 2.3 meV (88)), nuclear magnetic resonance (NMR) ($\Delta \sim$ 1.5 meV) (89), and specific heat ($\Delta \sim$ 3 meV) (67). In ARPES measurements, a clear isotropic gap

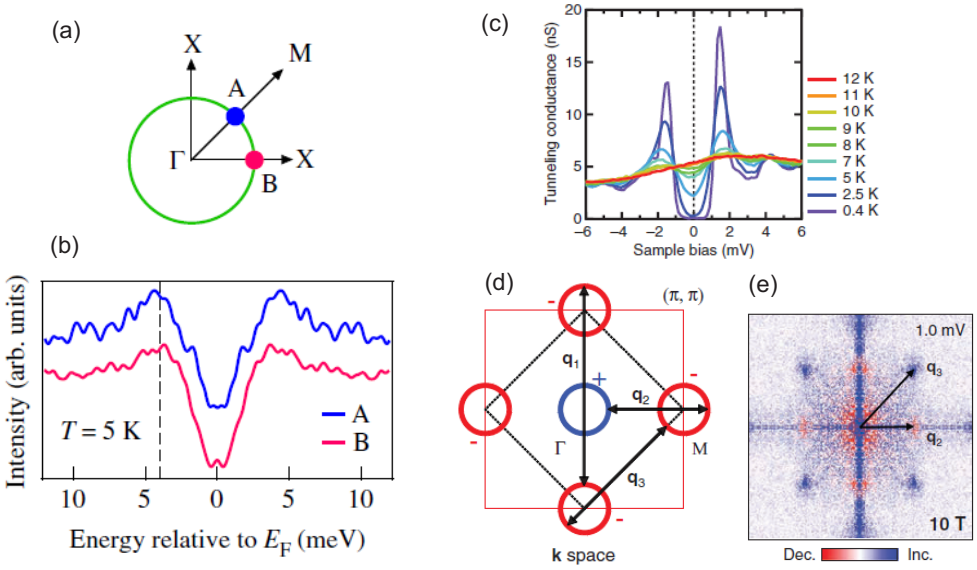

Figure 3.9: Superconducting gap in $Fe_{1+y}Te_{1-x}Se_x$ - (a) (b) Superconducting gap of $Fe_{1.03}Te_{0.7}Se_{0.3}$ at 5 K measured along (π,π) and (π,0) by ARPES from Ref. (73). The isotropic superconducting gaps ($\Delta \sim 4$ meV) are present. (c) Superconducting gap ($\Delta \sim 1.7$ meV) measured by STM at 0.4 K from Ref. (86). (d) A schematic of possible inter-Fermi pocket scattering. $\mathbf{q}_1$ is umklapp process, $\mathbf{q}_2$ ($\mathbf{q}_3$) denotes scattering between electron and hole pockets (electron and electron pockets) from Ref. (86). (e) Magnetic field-induced QPI at 1.5 K. The intensity of $\mathbf{q}_2$ increases while the intensity of $\mathbf{q}_3$ decreases with applying magnetic field. The opposite behavior of $\mathbf{q}_2$ and $\mathbf{q}_3$ under magnetic field indicates the sign change of superconducting gap function.

without any evidence of nodes has been observed, and therefore a nodal d-wave gap can be ruled out (73).

Insight into the superconducting gap symmetry can also be gained from quasiparticle interference (QPI) pattern by STM experiment. In general, the momentum-dependent energy dispersion $\varepsilon(\mathbf{k})$ can not be measured by STM, as STM is a real space imaging technique and allows one to measure the momentum-integrated local density-of-states (LDOS). However, when impurities or crystal defects are present in a sample, they cause elastic scattering which mixes the eigenstates of quasiparticles with different $\mathbf{k}$. As a consequence, quasiparticles with different $\mathbf{k}$ form a standing wave, and interference patterns (so-called QPI pattern) appear in the Fourier-transformed STM images (90). By applying magnetic field, vortices are formed and provide the magnetic field dependent QPI patterns (91). The magnetic field dependent QPI intensities in

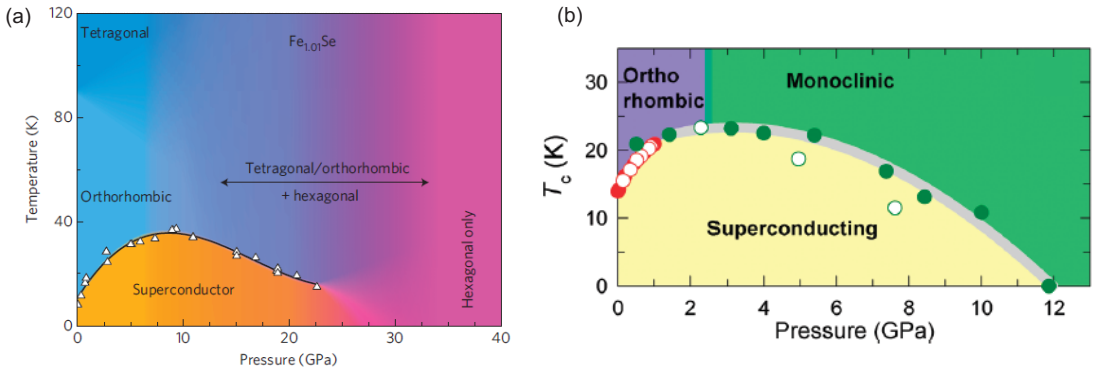

Figure 3.10: Superconductivity in $Fe_{1+y}Se_{1-x}Te_x$ under high pressure - (a) High pressure Phase diagram of $Fe_{1.01}Se$ from Ref. (92). (b) High pressure Phase diagram of $Fe_{1.03}Se_{0.57}Te_{0.43}$ from Ref. (93).

superconductors give an insight into the coherence factor which is related with the phase of superconducting gap. In particular, by increasing magnetic field, QPI intensities from same superconducting gap phase are enhanced, while the QPI intensities from different gap phase are suppressed for d-wave superconductors (91).

In $Fe_{1+y}Te_{1-x}Se_x$, such magnetic field dependent QPI pattern has been studied by Ref. (86). As applying magnetic field, QPI intensity between electron and hole pockets $\mathbf{q}_2$ decreases, while QPI intensity between electron and electron pockets $\mathbf{q}_3$ increases (see Fig. 3.9(e)) (86). This observation suggests the sign change of superconducting gap symmetry between electron and hole pockets, in good agreement with the argument based on the presence of the resonant spin excitations in neutron scattering measurement (83). Taken together, in the $Fe_{1+y}Te_{1-x}Se_x$ system, the superconducting gap function is an isotropic $s_{\pm}$-wave symmetry like that of other families of iron pnictides. This indicates a similar superconducting mechanism in all iron-based superconductors even though the magnetic structures of their parent compounds are different.

- **High pressure**

Superconductivity can also be achieved by applying pressure as shown in Fig. 3.10. The superconducting phase boundary has a dome shape and the optimum pressure depends on the chemical composition ($P^{optimal} \sim 10$ GPa for $Fe_{1.01}Se$ and 2 GPa for $Fe_{1.03}Se_{0.57}Te_{0.43}$). In both cases, superconductivity appears with a $T_c \sim 8$ K and 14 K, respectively, in an orthorhombic structure at ambient pressure, and upon applying

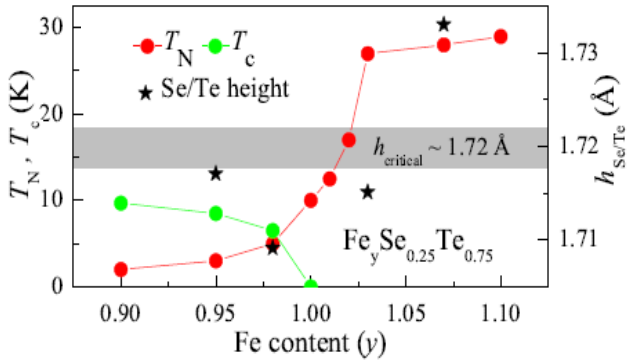

Figure 3.11: Phase diagram of $Fe_yTe_{0.75}Se_{0.25}$ - Phase diagram as a function of iron excess contents from Ref. (60). Upon increasing iron excess, the magnetic order enhances with suppressing superconductivity.

pressure, T_c is enhanced up to $T_c^{max} \sim 37$ K and 23 K, respectively, in the orthorhombic structure. After that, a structural phase transition occurs from orthorhombic to tetragonal or monoclinic with decreasing T_c under high pressure (92, 93). Taken together with the chemical doping effect, those observations strongly suggest that structural degree of freedom plays a crucial role in iron chalcogenides. Thus a systematic study of the lattice dynamics can shed a new light on these compounds.

3.2.4 Iron Excess

Before discussing the studies of lattice dynamics in this compound, here I want to point out the influence of iron excess. Recently, numerous reports have demonstrated the importance of the amount of the iron excess in the pure, but also in the Se-substituted $Fe_{1+y}Te_{1-x}Se_x$ compound (60, 62, 64, 68, 69, 71, 94, 95, 96). $Fe_{1+y}Te$ with a small iron excess concentration ($y \leq 0.1$) exhibits a coupled magnetic-structural transition to a commensurate AFM order with a tetragonal-to-monoclinic structural transition, while for higher iron excess ($y \geq 0.1$) incommensurate AFM order and a tetragonal-to-orthorhombic structural transition appear (61, 62).

Fig. 3.11 shows the phase diagram of $Fe_yTe_{0.75}Se_{0.25}$ as a function of iron contents. In iron deficient samples ($y \sim 0.9$), superconductivity is dominant even though the Se doping is quite far from the optimum doping (Se concentration ~ 0.5). When the amount of iron increases, the magnetic order becomes stronger and superconductivity becomes weaker. Superconductivity is completely suppressed in the region where the

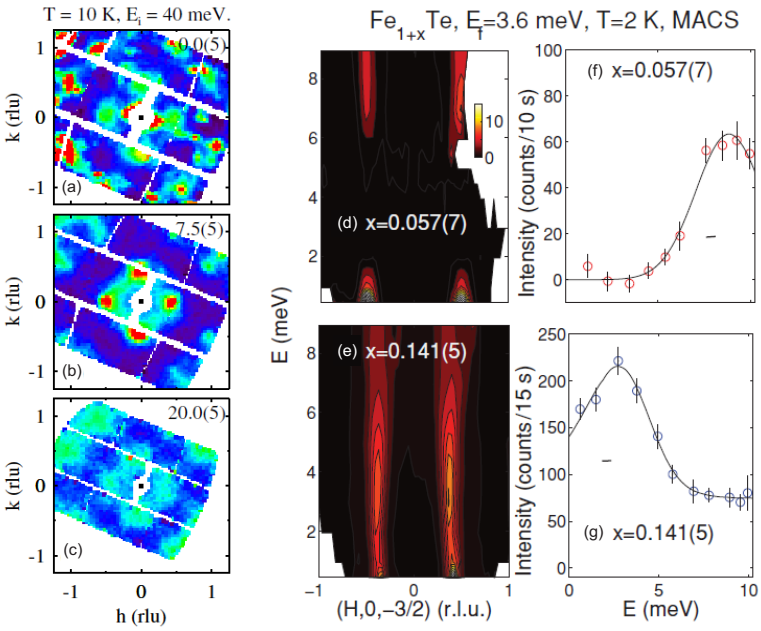

Figure 3.12: Magnetic excitations in parent $\mathbf{Fe_{1+y}Te}$ - (a) (b) (c) Magnetic excitations in parent $Fe_{1.1}Te$ at 10 K for energy transfers 0 meV, 7.5 meV and 20, respectively from Ref. (75). The magnetic excitations are centered at (π, 0). (d) (e) (f) (g) Magnetic excitations in parent $Fe_{1+y}Te$ with different iron excess at 2 K from Ref. (71). (d) (f) The magnetic excitation in less iron excess $Fe_{1.057}Te$ is gapped with a value of 7 meV. (e) (g) The magnetic excitation in rich iron excess $Fe_{1.141}Te$ is gapless with a excitation peak at 4 meV.

iron excess is present (60). Moreover when rich iron excess is present, it leads to the appearance of weakly localized magnetic states (96) and strong magnetic fluctuations as shown in Fig. 3.12(d)-(g), where magnetic excitations in parent $Fe_{1+y}Te$ with different iron excess are present (71). For a small amount of iron excess $Fe_{1+y}Te$, the magnetic excitation spectrum is gapped with a value of 7 meV, and as increasing the amount of iron excess, such gapped magnetic excitation spectrum is completely filled by the low energy spin fluctuations.

3.3 Prior Raman Scattering Studies

Raman spectroscopy is a powerful tool which allows the systematic studies of lattice dynamics. The first Raman scattering study in iron chalcogenids has been reported by Xia et al. in Ref. (65) on single crystal FeTe and superconducting $Fe_{1.03}Te_{0.7}Se_{0.3}$ at

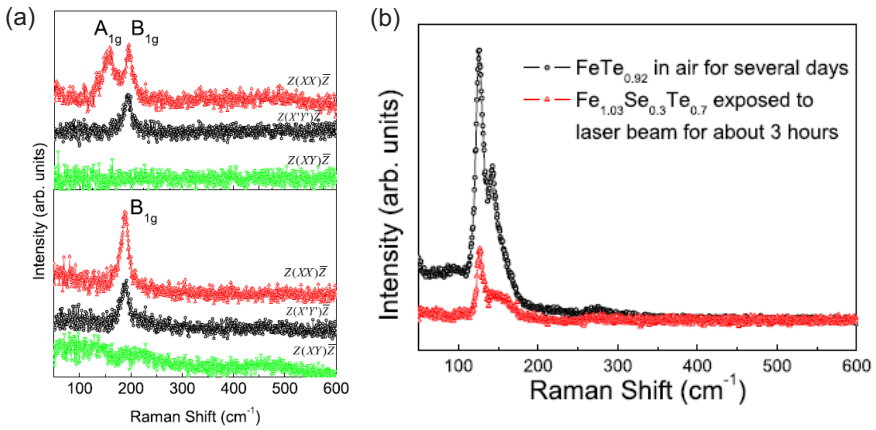

Figure 3.13: First Raman scattering study on $Fe_{1+y}Te_{1-x}Se_x$ - (a) Raman spectra on parent FeTe and superconducting $Fe_{1.03}Te_{0.7}Se_{0.3}$ at room temperature from Ref. (65). A_{1g}(Te/Se) and B_{1g}(Fe) modes are observed and A_{1g}(Te/Se) disappears in Se-doped sample. (b) Aging effect of $Fe_{1+y}Te_{1-x}Se_x$.

room temperature as shown in Fig. 3.13. The main findings in this paper are (i) $\sim$ 159 cm^{-1} and $\sim$ 196 cm^{-1} peaks can be assigned to the A_{1g}(Te/Se) mode and B_{1g}(Fe) mode at room temperature, respectively, and (ii) the A_{1g}(Te/Se) mode disappears in Se-doped sample, which is a very surprising effect as the isovalent substitution of Se to Te does not change the crystal structure and the mode therefore should exist. In addition, they have reported (iii) a strong aging effect (see Fig. 3.13(b)), and claimed the formation of amorphous Te is the origin of the strong decomposition peak rather than TeO_2 on the basis of earlier reports (97, 98).

Fig. 3.14 shows several Raman scattering studies on $FeSe_{1-x}$ compounds. The studies in Ref. (99) and Ref. (100) have been performed on polycrystalline samples (Fig. 3.14(a)(b)), and the study in Ref. (101) has been performed on a single crystal sample (Fig. 3.14(c)(d)). Two very sharp and intense phonon peaks are observed at $\sim$ 183 cm^{-1} and $\sim$ 207 cm^{-1} at 7 K on the single crystal $FeSe_{0.96}$. On the other hand, several phonon peaks (more than the expected number of phonon modes) are detected on polycrystals. Some of them are broad and their positions are different from the positions obtained from the single crystal. This suggests that extraneous phases were contained in the samples. Therefore not only high quality samples but also cautious sample treatment are required to study the complex phase diagram of this compound (see Fig. 3.1) (54, 55) and its decomposition (65).

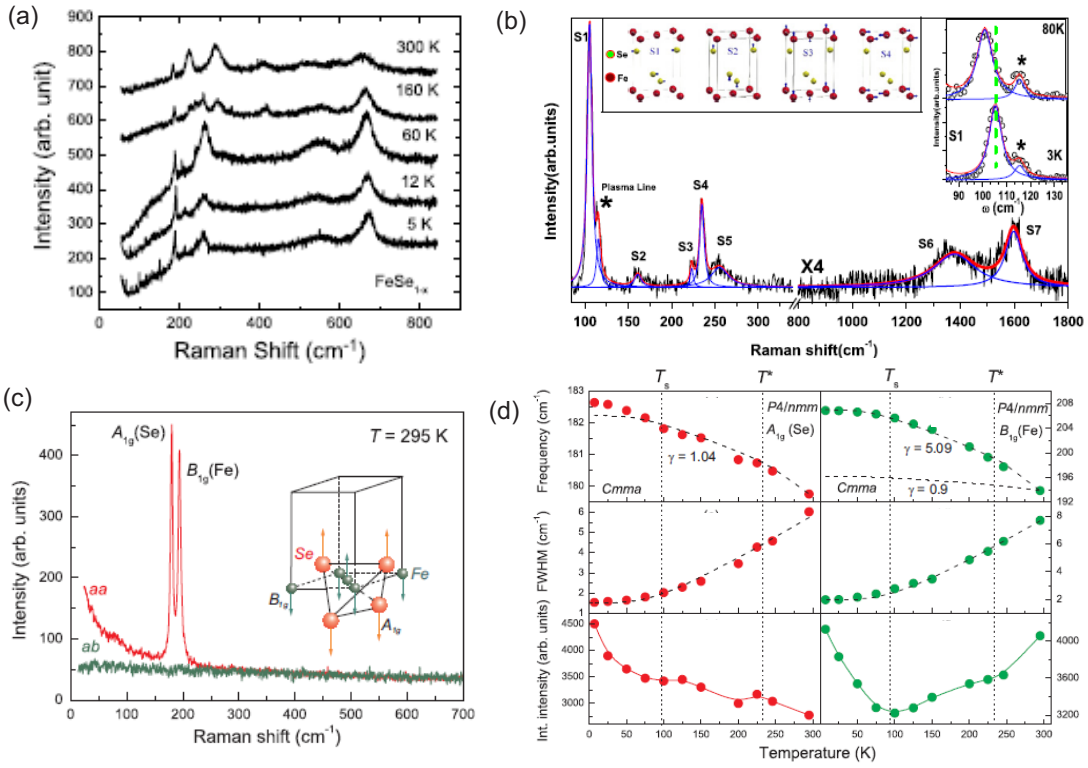

Figure 3.14: Several Raman scattering studies on superconducting $FeSe_{1-x}$ - (a) Raman spectrum on $FeSe_{0.82}$ at 3 K from Ref. (99). (b) Raman spectra on $FeSe_{1-x}$ for several temperatures from Ref. (100). (c) (d) Raman spectrum on $FeSe_{0.96}$ and the temperature dependence of A_{1g}(Se) and B_{1g}(Fe) modes from Ref. (101).

Fig. 3.15 shows the results of several Raman scattering studies on $Fe_{1+y}Te_{1-x}Se_x$ compounds. All Raman studies show the same two Raman active phonon modes (A_{1g}(Te) and B_{1g}(Fe) modes) in agreement with Ref. (65) except for the study from Ref. (104) (see Fig. 3.15(d)). The temperature dependence study for parent $Fe_{1+y}Te$ has done by Gnezdilov et al. in Ref. (102), where they observed (i) a large linewidth of A_{1g} mode, (ii) phonon renormalization across the SDW transition, and (iii) an abnormal increase of the linewidth of the B_{1g} mode with decreasing temperature. The authors claimed that the large line shape of Te A_{1g} phonon originates from a spin-orbital frustration while the Fe B_{1g} phonon remains essentially unaffected by the spin-orbital frustration. However, no claims are made for the origin of the abnormal temperature dependence of the linewidth of the B_{1g} mode.

Okazaki et al. in Ref. (103) have studied metallic $Fe_{1.074}Te$ and superconducting

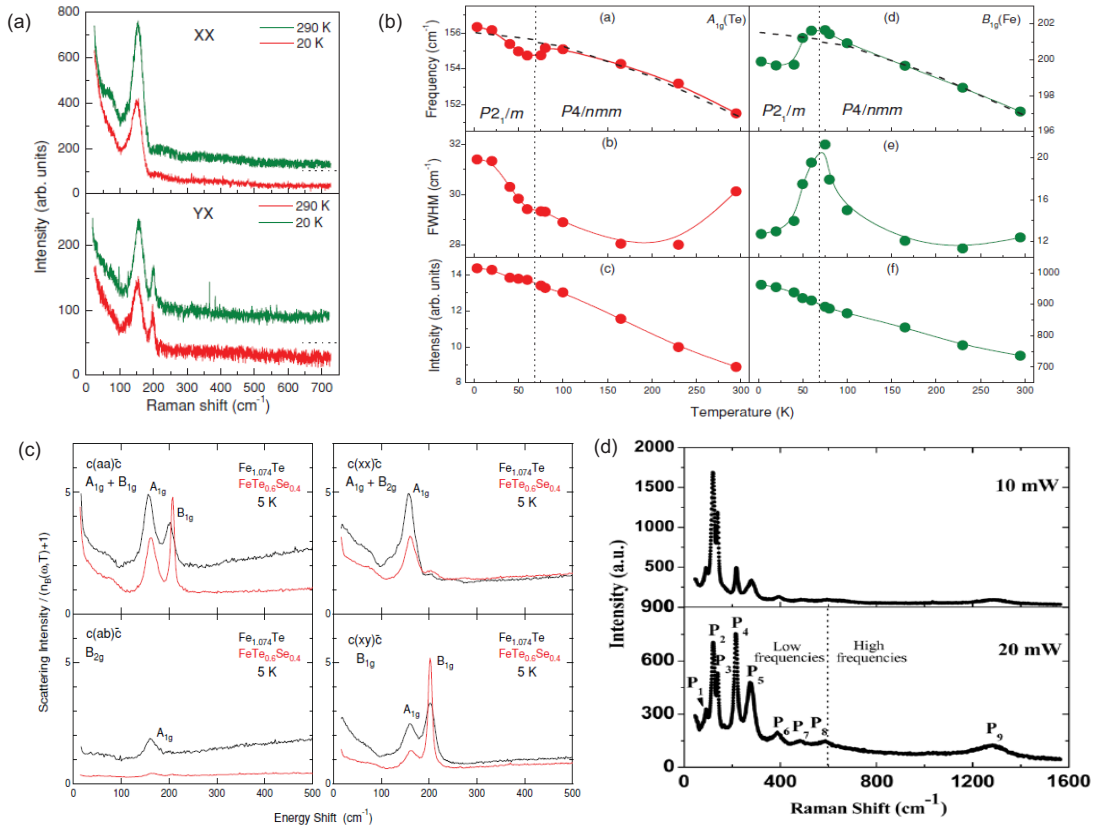

Figure 3.15: Several Raman scattering studies on $Fe_{1+y}Te_{1-x}Se_x$ - (a) (b) Raman spectrum on $Fe_{1.05}Te$ and the temperature dependence of A_{1g}(Te) and B_{1g}(Fe) modes from Ref. (102) (c) Raman spectra on parent $Fe_{1.074}Te$ and superconducting $FeTe_{0.6}Se_{0.4}$ at 5 K and room temperature from Ref. (103). (d) Raman spectra on superconducting $FeTe_{0.5}Se_{0.5}$ at room temperature from Ref. (104).

$FeTe_{0.6}Se_{0.4}$ samples. They observed a more intense and sharper B_{1g} phonon in the Se-doped sample than in the Se-free sample, but no systematic study of the Se doping dependence was performed.

So far, the available Raman data on $Fe_{1+y}Te_{1-x}Se_x$ single crystals is limited. In particular, no systematic studies of the influence of Se doping and excess iron concentration on the lattice dynamics have been carried out. This motivates the present our work where the influence of Se doping and excess iron concentration on the lattice dynamics are separately investigated by measuring the Raman active c-axis polarized optical phonons of $Fe_{1+y}Te_{1-x}Se_x$ for various iron excess, y, and Se concentrations, x.

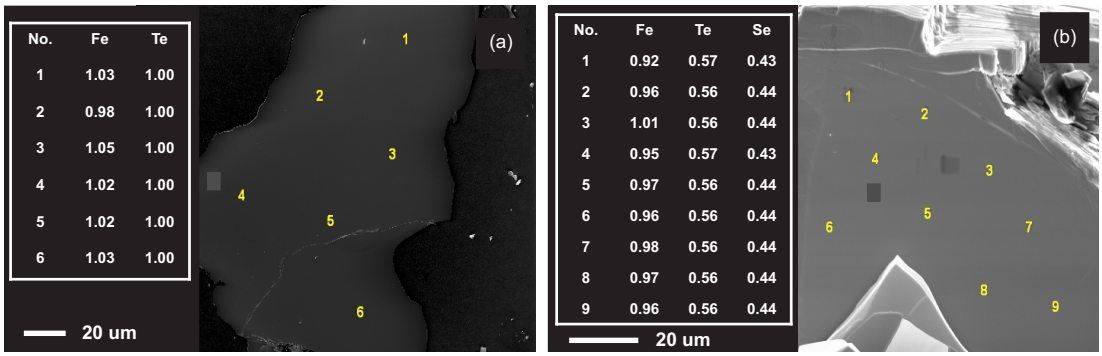

Figure 3.16: SEM image of $Fe_{1+y}Te_{1-x}Se_x$ - (a) SEM image of $Fe_{1.02}Te$ with chemical compositions determined by EDX. The 'No.' denotes the position where the EDX measurement has been performed. (b) SEM image of $Fe_{0.95}Te_{0.56}Se_{0.44}$ with chemical compositions.

3.4 Sample Characterizations

In order to disentangle the effects of iron excess and of Se doping, we have studied different groups of crystals, listed in Table 3.1. The first group comprises Se-free parent $Fe_{1+y}Te$ samples, and only the iron excess concentration was changed (FT1, FT2). The second group includes different Se concentration $FeTe_{1-x}Se_x$ samples, and the iron excess was kept as close to 1 as possible (FTS1, FTS2, FTS3 and FTS4). Finally, Se-doped samples containing iron excess ($Fe_{1+y}Te_{1-x}Se_x$) were investigated (FTS5 and FTS6).

Name	Sample composition	T_N	T_c
FT1	$Fe_{1.02}Te$	67 K	-
FT2	$Fe_{1.09}Te$	65 K	-
FTS1	$Fe_{1.00}Te_{0.78}Se_{0.22}$	-	11.5 K
FTS2	$Fe_{0.99}Te_{0.69}Se_{0.31}$	-	11 K
FTS3	$Fe_{0.98}Te_{0.66}Se_{0.34}$	-	10.5 K
FTS4	$Fe_{0.95}Te_{0.56}Se_{0.44}$	-	14 K
FTS5	$Fe_{1.05}Te_{0.58}Se_{0.42}$	-	11.5 K
FTS6	$Fe_{1.08}Te_{0.73}Se_{0.27}$	-	9 K

Table 3.1: A summary of the chemical compositions obtained by EDX and characteristic transitions temperatures of the various $Fe_{1+y}Te_{1-x}Se_x$ samples used in this study.

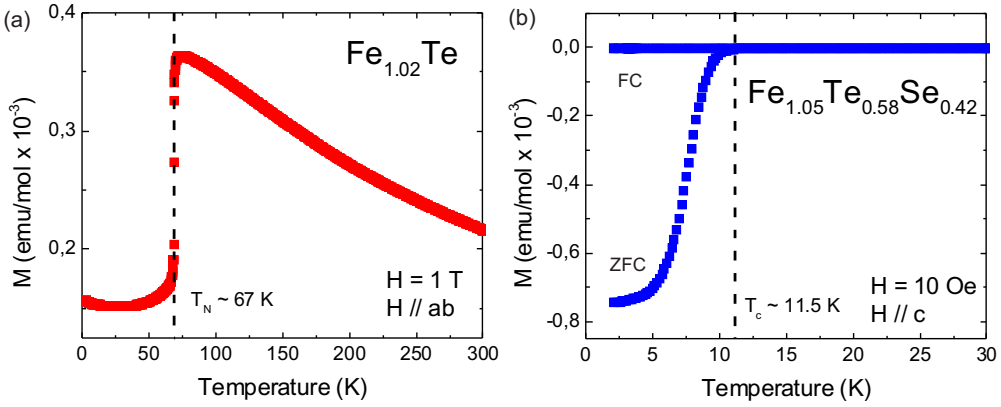

Figure 3.17: Magnetization on $Fe_{1+y}Te_{1-x}Se_x$ - (a) Magnetization curves on parent $Fe_{1.02}Te$ in a magnetic field of 1 T applied along ab-plane. The dashed line indicates the AFM transition temperature T_N of $\sim$ 67 K. (b) Zero field-cooled (ZFC) and field-cooled (FC) magnetization curves on superconducting $Fe_{1.05}Te_{0.58}Se_{0.42}$ in a magnetic field of 10 Oe applied along c-axis. The dashed line indicates the superconducting transition temperature T_c of $\sim$ 11.5 K.

Most of the $Fe_{1+y}Te_{1-x}Se_x$ single crystals were grown by Klein et al. using a sealed quartz tube and Bridgman methods as described in Ref. (67), and by Liu et al. using a self-flux and Bridgman methods as described in Ref. (70). A few pieces of sample were grown by Ganin et al. in Ref. (93, 105). The average chemical compositions listed in Table 3.1 were determined by Energy dispersive X-ray spectroscopy (EDX). Fig. 3.16 shows scanning electron microscope (SEM) images of samples with chemical compositions $Fe_{1.02}Te$ (FT1) and $Fe_{0.95}Te_{0.56}Se_{0.44}$ (FTS4). The EDX measurement can determine accurately the ratio of isovalent Te to Se concentration, while it is hard to determine the absolute iron concentration from the EDX. Nevertheless, we can effectively compare the relative iron concentrations of different samples. Typical AFM and superconducting transition temperatures T_N and T_c were measured by a superconducting quantum interference device (SQUID) as shown in Fig. 3.17, where clear AFM and superconducting transitions are observed at $\sim$ 67 K and $\sim$ 11.5 K, respectively.

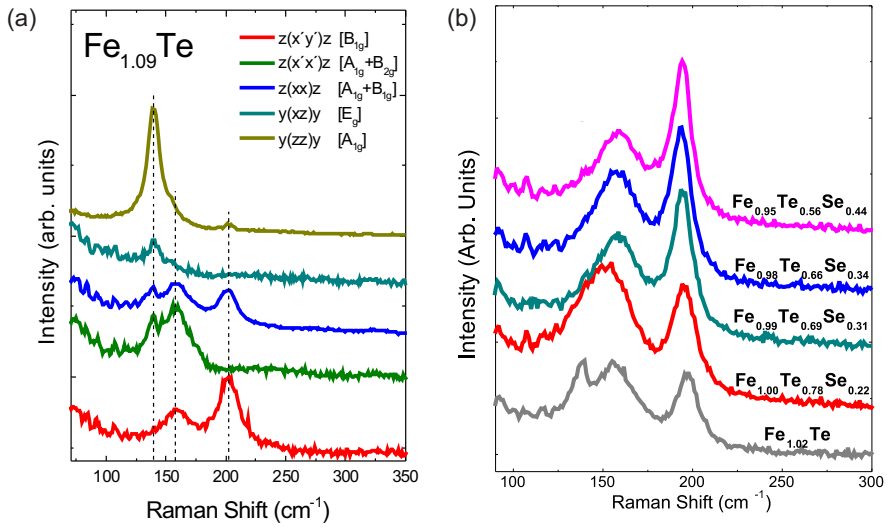

Figure 3.18: Mode assignment of $Fe_{1+y}Te_{1-x}Se_x$ - (a) Base temperature Raman spectra in $z(x'y')z$, $z(x'x')z$, $z(xx)z$, $y(xz)y$ and $y(zz)y$ configurations from FT1 sample. Spectra have been shifted vertically for clarity. Starting from the left, the peaks are assigned to 136 cm^{-1}, A_{1g}(Te) and B_{1g}(Fe) modes, and no E_g modes are observed. (b) Room temperature Raman spectra taken in $z(xx)z$ configuration from FT1, FTS1, FTS2, FTS3 and FTS4 samples (see Table 3.1). Spectra have been shifted vertically for clarity. The 136 cm^{-1} peak disappears in Se-doped samples.

3.5 Experimental Results

3.5.1 Experimental Conditions

All Raman light scattering experiments were performed on freshly cleaved surfaces, and the samples were mounted in a helium-flow cryostat. Spectra were taken in backscattering geometry through a JobinYvon LabRam 1800 single grating spectrometer, and a linearly polarized He^+/Ne^+ mixed gas laser with $\lambda = 632.817$ nm has been used for excitation. The power of the incident beam was less than 1 mW with a ~ 5 μm diameter spot on the sample surface.

3.5.2 Mode Assignment

As the lattice symmetry of stoichiometric FeTe is in the space group $P4/nmm$ (D_{4h}^7), with the Fe and Te atoms at the 2a and 2c Wyckoff positions, respectively, one would expect 12 zone-center phonon modes ($\Gamma_{FeTe} = 1A_{1g} + 1B_{1g} + 2A_{2u} + 2E_u + 2E_g$)

from group symmetry analysis [note that E_u and E_g modes are doubly degenerate] (44). Among them, 3 modes ($1A_{2u}$ + $1E_u$) are acoustic modes, 3 modes ($1A_{2u}$ + $1E_u$) are IR active modes and 6 modes ($1A_{1g}$, $1B_{1g}$ and $2E_g$) are Raman active modes. Fig. 3.18(a) shows Raman spectra on the parent $Fe_{1.09}Te$ (FT2) sample measured at 10 K for several scattering geometries with incident light wave vectors along the c-axis [$z(x'y')z$, $z(x'x')z$, $z(xx)z$ configurations], and along the b-axis [$y(zz)y$ and $y(xz)y$ configurations].

As discussed in Sec. 2.3, the measurements in the $z(x'y')z$, $z(x'x')z$, $z(xx)z$ configurations allow the phonon modes in the B_{1g}, A_{1g} + B_{2g} and A_{1g} + B_{1g} symmetries, respectively. Hence, we can effectively assign the modes at 136 cm^{-1}, 155 cm^{-1} and 197 cm^{-1} to the A_{1g}, A_{1g} (Te) and B_{1g} (Fe) c-axis polarized phonon modes, in agreement with previous reports (65, 102, 103), except for the mode at 136 cm^{-1}. The 136 cm^{-1} mode has not been observed in other Raman measurements (see Fig. 3.13) (65, 102, 103), but the mode is clearly visible in our measurement. I will discuss the origin of this mode later.

As the measurements in the $y(zz)y$ and $y(xz)y$ configurations allow the phonon modes in the A_{1g} and E_g symmetries, respectively, the weak peak at 136 cm^{-1} in $y(xz)y$ configuration which is strongly enhanced in $y(zz)y$ configuration, can be assigned to the polarization leakage of the A_{1g} c-axis polarized mode. In our measurement, we could not observe the E_g phonon modes. It may be as both (either) the intensity of the E_g modes is not enough to measure, and (or) the iron excess lowers the symmetry of the E_g modes, and the modes therefore are not detectable.

Fig. 3.18(b) shows the Raman spectra measured at room temperature on the parent $Fe_{1.02}Te$ (FT1) sample, together with the Se-doped $Fe_{1.00}Te_{0.78}Se_{0.22}$, $Fe_{0.99}Te_{0.69}Se_{0.31}$, $Fe_{0.98}Te_{0.66}Se_{0.34}$ and $Fe_{0.95}Te_{0.56}Se_{0.44}$ superconducting samples (FTS1, FTS2, FTS3 and FTS4, respectively) which have all iron stoichiometry as close to 1 as possible. Contrary to the observations of Xia et al. in Ref. (65) where the A_{1g} mode in parent $FeTe_{0.92}$ disappears in Se-doped $Fe_{1.03}Te_{0.7}Se_{0.3}$, the mode is clearly visible in all the investigated Se-doped compounds in the agreement with the results of Okazaki et al. (103). These two peaks are evidently much broader than the same phonon modes not only in other families of iron pnictides (106, 107, 108, 109), but also even in the same family (101). In particular, the Te A_{1g} mode linewidth in parent FT1 is $\sim$ 20

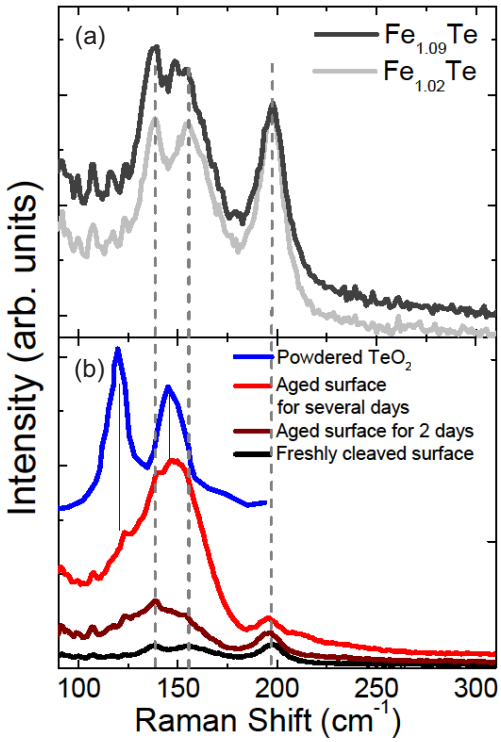

Figure 3.19: Raman spectra of $Fe_{1+y}Te$ at room temperature - (a) Room temperature Raman spectra of the parent $Fe_{1.02}Te$ and $Fe_{1.09}Te$ samples (vertically shifted for clarity). (b) Example of aging effect on the parent single crystals. The spectrum of powdered TeO_2 from Ref. (97) has been added for comparison.

cm^{-1} at room temperature. This is almost three times larger than the linewidth of the A_{1g} (As) mode in $BaFe_2As_2$.

3.5.3 Aging Effect

Fig. 3.19(b) shows Raman spectra obtained from a freshly cleaved surface and an aged surface at room temperature on the parent $Fe_{1.02}Te$ (FT1) sample. The strong aging effect already reported in Ref. (65) has also been observed in our measurement. In Ref. (65), the authors claimed that the formation of amorphous Te is the origin of a decomposition peak of $Fe_{1+y}Te_xSe_{1-x}$ based on the earlier reports (97, 98).

In Ref. (97) the authors mentioned *"The spectrum obtained from amorphous Te is shown in Fig. 2(d)."*, but in a *Note added in proof* they claimed that *"The spectrum of Fig. 2(d), attributed to an amorphous state of laser-premelted tellurium, is due to*

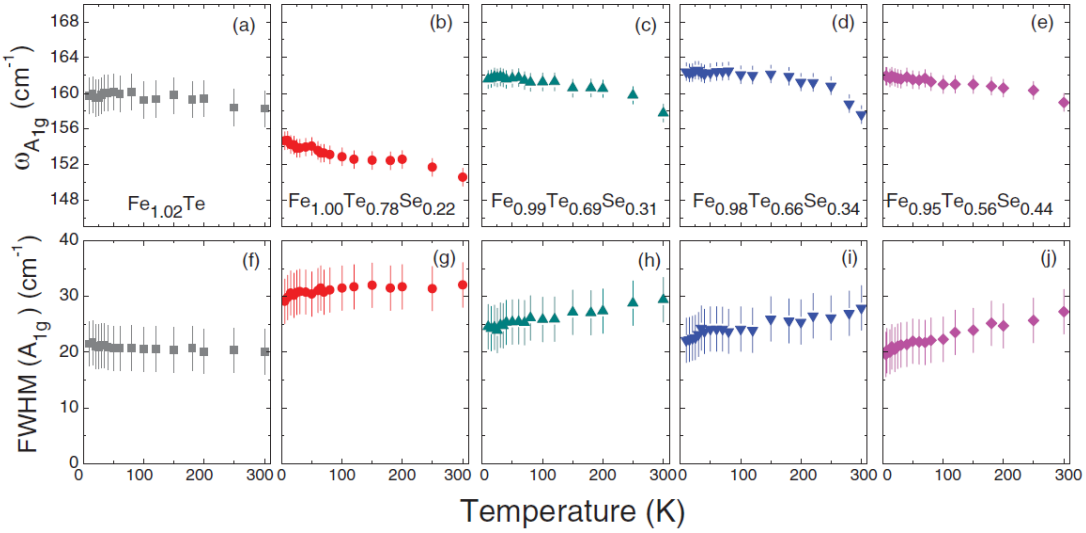

Figure 3.20: Temperature dependence of A_{1g} mode on $Fe_{1+y}Te_{1-x}Se_x$ - Upper panel: Temperature dependence of the A_{1g}(Te/Se) mode frequency of the (a) $Fe_{1.02}Te$ (FT1), (b) $Fe_{1.00}Te_{0.78}Se_{0.22}$ (FTS1), (c) $Fe_{0.99}Te_{0.69}Se_{0.31}$ (FTS2), (d) $Fe_{0.98}Te_{0.66}Se_{0.34}$ (FTS3), and (e) $Fe_{0.95}Te_{0.56}Se_{0.44}$ (FTS4). Lower panel: Temperature dependence of the A_{1g}(Te/Se) mode FWHM of the (f) FT1, (g) FTS1, (h) FTS2, (i) FTS3, and (j) FTS4.

an oxide created at high temperatures. The same characteristic spectrum is obtained a powdered sample of tetragonal TeO_2." and therefore the decomposition peak may originate from TeO_2 rather than amorphous Te. Hence, the Raman spectrum of powdered TeO_2 is added to our Fig. 3.19(b), and it is found that the peak position of TeO_2 is consistent with the position of the peak from our aged surface. The only differences are the relative intensities and widths of the two peaks of TeO_2 at 120 and 145 cm^{-1}. This may be caused by both (either) different texturing and strain of TeO_2 and (or) the presence of additional atom such as Fe in the decomposition product.

3.5.4 Influence of Se doping

- **A_{1g} mode**

Fig. 3.20 shows the temperature dependence of the A_{1g} mode of several $Fe_{1+y}Te_{1-x}Se_x$ samples. The frequency of the A_{1g} mode is weakly dependent on the Se contents. When Se of 31% is doped (FTS2), a small hardening ($\sim$ 2 cm^{-1}) is observed and it remains essentially constant up to 44% of Se-doped (FTS4) sample. Such small hardening seems

to be trivial, as in a first approximation, the phonon frequency is proportional to $M_r^{-1/2}$ (M_r is the reduced mass of the considered oscillator) and therefore the substitution of Te with lighter Se induces the mode hardening. The only noticeable exception is the $Fe_{1.00}Te_{0.78}Se_{0.22}$ (FTS1) sample where the A_{1g} mode is softer and broader than in any other Se-doped samples.

As shown in Fig. 3.18 and Fig. 3.19(a), an unexpected additional peak was observed at $\sim$ 136 cm^{-1} in A_{1g} symmetry in parent compounds. Interestingly, this peak disappears in the Se-rich samples (see Fig. 3.18(b)). However, its origin remains unclear, as (i) it is temperature independent and can therefore not be attributed to the lowering of the crystal symmetry-induced effect, and (ii) it is independent of the iron excess concentration and therefore iron excess-induced effect can be ruled out (see Fig. 3.19). In addition, (iii) the phonon peak of TeO_2 can also be ruled out as the aging-induced strong broad mode centered at 150 cm^{-1}, is clearly separate from the 136 cm^{-1} peak as shown in Fig. 3.19(b).

Furthermore, related with this mode, for 22% of Se doping level (FTS1), it seems the 136 cm^{-1} peak is still present, but not enough to resolve the mode and the A_{1g} mode, individually (see Fig. 3.18(b)). Therefore, the observed softening and broadening of the A_{1g} mode in FTS1 sample may originate from an overlapping of the A_{1g} mode with the 136 cm^{-1} peak.

Upon cooling down the system, a hardening of the A_{1g} mode is observed in all samples as expected from the lattice contraction, but no noticeable differences between the samples are observed. In particular, through the phase transitions (T_N and T_c), no phonon renormalizations have been observed. Within our error bars, the frequency of A_{1g} mode remains essentially unaffected by these transitions. A weak narrowing of the A_{1g} mode is observed for FTS2, FTS3 and FTS4 samples as expected from phonon anharmonicity (45, 46), while the broad linewidth of the mode in FT1 and FTS1 samples remains essentially temperature independent.

- **B_{1g} mode**

Fig. 3.21 shows a temperature dependence of B_{1g} mode on several $Fe_{1+y}Te_{1-x}Se_x$ samples. At 5 K, between 22% to 34% of Se-doped (FTS1 - FTS3) sample, the phonon frequency remains essentially constant, while a weak hardening ($\sim$ 2 cm^{-1}) is observed

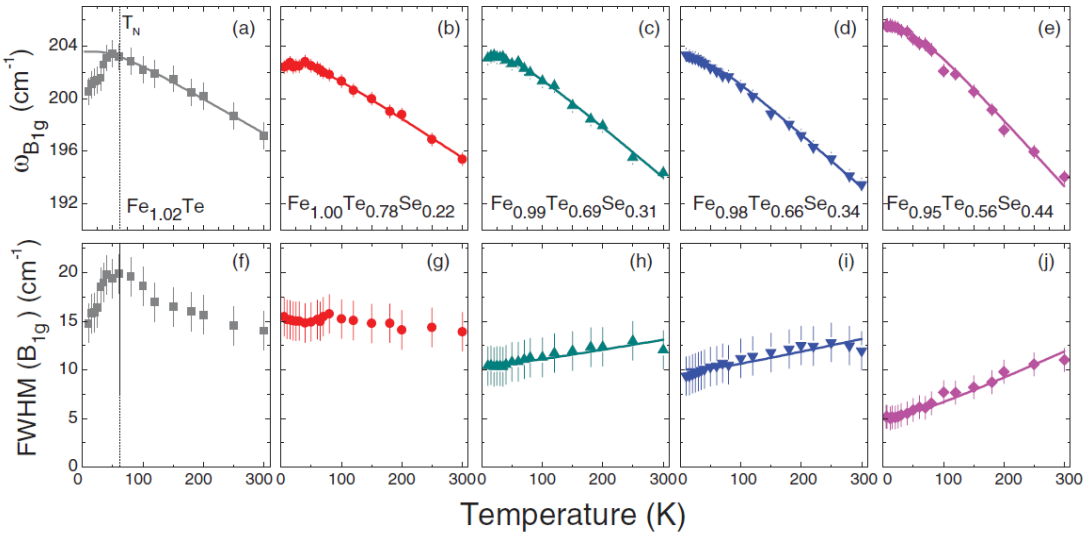

Figure 3.21: Temperature dependence of B_{1g} mode on $Fe_{1+y}Te_{1-x}Se_x$ - Upper panel: Temperature dependence of the B_{1g}(Fe) mode frequency of the (a) $Fe_{1.02}Te$ (FT1), (b) $Fe_{1.00}Te_{0.78}Se_{0.22}$ (FTS1), (c) $Fe_{0.99}Te_{0.69}Se_{0.31}$ (FTS2), (d) $Fe_{0.98}Te_{0.66}Se_{0.34}$ (FTS3), and (e) $Fe_{0.95}Te_{0.56}Se_{0.44}$ (FTS4). Lower panel: Temperature dependence of the B_{1g}(Fe) mode FWHM of the (f) FT1, (g) FTS1, (h) FTS2, (i) FTS3, and (j) FTS4.

in 44% of Se-doped (FTS4) sample. This effect may be caused by the significant Fe deficiency in the $Fe_{0.95}Te_{0.56}Se_{0.44}$ (FTS4) sample (It will be discussed in Sec. 3.6, 3.7.3).

Two interesting features, *i.e.*(i) phonon renormalization through the magnetic transition and (ii) unconventional temperature dependence of phonon linewidth, observed in Ref. (102), have also been observed in our measurement on the parent $Fe_{1.02}Te$ (FT1) sample. Usually in most of the materials, the phonon linewidth narrows with decreasing temperature, as phonon-phonon interactions are reduced with decreasing temperature

Name	Sample composition	ω_0 (cm^{-1})	Γ_0 (cm^{-1})	Γ (cm^{-1})
FTS2	$Fe_{0.99}Te_{0.69}Se_{0.31}$	203.9	9.9	0.78
FTS3	$Fe_{0.98}Te_{0.66}Se_{0.34}$	203.8	9.8	0.78
FTS4	$Fe_{0.95}Te_{0.56}Se_{0.44}$	205.6	3.44	2.1

Table 3.2: Fitting parameters for the temperature dependence of the B_{1g} phonon linewidth in $Fe_{0.99}Te_{0.69}Se_{0.31}$ (FTS2), $Fe_{0.98}Te_{0.66}Se_{0.34}$ (FTS3) and $Fe_{0.95}Te_{0.56}Se_{0.44}$ (FTS4) samples.

and the phonon half-width-at-half-maximum (HWHM) is proportional to τ^{-1} (τ is the phonon lifetime) and the phonon lifetime therefore increases (*i.e.* phonon linewidth narrows). However, in parent FT1 sample, phonon linewidth broadens with decreasing temperature (*i.e.* phonon lifetime decreases). This observation indicates the existence of an additional phonon decay channel in this system.

In parallel to this, an unusual evolution of temperature dependence of phonon linewidth upon Se doping is observed (see lower panels of Fig. 3.21). In the 22% Se-doped (FTS1) sample, the broadening of the linewidth with decreasing temperature is slightly suppressed, but still peculiar. However, from 31% of Se-doped (FTS2) sample, the unconventional broadening temperature dependence of the linewidth turns into a conventional narrowing behavior, but the FTS2 and FTS3 samples show only a weak narrowing of the phonon ($\sim$ 2.5 cm^{-1}) between room and base temperatures. In the almost optimal-doped $Fe_{0.95}Te_{0.56}Se_{0.44}$ (FTS4) sample, a conventional behavior is observed with a strong narrowing ($\sim$ 7 cm^{-1}).

The temperature dependence of both frequency and FWHM of the B_{1g} phonon for the FTS2, FTS3 and FTS4 samples can be well fitted by a symmetric anharmonic decay model (see Sec. 2.4.1) (45, 46), and the fitting parameters for these three samples are summarized in Table. 3.2. For the parent FT1 and Se-doped FTS1 samples, as the linewidth increases with decreasing temperature, the anharmonic phonon decay model can not be used to fit the experimental results.

3.5.5 Influence of iron excess

3.5.5.1 Parent compounds

- **A_{1g} mode**

Fig. 3.22(a)(c) show the temperature dependence of the A_{1g} mode in $Fe_{1.02}Te$ (FT1) and $Fe_{1.09}Te$ (FT2). The iron excess induces a small softening ($\sim$ 2 cm^{-1}) of the Te A_{1g} mode, while it does not induce any softening of the Fe B_{1g} mode. This may be became the iron excess locates on the Te plane, although it does not affect its already broad linewidth. No noticeable changes in the temperature dependence are observed. In particular, through the magnetic transition accompanying the structural transition, no phonon renormalization is observed.

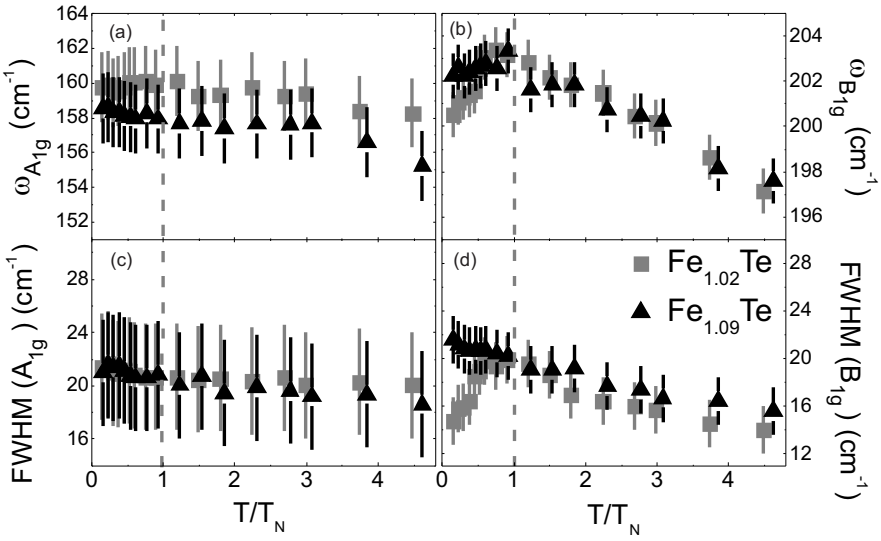

Figure 3.22: Temperature dependence of A_{1g} and B_{1g} mode on parent $Fe_{1+y}Te$ - (a) (b) Temperature dependence of the frequency of A_{1g} and B_{1g} modes, respectively, on parent $Fe_{1.02}Te$ (FT1) and $Fe_{1.09}Te$ (FT2) samples. (c) (d) Temperature dependence of the linewidth of A_{1g} and B_{1g} modes, respectively. Temperature has been normalized by the transition temperature and the dashed line indicates the transition temperature.

- **B_{1g} mode**

Fig. 3.22(b)(d) show the temperature dependence of the B_{1g} mode of the FT1 and FT2 samples. For a small amount of iron excess FT1 case, as shown in Fig. 3.21(a)(f), the B_{1g} mode softens and narrows through the magnetic transition. For a large amount of iron excess (FT2), a similar but weaker softening through the magnetic transition is observed, but interestingly magnetic transition-induced narrowing of the linewidth is clearly suppressed. Moreover the unusual broadening of the linewidth of the phonon mode with decreasing temperature is still observed, and it is therefore independent of the iron excess concentration, ruling out a disorder origin for this phenomena.

3.5.5.2 Se-substituted compounds

Fig. 3.23 shows the temperature dependence of the frequency and linewidth of the B_{1g} mode of Se-doped samples which contain different iron excess concentrations. In the case of $Fe_{0.95}Te_{0.56}Se_{0.44}$ (FTS4), as already discussed, conventional hardening and narrowing of the phonon with lowering temperature are observed. Such conventional

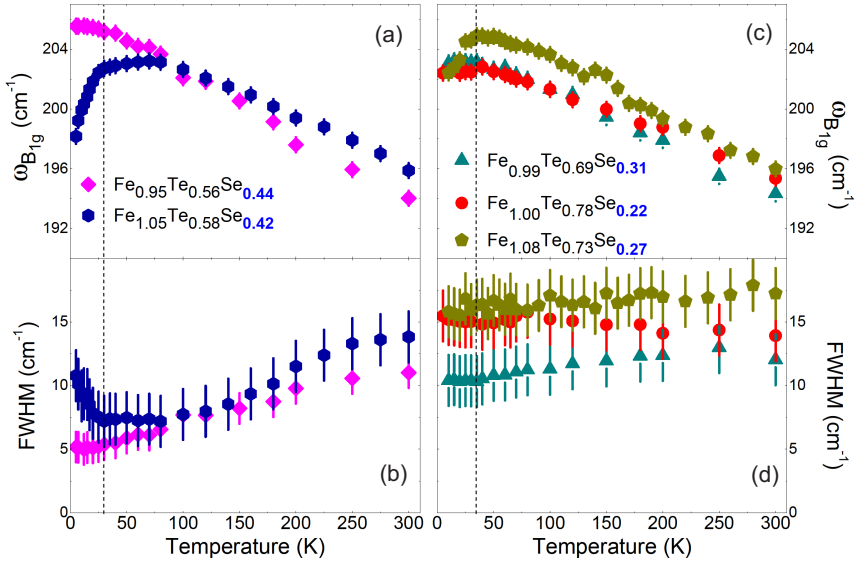

Figure 3.23: Influence of iron excess in B_{1g} mode on $Fe_{1+y}Te_{1-x}Se_x$ - (a) (b) Temperature dependence of the frequency and linewidth of B_{1g} mode, respectively, on $Fe_{0.95}Te_{0.56}Se_{0.44}$ (FTS4) and $Fe_{1.05}Te_{0.58}Se_{0.42}$ (FTS5) samples. (c) (d) Temperature dependence of the frequency and linewidth of B_{1g} mode, respectively on $Fe_{1.00}Te_{0.78}Se_{0.22}$ (FTS1), $Fe_{0.99}Te_{0.69}Se_{0.31}$ (FTS2) and $Fe_{1.08}Te_{0.73}Se_{0.27}$ (FTS6) samples. The dashed line indicates the temperature where the unexpected phonon renormalization occurs.

behavior is also observed in $Fe_{1.05}Te_{0.58}Se_{0.42}$ (FTS5) between room temperature and 35 K. However, suddenly the mode starts to broaden (~ 3 cm^{-1}) and soften (~ 5 cm^{-1}) at $\sim$ 35 K, although no phase transition occurs at this temperature. This remarkable effect is also observed in the $Fe_{1.08}Te_{0.73}Se_{0.27}$ (FTS6) sample at the same temperature of 35 K, but in the FTS6 sample the mode broadening is not observed. In the FTS6 sample, the B_{1g} mode is broader and the mode narrowing is weaker than those of the FTS2 sample, even though the FTS6 sample has a higher Se concentration than the FTS2 sample.

3.5.6 Summary of Experimental Results

Fig. 3.24 shows details of the fitting for selected representative samples for three groups ($Fe_{1.02}Te$ (FT1), $Fe_{0.95}Te_{0.56}Se_{0.44}$ (FTS4) and $Fe_{1.05}Te_{0.58}Se_{0.42}$ (FTS5)). It summarizes two of the main observations of this study: (i) the Se doping dependence of and (ii) the influence of iron excess on the Fe B_{1g} mode. In the parent FT1 sample, hardening

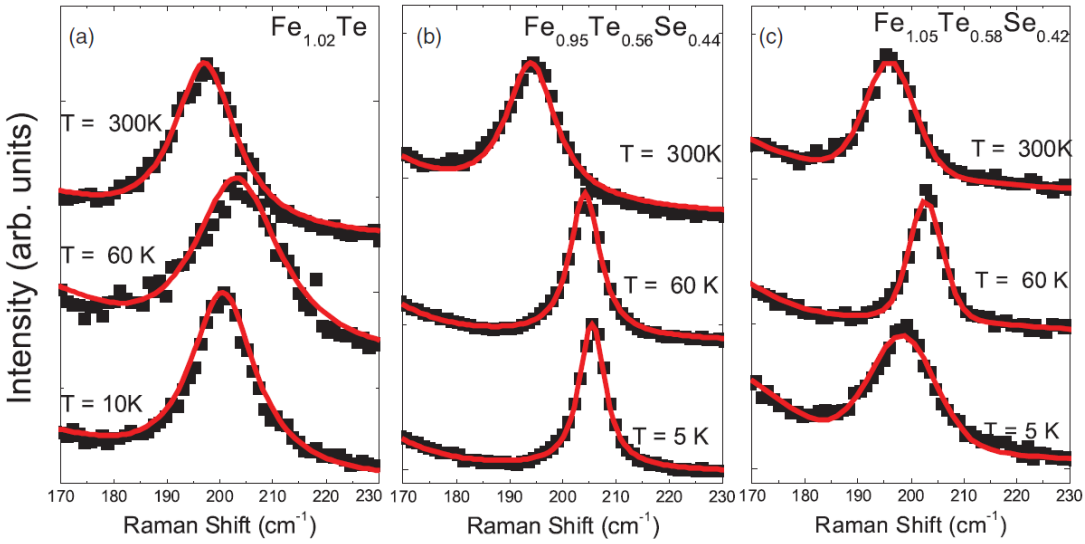

Figure 3.24: Raw Raman spectra with fitting of $Fe_{1+y}Te_{1-x}Se_x$ for several temperatures - (a) B_{1g} phonon of the $Fe_{1.02}Te$ sample for selected temperatures (Room temperature, $T \sim T_N$ and base temperature). Black squares are the raw data, red line is the fit following the procedure described in the text. Phonon intensity has been normalized and the spectra have been shifted vertically for clarity. (b) Same plot for the $Fe_{0.95}Te_{0.56}Se_{0.44}$ sample. (c) same plot for the $Fe_{1.05}Te_{0.58}Se_{0.42}$ sample.

and broadening of B_{1g} mode is observed when the temperature decreases down to T_N, and then softening and narrowing down to base temperature. In the Se-doped FTS4 sample with the highest Se and low iron concentrations, the spectra of the B_{1g} mode show a continuous hardening and narrowing down to 5 K. Finally, in the Se-doped FTS5 sample which contains almost the same Se concentration as the FTS4 sample but a higher iron concentration, the B_{1g} mode hardens and narrows down to 60 K, and then softens and broadens again down to 5 K, although there is no phase transition at this temperature. Such remarkable effects as a function of Se concentration and iron excess are clearly visible in the raw data.

Our main observations can be summarized as follow:

(i) In parent or low Se concentration samples, an unusual broadening linewidth of the B_{1g} phonon with decreasing temperature is observed. This gradually turns into a conventional narrowing linewidth with increasing Se substitution for Te.

(ii) In parent samples, softening and narrowing of the B_{1g} phonon through the magnetic transition are observed. These effects are suppressed in iron rich samples.

(iii) In Se substituted iron rich samples, strong softening and broadening of the B_{1g} mode at low temperature are observed.

3.6 LDA DFT Calculations

In order to gain further insights into the influence of magnetic order and iron excess concentration on the lattice dynamics in this system, non-spin polarized (nsp) and spin polarized (sp) density-functional theory (DFT) calculations have been performed by A. Subedi and L. Boeri for A_{1g} and B_{1g} modes. First, a stoichiometric FeTe system has been calculated using the frozen phonon approach with the experimental lattice parameters (a = 3.826 Å and c = 6.273 Å, with z_{Te}=0.28141) (60) and the results are summarized in Table. 3.3. In good agreement with previous calculations (72, 110), the magnetic moment of m = 2.2 μ_B for the double stripe order state is found. This is close to the experimentally observed value.

The influence of iron deficiency and excess on the B_{1g} mode is considered, and such non-stoichiometry is treated within the virtual crystal approximation (VCA). For the calculation, the experimental lattice parameters and Te height for several iron concentrations are taken from Ref. (60) and the phonon frequencies are calculated for nsp and sp configurations. The results we obtained are summarized in Table. 3.4, together with the self-consistent value of the magnetic moment at equilibrium. The influence of Se/Te concentrations on the A_{1g} mode can not be addressed, because the isovalent Se/Te substitution can not be treated within the VCA. In the calculation, the iron concentration is considered from 2% of deficiency to 6% of excess ($y = -0.02 \sim 0.06$), and it is found

Mode	ω_{nsp} (cm^{-1})	ω_{sp} (cm^{-1})	Expt. at 10 K (cm^{-1}) $Fe_{1.02}Te$ sample
A_{1g}	135	175	159.7
B_{1g}	200.9	197.5	200.5

Table 3.3: A_{1g} and B_{1g} frequencies of FeTe, from the non-spin polarized (nsp) and spin polarized (sp) DFT calculations.

	ω_{nsp} (cm^{-1})	ω_{sp} (cm^{-1})	m (μ_B)
$Fe_{0.98}Te$	216.76	207.36	2.34
$Fe_{0.99}Te$	207.21	199.92	2.28
FeTe	200.94	197.54	2.20
$Fe_{1.02}Te$	191.30	192.40	2.06
$Fe_{1.06}Te$	173.00	182.00	1.60

Table 3.4: B_{1g} frequencies of $Fe_{1+y}Te$, from the non-spin polarized (nsp) and spin polarized (sp) DFT calculations. m is the value of the self-consistent double-stripe moment at zero displacement, in μ_B.

that the values of the calculated frequencies and magnetic moments are extremely sensitive to the non-stoichiometric iron concentration. The calculated magnetic moments and frequencies decrease monotonically upon increasing the iron concentration with rates of ~ 523 cm^{-1}/y and ~ 292 cm^{-1}/y for nsp and sp calculations, respectively.

3.7 Discussion

3.7.1 Comparison with Other Families

- **Phonon calculation**

In the 122 and 1111 systems, it has been already shown that the calculated phonon frequencies with considering the magnetic order are much closer to the experimental phonon frequencies than those obtained without considering the magnetic order, even in the non-magnetic state (111, 112, 113, 114). This is also the case of our work, as the frequency resulting from the sp calculation is much closer to the experimental observation than the frequency from the nsp calculation. In particular, for the iron non-stoichiometry case considered within the VCA, the sp calculation clearly provides better agreement than the nsp calculation (see Table. 3.4).

- **Phonon renormalization through T_N**

In previous phonon studies of 122 parent compounds, phonon renormalizations (hardening and narrowing) have been reported at the structural transition accompanying the SDW transition. In parent $BaFe_2As_2$, no softening is observed for the B_{1g}

mode through the structural transition, while a sudden downward frequency jump is observed in the A_{1g} mode through T_N (106, 115). In parent $CaFe_2As_2$, a sudden frequency jump is observed for the B_{1g} mode through T_N (107). In the latter case, this effect can be explained by a sudden collapse of the unit cell along the c-axis through the transition (116); but such c-axis collapse does not take place in $BaFe_2As_2$ (117).

In parent $Fe_{1.02}Te$ (FT1), a clear smooth softening of the B_{1g} phonon through the coupled structural-magnetic transition has been observed in our measurement. In the case of the parent $Fe_{1+y}Te$, it has been observed that the c-axis lattice parameter suddenly expands through the transition (68). This expansion of c-axis certainly favors the observed softening, although in this case one would expect an abrupt jumping down of the phonon frequency rather than the observed smooth softening between T_N and 10K .

The linewidth narrowing of the B_{1g} mode through the transition in $Fe_{1+y}Te$ is similar to that in 122 system. As the phonon linewidth is inversely proportional to its lifetime, the renormalization of the mode through the transition reflects the changes of the coupling strength between phonon and some decay channels. For the 122 system, due to the opening of the SDW gap (118, 119), a significant reduction of the electronic density-of-states at the Fermi level occurs, and it leads to a decrease of electron-phonon coupling which rationally accounts for the observed narrowing of the phonon linewidth (106). Such a SDW gap opening has not been reported yet in the 11 system (63, 66), but recently a SDW gap has been observed in ARPES experiments (120), and it is therefore very likely responsible for the narrowing of the B_{1g} mode in the $Fe_{1.02}Te$ (FT1) sample.

- **Absence of superconductivity-induced effects**

So far, most of the Raman studies did not observe any superconductivity-induced phonon renormalization through T_c in both A_{1g} and B_{1g} modes (106, 109, 121), except for $Sr_{0.85}K_{0.12}Fe_2As_2$ (107) and $Pr_xCa_{1-x}Fe_2As_2$ (108) where a small hardening of the B_{1g} phonon through T_c occurs. The absence of superconductivity-induced effect is expected, because the superconducting gap amplitude is much smaller than the phonon frequencies, and therefore the phonon frequencies remains essentially unaffected by the opening of superconducting gap. This is also the case for $Fe_{1+y}Te_{1-x}Se_x$, as the phonon frequency is much larger than the reported superconducting gap energies in various

experiments: $2\Delta \sim 2$ meV (17 cm^{-1}) (87), 3.4 meV (27.4 cm^{-1}) (86) or 4.6 meV (37 cm^{-1}) (88) from STM, $2\Delta \sim 3$ meV (24 cm^{-1}) from NMR (89), and $2\Delta \sim 6$ meV (48 cm^{-1}) from specific heat (67).

3.7.2 Se-substituted Systems

In the Se-doped $Fe_{1+y}Te_{1-x}Se_x$ system, the c-axis lattice parameter decreases upon Se doping (15, 61, 68), and it is therefore responsible for the observed weak enhancement of the B_{1g} phonon frequency at the lowest temperature (see Figs. 3.21). The room temperature linewidth of B_{1g} mode is weakly dependent on the Se concentration (~ 2 cm^{-1}), while at the lowest temperature the difference is clearly strong (~ 5 cm^{-1}). This is unexpected, because usually the doping process that introduces impurities into the system, and one would therefore expect the Se-substitution leads to a broadening of the phonon linewidth rather than a narrowing. In addition, the normal state temperature dependence of the phonon linewidth for several different Se doping levels is even more puzzling as discussed in Sec. 3.5.4.

In a conventional anharmonic decay model, the residual linewidth Γ_0 which is temperature independent, reflects the strength of electron-phonon coupling and/or disorder effects. For the $Fe_{0.99}Te_{0.69}Se_{0.31}$ (FTS2), $Fe_{0.98}Te_{0.66}Se_{0.34}$ (FTS3) and $Fe_{0.95}Te_{0.56}Se_{0.44}$ (FTS4) samples (see Table. 3.2), the Γ_0 is 3.4 cm^{-1}, and this value is comparable with the prefecture of temperature-dependent linewidth Γ (2.1 cm^{-1}) (see Eq. 2.38), while in the FTS3 and FTS2 samples, Γ_0 is ~ 10 cm$^{-1} \gg \Gamma$. This doping-induced linewidth evolution is unusual and indicates that the contribution of the conventional anharmonicity to the B_{1g} phonon lifetime is not dominant. Hence, at least one additional decay channel for this phonon, of which the contribution strongly depends on the Se concentration should be taken into account. For that two possible origins, *i.e.* (i) conventional electron-phonon coupling and (ii) spin-phonon coupling, can be considered. In the first scenario (electron-phonon coupling), the increasing relative weight of the temperature-independent residual linewidth Γ_0 with decreasing Se content can be related to the increase of the electronic density-of-states at the Fermi level $N(E_F)$ (72), which naturally leads to a decrease of the phonon lifetime through their coupling to electrons ($\Gamma_0 \propto N(E_F)$). However this may not be sufficient to account for the observed unusual temperature dependence of the B_{1g} phonon linewidth in parent $Fe_{1.02}Te$ (FT1) and $Fe_{1.00}Te_{0.78}Se_{0.22}$ (FTS1) samples, as the electron-phonon coupling is in principle

temperature-independent. Thus, for the temperature dependent linewidth of the B_{1g} phonon spin-phonon coupling may be a possible additional decay channel, because the weight of magnetic excitations directly depends on the temperature (further it also depends on the Se concentrations) (64, 95).

3.7.3 Influence of Iron excess

- **Comparison of experimental data with LDA DFT calculation**

In our LDA DFT phonon calculations (see Sec. 3.6), a softening of the B_{1g} phonon frequencies with increasing of iron concentration is found with softening rates of 523 and 292 cm^{-1}/y for nsp and sp calculations, respectively. Experimentally, at low temperature, when the iron concentration increases from $Fe_{1.02}Te$ (FT1) to $Fe_{1.09}Te$ (FT2), a small hardening ($\sim$ 2 cm^{-1}) is observed, while in Se-substituted samples a softening rate of $\sim$ 70 cm^{-1}/y between $Fe_{0.95}Te_{0.56}Se_{0.44}$ (FTS4) and $Fe_{1.05}Te_{0.58}Se_{0.42}$ (FTS5) is observed. Furthermore, between $Fe_{0.98}Te_{0.66}Se_{0.34}$ (FTS3) and FTS4, a softening rate of $\sim$ 66 cm^{-1}/y is observed, although in this case the Se concentrations are slightly different.

In any case, the experimentally observed iron non-stoichiometry-induced softening rates are much weaker than those theoretically calculated, even considering the sp calculation where the softening rate is the smallest. An accurate comparison of experimentally observed value to the calculated one is very difficult, however, because of the presence of iron excess which complicates the system. In principle, within the VCA treatment, the excess or deficient charges are considered to be located simply in the same iron site, while experimentally excess iron atoms are located in the Te plane. In addition, the effective iron magnetic moment increases by the formation of local moments on interstitial iron atoms. Such a complicated situation can not be taken into account in the VCA, and (as a result), the iron excess-induced renormalization of the frequency and linewidth in the B_{1g} mode (see Fig. 3.23) can not be reproduced in LDA DFT calculations.

- **Iron excess-induced magnetic fluctuation**

As discussed in Sec. 3.5.5.1, the SDW transition-induced phonon renormalization in $Fe_{1.02}Te$ (FT1) sample is suppressed in the iron rich $Fe_{1.09}Te$ (FT2) sample. A

small softening but no narrowing of the linewidth has been observed (see Fig. 3.22). Furthermore, in the Se-substituted iron rich samples, an unexpected phonon softening and broadening are present below $\sim$ 35 K (well above T_c) which are absent in iron deficient sample (see Fig. 3.23). So far, no phase transition has been reported at this temperature range ($\sim$ 35 K) in Se-substituted sample, but one interesting feature has been reported at this temperature: short range magnetic fluctuations (64). In the parent compound $Fe_{1+y}Te$, a low energy spin excitation is present with a gap in the SDW state, but upon increasing the iron excess concentration, the low energy spin gap has been filled up by the low energy spin fluctuations (71).

Thus, in both parent and Se-doped cases, one major effect of iron excess is introducing low energy magnetic fluctuations into the system in a temperature range where the B_{1g} phonon broadens. This reinforces the point we made at the end of Sec. 3.7.2, indicating that the additional damping for the B_{1g} mode may actually originate from its coupling to the magnetic excitations.

3.8 Conclusions

A systematic study of the lattice dynamics in the $Fe_{1+y}Te_{1-x}Se_x$ has been carried out for various iron excess y and Se concentrations x, especially focussing on the c-axis polarized Fe B_{1g} mode. The observed phonon frequencies are in good agreement with the frequencies obtained from a first-principles calculation including the effect of magnetic order, similar to that in iron pnictides. In parent $Fe_{1+y}Te$, unlike other families of iron pnictides such as 122 and 111 systems, the unconventional linewidth broadening of the mode with decreasing temperature, which gradually turns into conventional linewidth narrowing has been observed, and a clear signature of the opening of the SDW gap is observed. In particular, the influence of the iron excess to the B_{1g} phonon is addressed, and it leads us to infer a peculiar coupling between the B_{1g} phonon and iron excess-induced magnetic fluctuations in the $Fe_{1+y}Te_{1-x}Se_x$ compound.

4

LiFeAs

The discovery of superconductivity in LiFeAs (111-type) has generated several debates in the iron-based superconductors due to its unique features. In general, all iron-based superconductors share similar properties: (i) a magnetic transition accompanying a structural transition in stoichiometric parent compounds, (ii) a strongly nested Fermi surface that induces a SDW instability in the parent compounds, and (iii) the appearance of superconductivity upon chemical doping or external pressure. In LiFeAs, neither structural nor magnetic transitions are reported, and superconductivity with T_c of 18 K is present at ambient pressure without any doping, even though LiFeAs has very similar crystal and electronic structures to those of other families of iron-based superconductors. Moreover, the origin of superconductivity in LiFeAs is controversial. The presence of weak local moments and normal-state AFM fluctuations with a prediction of weak electron-phonon coupling seems to support an unconventional pairing mechanism, as in other FeAs compounds. On the other hand, a superconducting gap ratio ($2\Delta \sim 4\ k_B T_c$) measured by several techniques is closer to the BCS limit (weak electron-electron coupling), and ARPES measurements have indicated a strong electron-phonon coupling, possibly enhanced by the magnetic fluctuations. These data seems to rather suggest a conventional phonon-mediated pairing in this compound.

In this chapter, I will report the first lattice dynamics study on LiFeAs using Raman scattering spectroscopy and investigate the strength of the electron-phonon coupling which has caused a controversy on the origin of superconductivity in this compound. In Sec. 4.1, I will discuss general properties and issues in LiFeAs, and in particular, in Sec. 4.2, I will point out a report of strong electron-phonon coupling which motivates

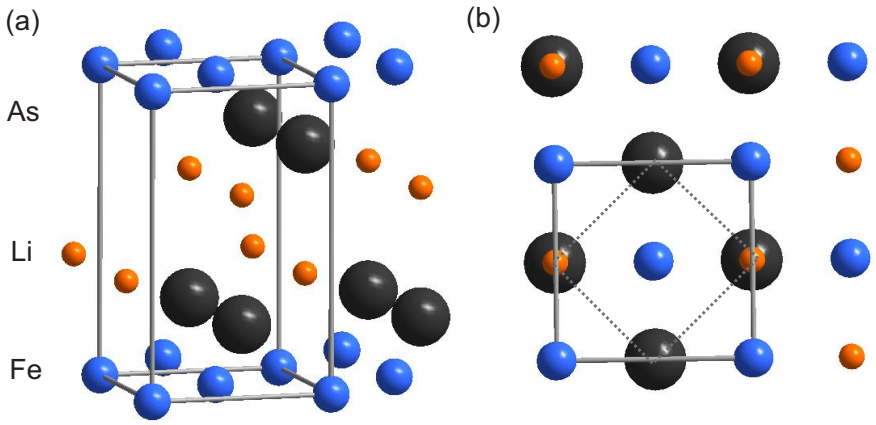

Figure 4.1: Crystal structure of LiFeAs - Tetragonal Cu_2Sb-type (or anti-PbO-type) structure (space group P4/nmm (D_{4h}^7)). The orange, blue, black atoms and gray line represent the Li, Fe, As atoms and the tetragonal unit cell, respectively. Two lithium, two iron and two arsenic atoms are present in the tetragonal unit cell. (a) 3D view. (b) Top view. The gray dashed line represents the primitive unit cell containing one iron and one arsenic atoms.

the present work. In Sec. 4.3, I will describe the samples which were used in this work. In Sec. 4.4, 4.5, I will discuss our experimental observations, and then finally, in Sec. 4.6, I will state some conclusions.

4.1 Properties and Issues in LiFeAs

4.1.1 Crystal Structure

LiFeAs was first synthesized in 1968 by Juza et al. (122) without attracting much attention. Since the discovery of superconductivity in iron-based compounds (7), LiFeAs has been resynthesized and superconductivity has been found by several groups (12, 123, 124). The lattice symmetry of LiFeAs is described by the Cu_2Sb-type (or anti-PbO-type) tetragonal structure (space group P4/nmm (D_{4h}^7)) with Li, Fe and As atoms located at 2c, 2b, and 2c Wyckoff positions, respectively. Lattice parameters are a = 3.777 Å and c = 6.356 Å (125). The structure is composed of stacks of FeAs layers which are separated by double layers of Li ions as shown in Fig. 4.1. As a consequence of the small size of the Li ion, the edge-sharing $FeAs_4$ tetrahedra are compressed in the basal plane, and the Fe-Fe distance (2.6809 Å) (12) is significantly smaller in LiFeAs

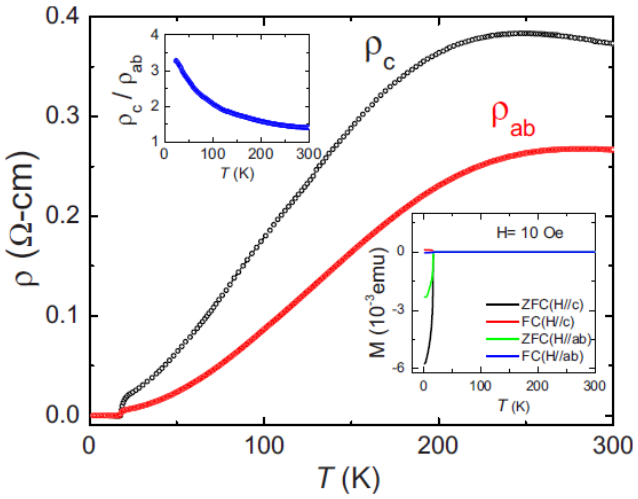

Figure 4.2: Resistivity of LiFeAs - The in-plane and out-of-plane resistivity of LiFeAs from Ref. (128). The superconducting transition occurs at $\sim$ 18 K. The left inset shows the electrical anisotropy and the right inset shows the magnetic susceptibility.

than in the other Fe-based compounds such as LaFeAsO (2.8528 Å) (126) or $BaFe_2As_2$ (2.8021 Å) (127).

4.1.2 Electronic and Magnetic Structure

LiFeAs is a metal as shown by the resistivity data displayed in Fig. 4.2 (128). The initial LDA calculations predicted a Fermi surface topology similar to that of other families of iron pnictides (hole pockets at the Γ point and electron pockets at the M point) as shown in Fig. 4.3 (129), and experimentally, it has been confirmed by several ARPES measurements (see Fig. 4.4) (130, 131, 132) and quantum oscillations measurement (133).

- **Electronic structure**

First-principles calculations have been performed for nonmagnetic, ferromagnetic (FM) and antiferromagnetic (AFM) states to get insight into the ground state of LiFeAs. In particular, for the AFM state, two different magnetic vectors (A′ type and C′ type) are considered (see Fig. 4.5). Similar to other families of iron pnictides, it has been found that a SDW instability is present (129), and that the C′ type (striped AFM state) is most stable state (134, 136) with weak magnetic moments (0.7 μ_B/iron by

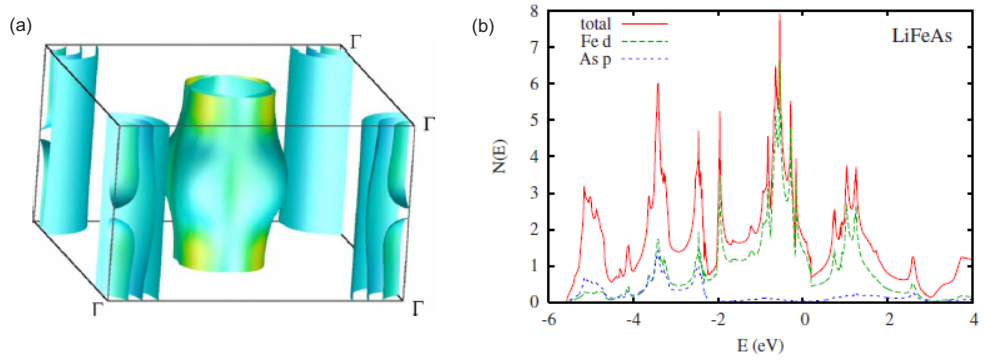

Figure 4.3: Electronic structure of LiFeAs - Electronic structure of LiFeAs from Ref. (129). (a) LDA Fermi surface of LiFeAs. The corners are Γ points. (b) Electronic density-of-state (DOS).

linearized augmented plane waves (LAPW) (129), 1.5 - 1.6 μ_B/iron by the generalized gradient approximation (GGA) and 0.1 - 0.6 μ_B/iron by the local spin-density approximations (LSDA) (134, 136)). However, contrary to the first-principles calculations, one important feature captured in ARPES measurements is the absence of Fermi surface nesting between hole and electron pockets which is the driving force of

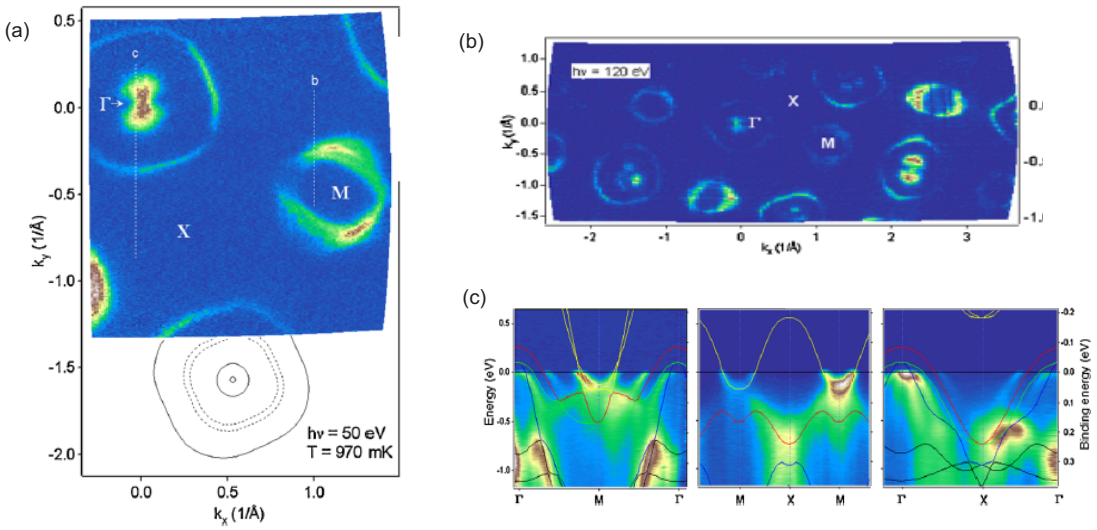

Figure 4.4: Fermi surface topology of LiFeAs - (a) (b) Fermi surface map of LiFeAs at $\sim$ 1 K from Ref. (130). Hole pockets at the Γ point and electron pockets at the M point. (c) Comparison with the band structure calculations.

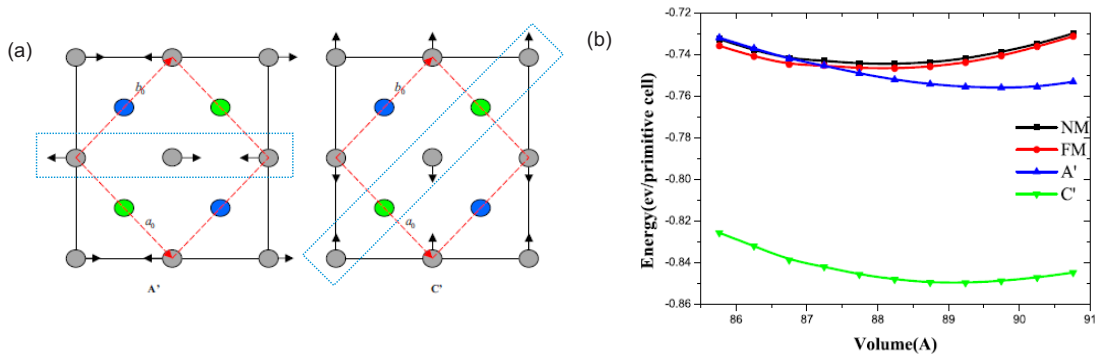

Figure 4.5: Ground sate of LiFeAs - (a) Schematic picture for two different magnetic states from Ref. (134). The gray, blue, green atoms and dashed red line represent the Fe, As (below Fe plane), As (above Fe plane) atoms and the tetragonal unit cell, respectively. A′ and C′ denote AFM along (π,0) and (π,π), respectively. The dashed blue line indicates the magnetic vector. (b) Equation of state for nonmagnetic, FM, A′ type and C′ type from GGA calculations.

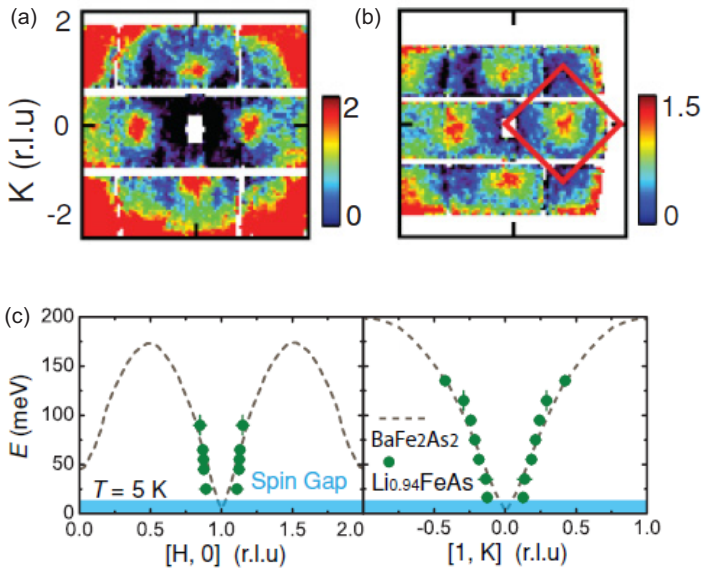

Figure 4.6: Magnetic excitation in LiFeAs - (a) (b) Magnetic excitations in LiFeAs at 5 K for energy transfers 25 meV and 45 meV, respectively from Ref. (135). The magnetic excitations are centered at the M point. The red box in (b) indicates the Brillouin zone. (c) (d) Magnetic excitations along [H, 0] and [0, K]. The dashed line shows spin wave dispersion for $BaFe_2As_2$ at 5 K.

the SDW instability (130). Moreover, no static magnetic order is found in SQUID measurements (12, 123).

- **Magnetic structure**

Nevertheless, in LiFeAs, experimentally $\sim 0.9\ \mu_B$/iron has been measured by x-ray emission spectroscopy (74), and NMR measurements indicate the presence of normal state AFM fluctuations (137, 138). In particular, recently, in non-superconducting lithium deficient $Li_{1-x}FeAs$ (x $\sim$ 0.06) where no static AFM order is present, low energy magnetic excitations with a spin gap have been observed by inelastic neutron scattering measurements as shown in Fig. 4.6 (135). The low energy magnetic excitations are centered at the M point (π,π), with a large spin gap of 13 meV similar to $BaFe_2As_2$ (139). With increasing energy, the magnetic excitation splits, and high energy magnetic excitations are centered at (π,0). The observed magnetic features suggest the possibility of a similar nature of superconductivity in LiFeAs as in other iron-based superconductors.

4.1.3 Superconducting State

- **Chemical doping**

The usual first step for achieving superconductivity in iron-based superconductors is to introduce additional charge carriers in the system. However, the parent LiFeAs shows superconductivity with a $T_c \sim 18$ K at ambient pressure, without any chemical doping (see Fig. 4.2), similar to iron chalcogenide FeSe (14). For this reason, the influence of iron excess has been considered by substituting 4% of Fe to the Li site ($Li_{1-y}Fe_{1+y}As$), and it was observed that the introduced iron excess rapidly destroys superconductivity (see Fig. 4.7(a)). Furthermore, the influence of additional charge carriers has been studied by substituting Co or Ni to the Fe site ($LiFe_{1-x}M_xAs$, (M = Co, Ni)), and it was found that superconductivity is also suppressed with increasing doping (see Fig. 4.7(b)) (125).

- **High pressure**

In order to get further insights into superconductivity, pressure studies have been performed. In LiFeAs, upon applying pressure, T_c gradually decreases and disappears

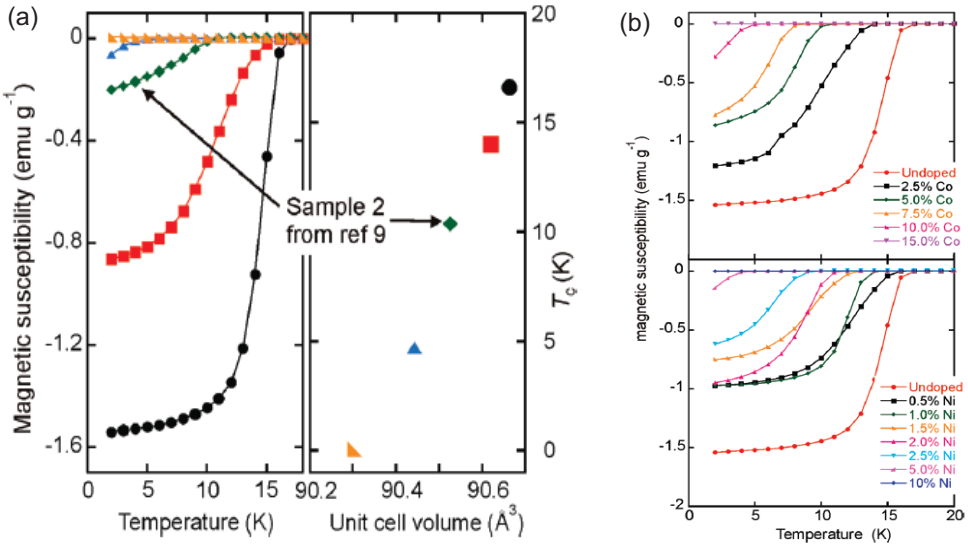

Figure 4.7: Superconductivity in LiFeAs upon chemical doping - (a) ZFC magnetic susceptibility (left) and T_c for $Li_{1-y}Fe_{1+y}As$ samples from Ref. (125). T_c decreases with increasing iron doping. (b) ZFC magnetic susceptibilities for $LiFe_{1-x}Co_xAs$ (up) and $LiFe_{1-x}Ni_xAs$ (down) samples from Ref. (125). Upon doping, superconductivity is suppressed.

at $\sim$ 8.4 GPa as shown in Fig. 4.8 (140, 141). Taken together with the chemical doping effect, it is found the mechanism of achieving superconductivity in LiFeAs is essentially

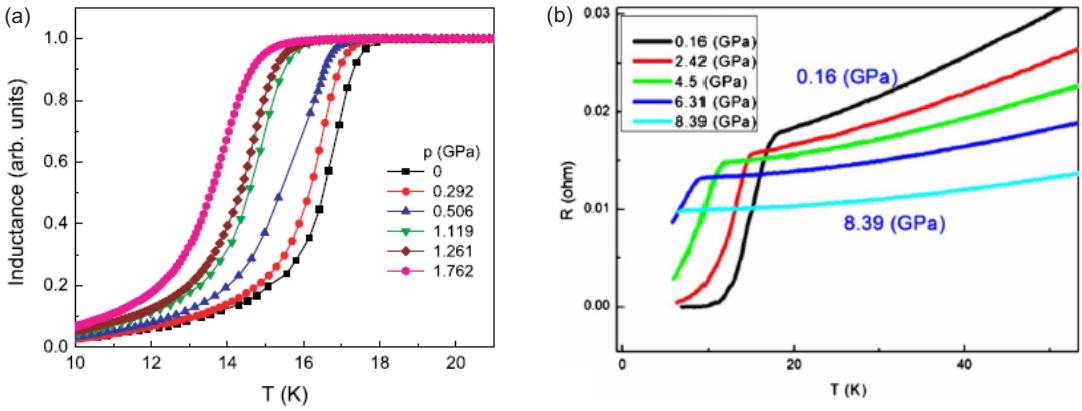

Figure 4.8: Superconductivity in LiFeAs under high pressure - (a) Mutual inductance of LiFeAs under high pressure from Ref. (140). (b) Resistivity of LiFeAs under high pressure from Ref. (141). T_c decreases with applying pressure.

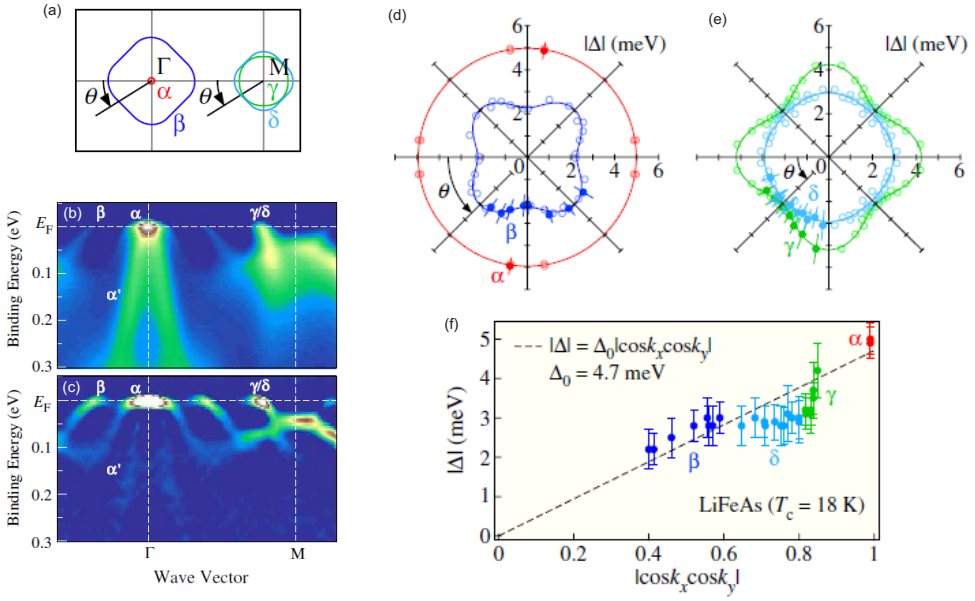

Figure 4.9: Superconducting gap in LiFeAs - (a) Schematic Fermi surface and the definition of angle θ from Ref. (132). (b) (c) Intensity and its second-derivative along the Γ - M, respectively. (d) (e) Superconducting gap size for the α, β and the γ, δ Fermi surfaces, respectively. Filled circles are the raw data, and opened circles are the folded data in fourfold symmetry. (f) Superconducting gap size as a function of $|\cos k_x \cos k_y|$

different from that in other families of iron-based superconductors, and in particular, LiFeAs can be considered as almost optimally doped compound by itself, which is a unique feature among all other families of iron-based superconductors.

- **Superconducting gap**

Several techniques indicate different superconducting gaps: (i) An isotropic single gap: London penetration depth and small-angle neutron scattering ($\Delta \sim 3$ meV) (142), (ii) two-gaps on hole and electron pockets, respectively: ARPES ($\Delta \sim 1.5$ meV and $\Delta \sim 3$ meV) (130), specific heat ($\Delta \sim 1.2$ meV and $\Delta \sim 2.6$ meV) (143), London penetration depth ($\Delta \sim 1.5$ meV and $\Delta \sim 3$ meV) (144), ($\Delta \sim 1.6$ meV and $\Delta \sim 3.1$ meV) (145), nuclear magnetic resonance (NMR) ($\Delta \sim 1.9$ meV and $\Delta \sim 4.4$ meV) (146), and (iii) anisotropic multi-gaps on hole and electron pockets, respectively: ARPES ($\Delta \sim 5.0$ meV, $\Delta \sim 2.5$ meV and $\Delta \sim 4.2$ meV, $\Delta \sim 2.8$ meV)) (132).

So far, the superconducting gap symmetry in LiFeAs is still controversial, even though most of the measurements suggest a nodeless $s_{\pm}$-wave superconducting gap

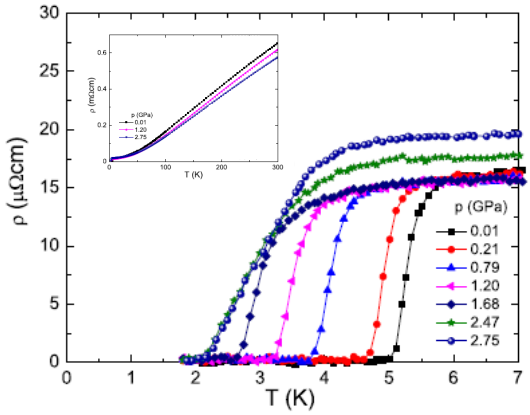

Figure 4.10: Superconductivity in LiFeP - Resistivity of LiFeP under pressure from Ref. (150).

symmetry ruling out a nodal d-wave gap symmetry. In particular, recently measured multi-gaps on hole and electron pockets by ARPES measurement can also be described by $s_{\pm}$-wave symmetry as shown in Fig. 4.9, although they are anisotropic (132, 147). However, the observed gap anisotropy provides the possibility of different pairing symmetry, for instance a mixture pairing between $s_{\pm}$-wave and another symmetry or other symmetries. In addition, the very recently studied quasi particle interference pattern using STM (148) suggests the p-wave gap symmetry, which also has been theoretically predicted in Ref. (149).

4.1.4 Similar Compounds

Superconductivity with $T_c \sim 6K$ (at ambient pressure) has been also found in LiFeP, which is isostructural and isoelectronic to LiFeAs (150, 151). In LiFeP, T_c gradually decreases with applying pressure as shown in Fig. 4.10, similar to LiFeAs.

4.2 Strength of Electron-Phonon Coupling

The initial DFT calculations for electron-phonon coupling strength without considering spin-polarization have found $\lambda = 0.26$ - 0.29, where λ is the electron-phonon coupling strength, and suggested that the electron-phonon coupling is too weak to account such high T_c in LiFeAs, like other families of iron-based superconductors (3, 4). However,

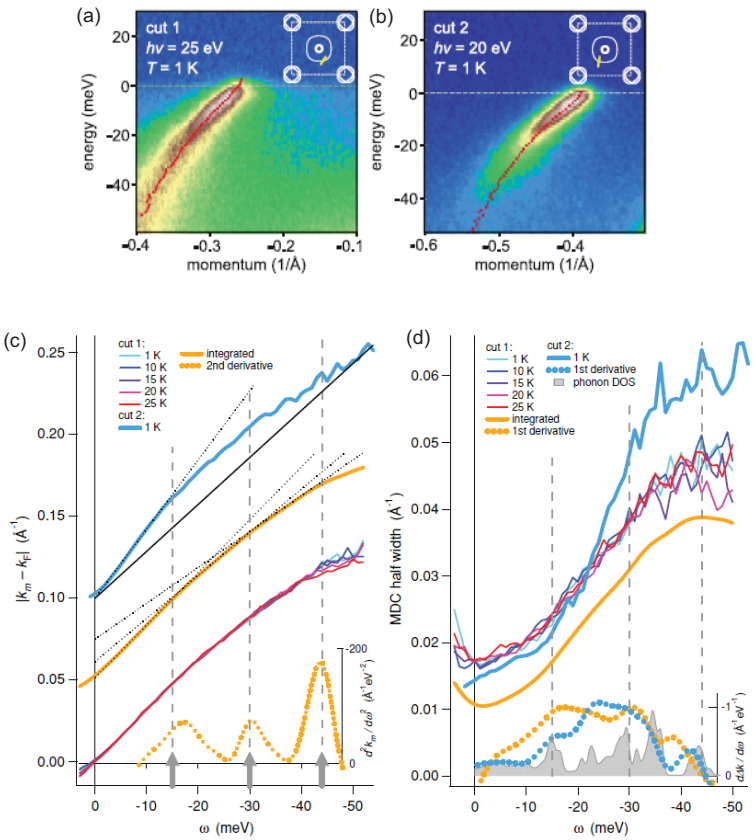

Figure 4.11: Strong electron-phonon coupling - (a) (b) Different cuts of hole pocket and (c) (d) the positions and linewidth of MDC as a function of energy ω for different cuts, respectively from Ref. (131). The gray vertical dashed lines indicate the energy of the optical phonon modes.

it has been found that such weak electron-phonon coupling strength can possibly be enhanced in the spin-polarized state (4, 152). In addition, recent ARPES measurements have suggested that the coupling between electrons and phonons could be stronger ($\lambda = 1.38$) than initially emphasized, as kinks in the momentum distribution curves (MDC) have been observed as shown in Fig. 4.11, where the positions and linewidth of the MDC for different cuts are present (131). Kinks in the electronic dispersion usually imply the interaction of the electron with a boson residing at the kink energies. In Fig. 4.11(c), the positions of the MDC maxima have been integrated for several temperatures, and three kinks have been observed. The energies of the observed kinks correspond to the energies of the optical phonon modes: 15 meV (121 cm^{-1}), 30 meV (240 cm^{-1}) and

44 meV (356 cm^{-1}) from Ref. (3). Furthermore, similar kinks also have been observed in the linewidth of the MDC at the same phonon energies (see Fig. 4.11(d)), which implies the possibility of electron-phonon coupling in this compound.

This experimental observation rather suggests a conventional electron-phonon driven pairing than an unconventional pairing, and requires the study of the strength of the electron-phonon coupling. So far, no studies of lattice dynamics that would allow a direct determination of the strength of the electron-phonon coupling, have been reported on LiFeAs. This situation motivates the present work.

4.3 Sample Characterizations

Single crystals of LiFeAs with $T_c \sim 18$ K were grown by Song et al. using a sealed tungsten crucible and Bridgman method as described in Ref. (128). Typical superconducting transition temperatures T_c of 18 K were measured by a superconducting quantum interference device (SQUID) as shown in Fig. 4.2. Sample preparations for Raman measurement were carefully carried out as LiFeAs crystals are extremely air sensitive. In particular, they were cleaved and mounted on the cold finger of a helium-flow cryostat in a glove box under Ar atmosphere.

4.4 Experimental Results

4.4.1 Experimental Conditions

All Raman light scattering experiments were performed on freshly cleaved surfaces, and the samples were mounted in a helium-flow cryostat. Spectra were taken in backscattering geometry through a JobinYvon LabRam 1800 single grating spectrometer, and a linearly polarized He^+/Ne^+ mixed gas laser with $\lambda = 632.817$ nm has been used for excitation. The power of the incident beam was kept less than 1 mW with a ~ 5 μm diameter spot on the sample surface.

4.4.2 Mode Assignment

As the lattice symmetry of stoichiometric LiFeAs is in the space group $P4/nmm$ (D_{4h}^7), with Li, Fe and As atoms at 2c, 2b, and 2c Wyckoff positions, respectively, one would expect 18 zone-center phonon modes ($\Gamma_{LiFeAs} = 2A_{1g} + 1B_{1g} + 3A_{2u} + 3E_u + 3E_g$)

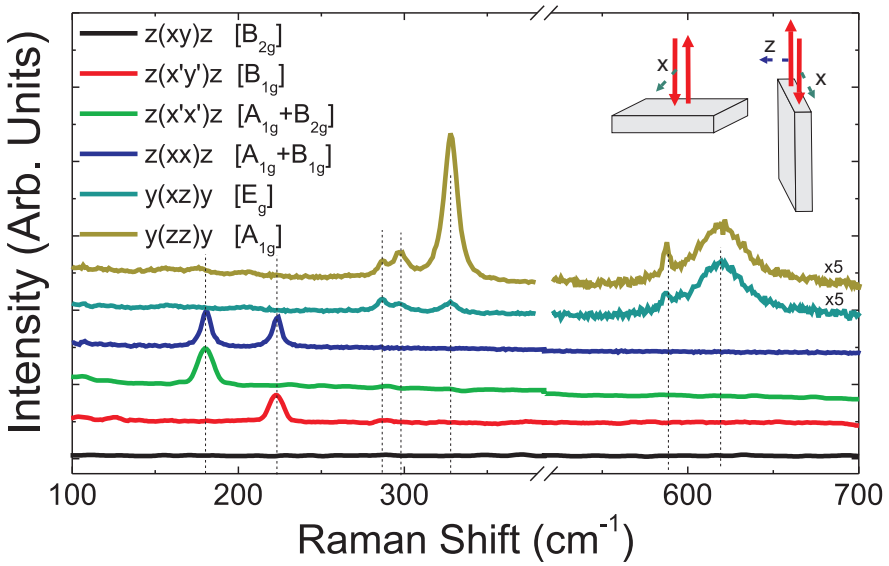

Figure 4.12: Mode assignment of LiFeAs - Room-temperature Raman spectra in $z(xy)z$, $z(x'y')z$, $z(x'x')z$, $z(xx)z$, $y(xz)y$, and $y(zz)y$ configurations. Spectra have been shifted vertically for clarity. Starting from the left, the peaks are assigned to A_{1g}(As), B_{1g}(Fe), E_g(Fe), E_g(Li), and A_{1g}(Li) vibrations. The inset indicates schematic scattering geometries.

from group symmetry analysis [note that E_u and E_g modes are doubly degenerate] (44). Among them, 3 modes ($1A_{2u}$ + $1E_u$) are acoustic modes, 6 modes ($2A_{2u}$ + $2E_u$) are IR active modes and 9 modes ($2A_{1g}$, $1B_{1g}$ and $3E_g$) are Raman active modes.

Fig. 4.12 shows the room temperature Raman spectra for several scattering geometries. The incident light wave vectors are along the c-axis [$z(xy)z$, $z(x'y')z$, $z(x'x')z$, $z(xx)z$ configurations], and along the b-axis [$y(zz)y$ and $y(xz)y$ configurations]. The $z(xy)z$, $z(x'y')z$, $z(x'x')z$ and $z(xx)z$ configurations probe the B_{2g}, B_{1g}, A_{1g} + B_{2g} and A_{1g} + B_{1g} symmetries, respectively. As expected from group symmetry analysis, no phonon modes are active in B_{2g} symmetry. In $z(xx)z$ configuration, two phonon modes are observed at 181 cm^{-1} and 223 cm^{-1}, and the modes are well separated into A_{1g} and B_{1g} symmetries, individually, and the modes at 181 cm^{-1} and 223 cm^{-1} therefore can be assigned to the A_{1g}(As) and B_{1g}(Fe) c-axis polarized vibrations of the FeAs planes.

The calculation of phonon frequencies from Jishi et al. in Ref. (3) based on the experimental lattice constants and atomic coordinates, is in better agreement with the experimentally observed phonon frequencies than the calculation from Huang et al.

in Ref. (4), where the relaxed lattice constants and atomic coordinates are used (see Table. 4.1). Furthermore, the A_{1g} and B_{1g} mode frequencies are also very similar to those in other families of iron-based superconductors: 170 cm^{-1} and 208 cm^{-1} in 1111 system (153), 182 cm^{-1} and 204 cm^{-1} in 122 system (154), and 155 cm^{-1} and 197 cm^{-1}) in 11 system (155). In $y(zz)y$ and $y(xz)y$ configurations, the phonon modes are active in A_{1g} and E_g symmetries, respectively. In the $y(zz)y$ configuration, three phonon modes are observed at 287 cm^{-1}, 297 cm^{-1} and 328 cm^{-1}. The intense mode at 328 cm^{-1} is considerably suppressed in the $y(xz)y$ configuration, and the mode can therefore be assigned to the c-axis polarized A_{1g}(Li) phonon mode rather than the in-plane E_g mode. It can be also confirmed as the frequencies of the modes are close to the calculated values.

Finally, the two remaining phonon modes at 287 cm^{-1} and 297 cm^{-1} are essentially assigned to the in-plane vibrations in E_g symmetry, although the mode frequency at 287 cm^{-1} deviates strongly from the calculated frequencies (240 cm^{-1} (3) and 225 cm^{-1} (4)), and the selection rules are not perfectly respected as two E_g modes are still visible in the $y(zz)y$ configuration.

Mode (atom)	Polarization	Selection Rule	Calc. Fre. (cm^{-1})		Exp. fitting parameters (cm^{-1})			
			Ref. (3)	Ref. (4)	ω_0	C	Γ_0	Γ
E_g (As)	in-plane	xz	121	173.7	-	-	-	-
A_{1g} (As)	c-axis	xx, $x'x'$ zz	188	183.3	185.1	1	0.24	1.3
B_{1g} (Fe)	c-axis	xx, $x'y'$	225	207.5	237.8	4	0.07	1.6
E_g (Fe)	in-plane	xz	240	224.7	289.2	0.9	0	1.1
E_g (Li)	in-plane	xz	294	233	308.2	3.7	0	3.3
A_{1g} (Li)	c-axis	xx, $x'x'$ zz	356	299.8	338.2	4	0	3.5

Table 4.1: Calculated Raman active phonon frequencies from Refs. (3) and (4), and our experimental results (see text for the definition of the parameters).

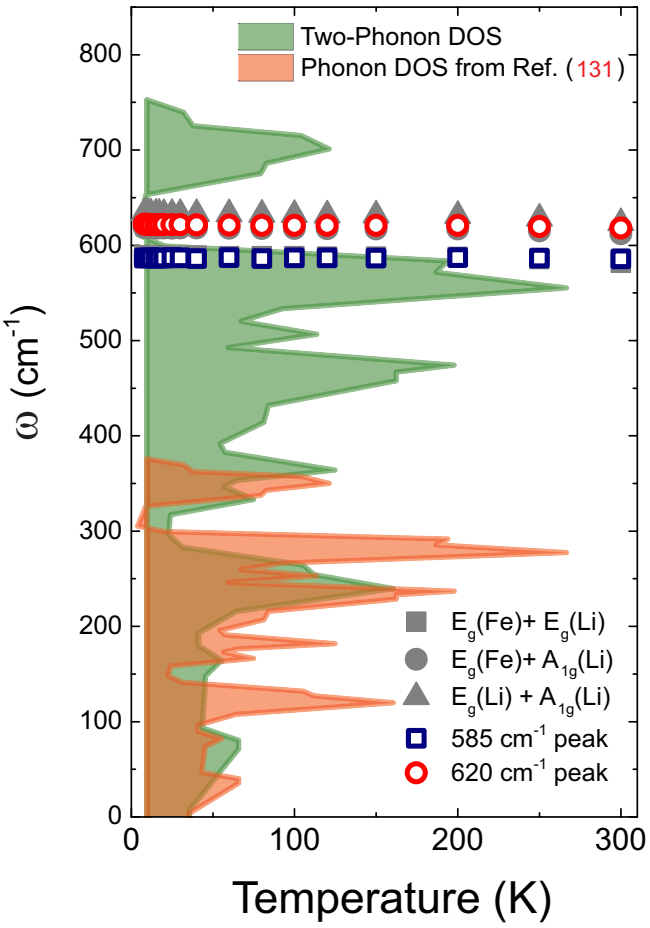

Figure 4.13: Two-phonon scattering mode in LiFeAs - Comparison of the temperature dependence of the frequencies of the high-energy modes at 585 cm^{-1} and 620 cm^{-1} with the sums of the frequencies of modes observed in $y(zz)y$ and $y(xz)y$ polarizations. The green curve describes the phonon DOS from Ref. (131), and the energy scale of the phonon DOS has been multiplied by two for the comparison with two-phonon scattering modes.

Actually, it is very hard to cleave the ac-plane as it is not a good cleavage plane, and align accurately in the glove box as well. As a consequence, there is always a misalignment between the incident light wave vector and a sample axis, and it might explain the observed leakage of the E_g modes. In our measurement, the lowest energy E_g(As) phonon mode predicted in the calculations, is not observed. The phonon assignments are summarized in Table. 4.1 with the fitting parameters obtained by the anharmonic phonon decay model, which will be discussed later.

Although all the expected phonon modes are well assigned, still there are two remaining modes at 585 cm^{-1} and 620 cm^{-1} in the ac-plane measurement. The frequencies of the modes greatly exceed the calculated highest phonon frequency of 356 cm^{-1}. Fig. 4.13 shows the temperature dependence of the frequencies of the observed high-energy phonon modes with the sums of the frequencies of the modes observed in $y(zz)y$ and $y(xz)y$ polarizations. For the comparison with the calculation, the energy scale of the phonon DOS (3, 131) has been multiplied by two and the phonon DOS is plotted together with the frequency of high energy phonon modes. First, the frequencies are not well aligned with the calculated phonon DOS. It might be caused by both the underestimation and overestimation in the calculation for the frequencies of E_g and A_{1g}(Li) modes, in particular, the E_g(Fe) mode is underestimated by 50 cm^{-1} (see Table. 4.1). Nevertheless. the frequency of the mode at 585 cm^{-1} is almost equal to the sum of the frequencies of the two E_g modes, *i.e.* E_g(Fe) + E_g(Li), even at all temperatures, and the mode at 620 cm^{-1} is in between the sums of the frequency of the A_{1g}(Li) with the frequency of each E_g modes, *i.e.* A_{1g}(Li) + E_g(Fe) and A_{1g}(Li) + E_g(Li). Hence, these high frequency phonon modes can be assigned to two-phonon scattering modes rather than single-phonon modes. Furthermore, the 620 cm^{-1} mode has a large linewidth of 35 cm^{-1} compared to the linewidth of the 585 cm^{-1} mode of 3.5 cm^{-1}. It suggests that several features which are not resolved individually, might be overlapped.

4.4.3 Temperature Dependence of Phonon Modes

Fig. 4.14 shows details of the fitting of the Raman data for selected temperatures and the temperature dependence of the frequencies and linewidths of the all observed phonon modes. The temperature dependence of the frequencies and linewidths of the phonon modes can be well fitted within a conventional symmetric anharmonic decay model (see Sec. 2.4.1). What has been found is: (i) the absence of phonon anomalies at any temperature, such as the splitting of the E_g modes predicted in Ref. (4), (ii) the absence of superconductivity-induced phonon renormalization, and (iii) a narrow residual linewidth Γ_0 which reflects the strength of the electron-phonon coupling and/or disorder.

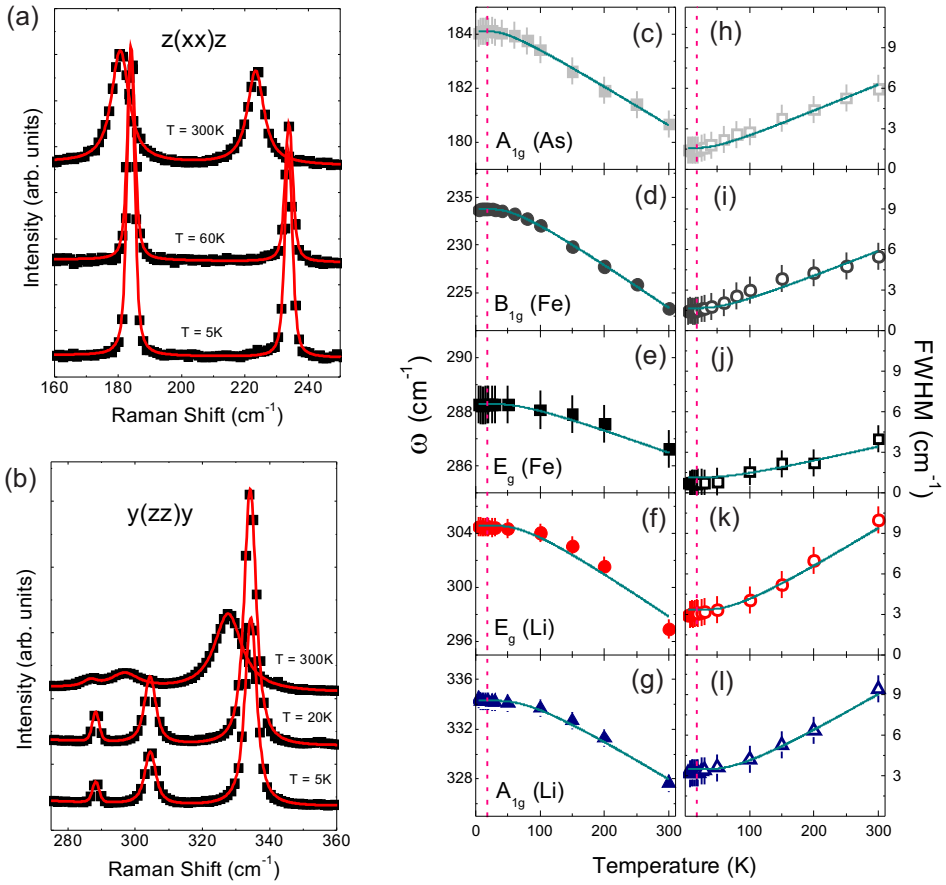

Figure 4.14: Temperature dependence of all phonon modes on LiFeAs - (a) ab-plane and (b) ac-plane measurements-active phonon modes for selected temperatures (room temperature, $T \sim T_c$, and the base temperature). Black squares are the raw data, red line is the fit following the procedure described in the text. The spectra have been shifted vertically for clarity. (c)-(g) Temperature dependence of frequencies (left panel) and (h)-(l) linewidths (right panel) of the five observed Raman active modes. The pink dashed line indicates T_c, and the green line is the result of a conventional phonon anharmonic model).

4.5 Discussion

4.5.1 Comparison with Other Families

- **Anisotropy of Raman tensor**

In our measurement, one interesting point is two A_{1g} modes of As and Li atoms are not visible in the same scattering geometries. The A_{1g}(As) is active in the ab-plane measurement [$z(xx)z$ and $z(x'x')z$ configurations], while the A_{1g}(Li) is active in the ac-plane measurement [$y(zz)y$ configuration] (see Fig. 4.12). The intensity of the A_{1g} mode is proportional to $(2\alpha_{xx})^2$ and $(\alpha_{zz})^2$ in the $z(xx)z$ (or $z(x'x')z$) and $y(zz)y$ configurations, respectively, where α_{zz} and α_{xx} are the diagonal elements of the A_{1g} Raman tensor (see Sec. 2.3.2). Our observations indicate that the A_{1g} Raman tensor components of As and Li atoms are different: $\alpha_{zz} \sim 0 << \alpha_{xx}$ for the A_{1g}(As) mode, while $\alpha_{xx} \sim 0 << \alpha_{zz}$ for the A_{1g}(Li) mode. Such similar anisotropy of A_{1g} the Raman tensor has also been reported in $SrFe_2As_2$, where $\alpha_{xx} \sim 0 << \alpha_{zz}$ (154).

- **Absence of phonon renormalization**

In previous phonon studies on iron-based superconductors where magnetic and structural transitions are present, phase transition-induced phonon renormalizations such as changes in frequency or linewidth (106, 107, 115, 155), or splitting of the E_g modes (115), have been observed. Moreover, in some cases, phonon anomalies have also been induced even if no phase transition is present (155). However, as shown in Fig. 4.14, in LiFeAs, none of the phonon modes show any anomalies at any temperature, although the DFT calculation based on the spin-polarized state, which is found to be a ground state of LiFeAs by first-principles calculations, predicted a splitting of the E_g modes. Our observations therefore further confirm that LiFeAs does not undergo any structural or magnetic phase transitions, ruling out the strong electron-phonon coupling through the spin channel predicted in Ref. (4, 152).

Similar to $Fe_{1+y}Te_{1-x}Se_x$ system, the superconductivity-induced effect is absent in LiFeAs. The reported superconducting gap of LiFeAs (Sec. 4.1.3) is much smaller than the phonon frequencies, and therefore the phonon frequencies remains essentially unaffected by the opening of superconducting gap (see Sec. 3.7.1).

4.5.2 Weak Electron-Phonon Coupling

When a phonon strongly couples to electrons, the phonon lineshape becomes a Fano profile, *i.e.* an asymmetric lineshape (see Sec. 2.4.2). However, all the observed Raman active phonon modes can be fitted very well by simple symmetric Lorentzian profiles

Mode	Exp. parameters (cm^{-1})		Calculated Γ (cm^{-1})	
(atom)	ω_0	Γ_0	$\lambda = 0.29$	$\lambda = 1.38$
E_g (As)	-	-	-	-
A_{1g} (As)	185.1	0.24	0.4	2.0
B_{1g} (Fe)	237.8	0.07	0.7	3.4
E_g (Fe)	289.2	0	1.1	5.0
E_g (Li)	308.2	0	1.2	5.7
A_{1g} (Li)	338.2	0	1.4	6.8

Table 4.2: Calculated phonon linewidth for weak and strong coupling parameters, and comparison to our experimental results.

as shown in Fig. 4.14(a)(b). In addition, as shown in Table. 4.1, the temperature-independent residual linewidth Γ_0 which reflects directly a coupling strength between electrons and phonons, is a vanishingly small, and much smaller than the temperature-dependent coefficient Γ. This implies that the lattice anharmonicity mainly contributes to the decay of phonons and the coupling strength of electrons and phonons is weak. In particular, the residual linewidths of the three phonons (E_g(As), E_g(Fe) and A_{1g}(Li)) suggested in ARPES measurements for the origin of the kinks in MDC (131), are below the resolution limit, implying very weak electron-phonon coupling, even though one of them (E_g(As)) can not be studied in the present work. Furthermore, the estimated FWHMs for weak coupling strength ($\lambda = 0.29$) using $\frac{1}{2}\pi N(0)\frac{\lambda}{n(\omega)}\omega^2$, where $N(0)$ is the electronic DOS ($N(0)_{LiFeAs} \sim 4/\text{eV}$), λ is electron-phonon coupling parameter, $n(\omega)$ is number of phonon branches ($n(\omega)_{LiFeAs} = 18$) and ω is phonon energy (38, 106), are in much better agreement with the experimental observation than those for strong coupling strength ($\lambda = 1.38$), and the obtained FWHMs are summarized in Table. 4.2. However, the possibility of strong electron-phonon coupling can not be completely ruled out, as the Raman measurement only allows the investigation of zone center phonons. A study of the phonon dispersion is therefore required.

4.6 Conclusions

The first study of the lattice dynamics in LiFeAs has been carried out, and five of the six expected phonon modes are observed. The phonon frequencies are in good

agreement with the frequencies obtained from density functional calculations, and the temperature dependence of phonon frequencies and linewidths is well described by a conventional anharmonic decay model. Neither clear anomalies associated with the superconducting transition nor any evidence for strong electron-phonon coupling are observed. This leads us to conclude that the coupling between electrons and phonons in LiFeAs is weak, at least for wavevectors close to the Brillouin zone center.

5

$NaFe_{1-x}Co_xAs$

Superconductivity with $T_c \sim 8$ K has also been discovered in parent NaFeAs (111-type) which is isostructural and isoelectronic with LiFeAs. Interestingly, the properties in NaFeAs are rather different from those of LiFeAs: (i) magnetic and structural transitions are present in parent NaFeAs, in particular, $T_{SDW} \sim 40$ K is well separated from a structural transition at $T_S \sim 50$ K. (ii) Superconductivity is enhanced upon both charge carrier doping ($T_c^{max} \sim 20$ K) and external pressure ($T_c^{max} \sim 30$ K). The properties in NaFeAs are indeed closer to those of other families of iron-based superconductors rather than LiFeAs. Hence, NaFeAs would be a promising compound to bridge the gap between LiFeAs and other families of iron pnictides, and provide insights into general features of superconductivity in iron-based superconductors.

In particular, a key issue in NaFeAs is the pairing mechanism as several techniques indicate the different superconducting gap size and coupling strength in Co-doped $NaFe_{1-x}Co_xAs$. The initial ARPES study and STM measurement have suggested strong coupling ratio between the superconducting gap and k_BT_c ($2\Delta \sim 8\ k_BT_c$), while a recent ARPES and NMR measurement have observed weak coupling ratio ($2\Delta \sim 4\ k_BT_c$). Hence, the study about the strength of electron-phonon coupling can provide further insights about the such issues.

In this chapter, I will report first lattice dynamics study on NaFeAs using Raman scattering spectroscopy. In Sec. 5.1, I will discuss general properties and issues in NaFeAs. In Sec. 5.2, I will describe samples which were used in this work, and in Sec. 5.3, 5.4, I will discuss our experimental observations, and then finally, in Sec. 5.5, I will make conclusions.

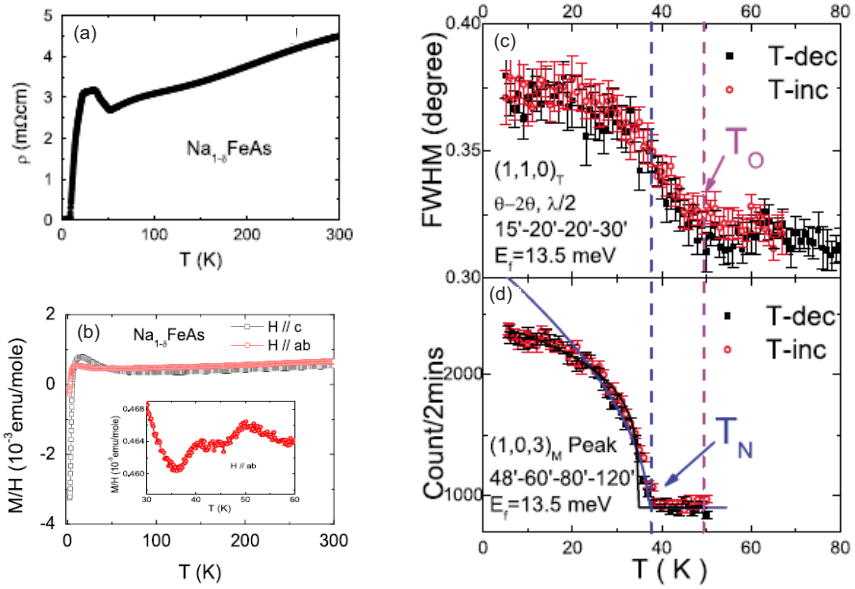

Figure 5.1: Structural and magnetic transitions in NaFeAs - (a) (b) The in-plane resistivity and magnetic susceptibility of NaFeAs, respectively from Ref. (156). (c) (d) Temperature dependence of FWHM of nuclear Bragg peak and intensity of magnetic Bragg peak on NaFeAs, respectively from Ref. (158). Structural and AFM transitions occur at different temperatures ($T_S \sim 50$ K and $T_{AFM} \sim 40$ K).

5.1 Properties and Issues in NaFeAs

5.1.1 Crystal Structure

Superconductivity with $T_c \sim 8$ K has also been discovered in NaFeAs which is isostructural and isoelectronic with LiFeAs (13, 156, 157). The lattice symmetry of NaFeAs is exactly same as LiFeAs (See Fig. 4.1), and is described by the Cu_2Sb-type (or anti-PbO-type) tetragonal structure (space group P4/nmm (D_{4h}^7)) with Na, Fe and As atoms located at 2c, 2b, and 2c Wyckoff positions, respectively. Lattice parameters are a = 3.9494 Åand c = 7.0396 Åat room temperature (13).

5.1.2 Electronic and Magnetic Structure

NaFeAs is metallic as shown by the resistivity data displayed in Fig. 5.1(a) (156). Upon cooling, NaFeAs shows well separated multiple phase transitions. First, it undergoes a tetragonal-to-orthorhombic structural transition at ~ 50 K, then an AFM transition

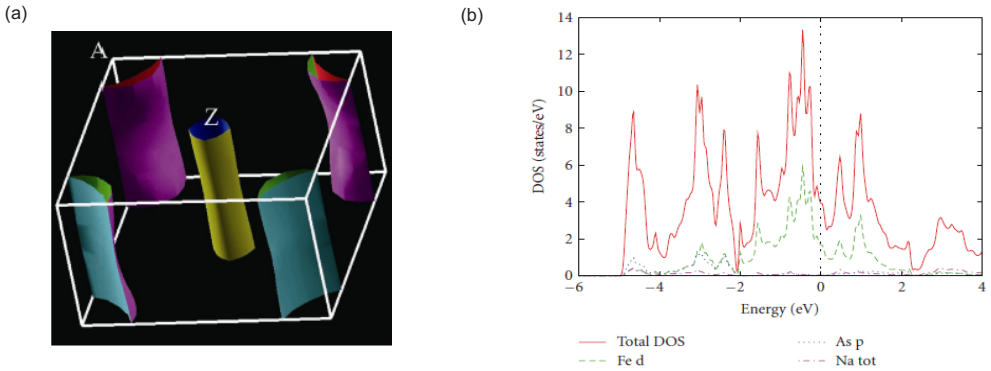

Figure 5.2: Electronic structure of NaFeAs - (a) Electronic structure of NaFeAs from Ref. (159). (b) Electronic density-of-state (DOS) from Ref. (3).

occurs at $\sim$ 40 K (158). Fig. 5.1(c)(d) shows the temperature dependence of the FWHM of a nuclear Bragg peak (which due to unresolved splitting of the peak by the orthorhombic distortion) and the intensity of a magnetic Bragg peak of NaFeAs,

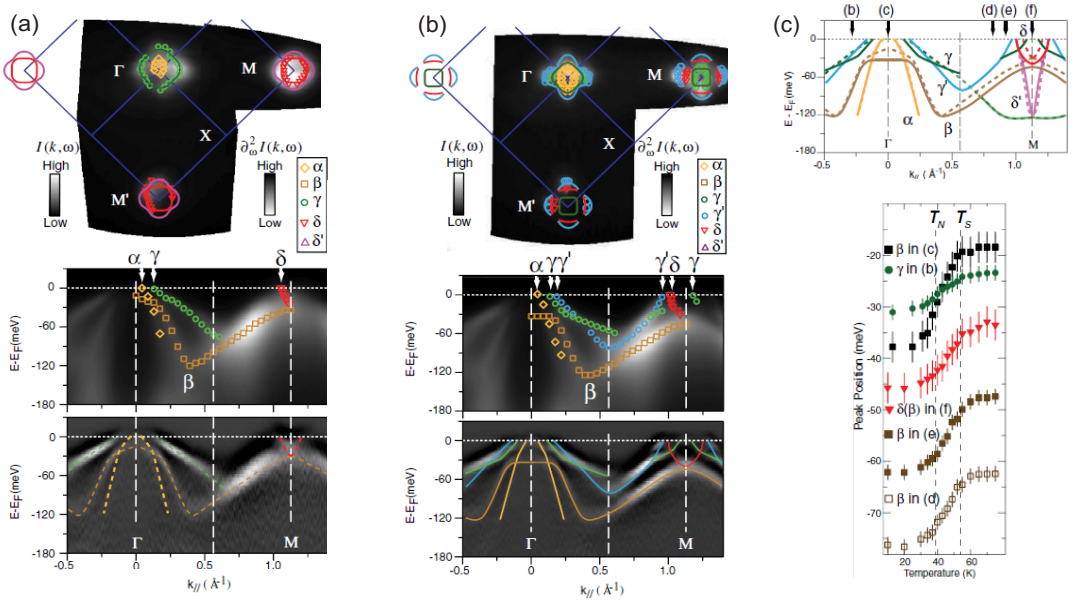

Figure 5.3: Fermi surface topology of NaFeAs - (a) Electronic structure of NaFeAs at $\sim$ 60 K from Ref. (160). Hole pockets at the Γ point and electron pockets at the M point. (b) Electronic structure of NaFeAs at $\sim$ 10 K. (c) The normal state (dashed curves) and SDW state (solid curves) band structures and temperature dependence of the band positions.

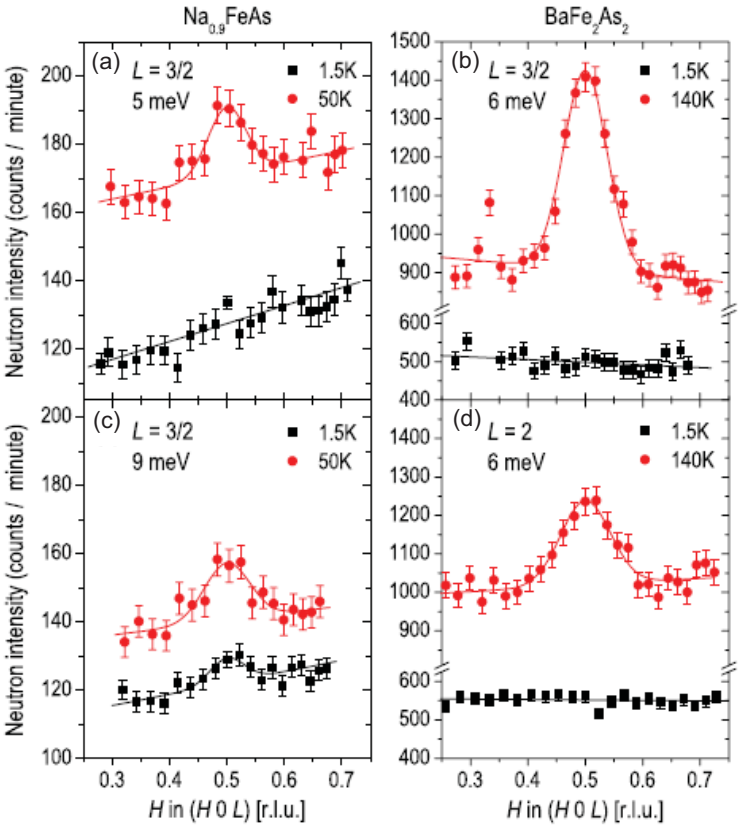

Figure 5.4: Magnetic excitation in NaFeAs - (a) (b) Magnetic excitations in NaFeAs for energy transfers 5 meV and 9 meV, respectively from Ref. (33). The magnetic excitations are centered at (π, π) with the spin gap of $\sim$ 10 meV. (c) (d) Magnetic excitations in $BaFe_2As_2$

respectively. The linewidth of the nuclear Bragg peak starts to broaden at $\sim$ 50 K, while the magnetic Bragg peak appears at $\sim$ 40 K. The structural and magnetic transitions are thus clearly separated in parent NaFeAs. Finally, superconductivity appears at $\sim$ 8 K (see Fig. 5.1(a)(b)) (156).

- **Electronic structure**

The initial band structure calculation has predicted a similar Fermi surface topology to that of LiFeAs (hole pockets around the Γ point and electron pockets around the M point) as shown in Fig. 5.2 (159), and experimentally, it has been confirmed by several ARPES measurements (see Fig. 5.3) (160, 161, 162, 163). When the system

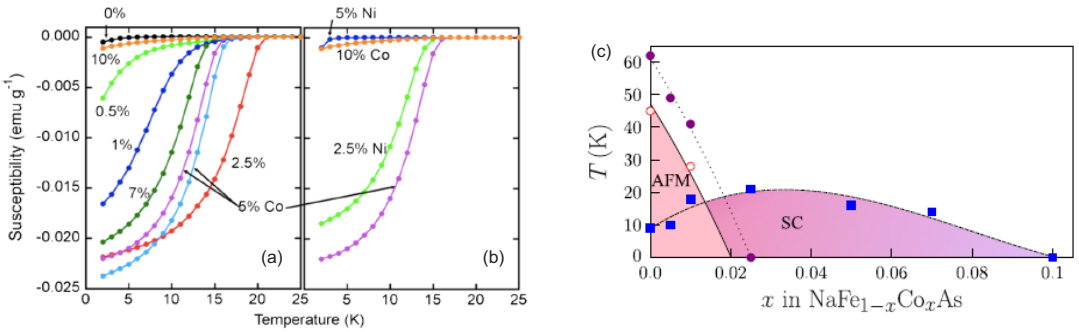

Figure 5.5: Superconductivity in NaFeAs upon chemical doping - ZFC magnetic susceptibilities for (a) $NaFe_{1-x}Co_xAs$ and (b) $NaFe_{1-x}Ni_xAs$ samples from Ref. (82). (c) Phase diagram for $NaFe_{1-x}Co_xAs$.

enters into the SDW state, the normal state electronic structure drastically changes as shown in Fig. 5.3(b). First, an additional band γ' appears and a cross-like spectral weight redistribution occurs at the M point, and the β and δ bands start to shift at the structural transition temperature. As a consequence, the authors of Ref. (160) have suggested that structural and magnetic transitions share a common origin.

- **Magnetic structure**

Inelastic neutron scattering measurements on NaFeAs have observed the stripe AFM order along (π, π) and a similar order of magnitude of a spin gap ($\sim$ 10 meV) to 122 family (33), although the magnetic ordering temperature (45 K) is much lower than T_N (137 K) in $BaFe_2As_2$ and the magnetic moments ($\sim$ 0.1 - 0.2 μ_B by muon spin rotation (μSR) (13, 164), $\sim$ 0.09 μ_B by neutron diffraction (158), and $\sim$ 0.3 μ_B by NMR (165)) are smaller than those of the 122 system ($\sim$ 1.0 μ_B) (166, 167). Recently, however, a SDW gap ($2\Delta_{SDW}$ = 33 meV) which closes at the magnetic transition temperature has been observed in STM measurements (168).

5.1.3 Superconducting State

- **Chemical doping**

As already shown in Fig. 5.1(a), NaFeAs shows superconductivity at $\sim$ 8 K. When additional charge carriers are introduced by the substitution of Co or Ni on the iron site, the structural and magnetic transitions are suppressed and superconductivity is

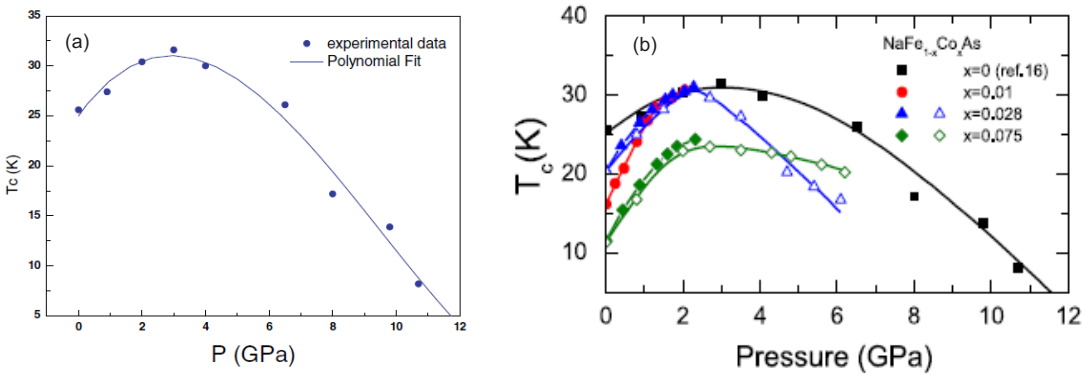

Figure 5.6: Superconductivity in NaFeAs under high pressure - (a) T_c under high pressure in parent NaFeAs from Ref. (171). (b) T_c under high pressure in Co-doped NaFeAs from Ref. (172). T_c is enhanced up to $\sim$ 30 K. Note that the obtained $T_c \sim$ 25 K in undoped NaFeAs might indicate that Na deficiencies are present in the sample.

enhanced (see Fig. 5.5(a)(b)). Fig. 5.5(c) shows a phase diagram as a function of Co concentration. T_c is enhanced up to $\sim$ 20 K when 3% of Co is substituted for Fe (82). In addition, T_c can also be enhanced by interacting with environment (169, 170). Environmental reaction causes Na deficiencies in the system (which acts as chemical doping) and enhances T_c.

- **High pressure**

Fig. 5.6 shows phase diagrams as a function of external pressure on both parent and Co-doped $NaFe_{1-x}Co_xAs$ samples. As applying external pressure, T_c is gradually enhanced up to $\sim$ 30 K in both parent and Co-doped $NaFe_{1-x}Ni_xAs$ samples. Taken together with chemical doping effect, the mechanism of achieving superconductivity in NaFeAs is essentially closer to that in other families of iron-based superconductors rather than LiFeAs. Note that the usual T_c is $\sim$ 10 K for undoped NaFeAs. Thus the obtained $T_c \sim$ 25 K in Fig. 5.6 (171) might indicate that Na deficiencies are present in the sample (169).

- **Superconducting gap**

The superconducting gap has been measured on $NaFe_{1-x}Co_xAs$ by several techniques: STM ($\Delta \sim$ 5.5 meV for x = 0.028) (168), ($\Delta \sim$ 4.5 meV for x = 0.05) (173),

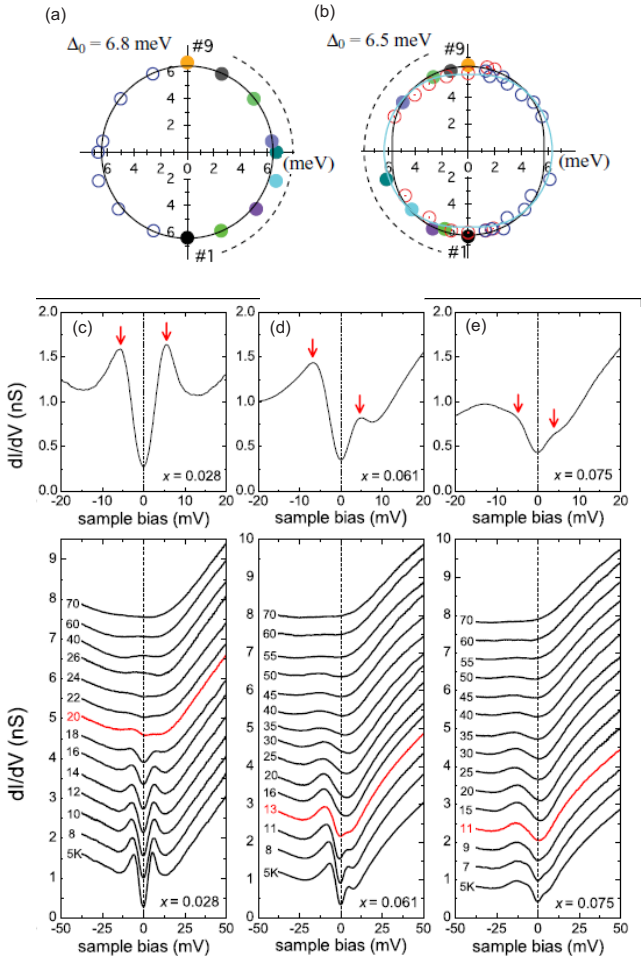

Figure 5.7: Superconducting gap in $NaFe_{1-x}Co_xAs$ - (a) (b) Superconducting gap size for the α and the γ (δ) Fermi surfaces determined by ARPES, respectively from Ref. (161). Two isotropic gaps ($\Delta \sim 6.8$ meV on hole pockets and 6.5 meV on electron pockets) are observed. (c) (d) (e) Superconducting gap size for $NaFe_{0.972}Co_{0.028}As$, $NaFe_{0.939}Co_{0.061}As$ and $NaFe_{0.925}Co_{0.075}As$ at 5 K determined by STM, with their temperature evolution, respectively from Ref. (168).

NMR ($\Delta \sim 3.6$ meV for x = 0.025) (174), ARPES ($\Delta \sim 6.8$ meV on hole pockets and 6.5 meV on electron pockets for x = 0.05) (161), ($\Delta \sim 3.3$ meV on hole pockets and 2.9 meV on electron pockets for x = 0.05) (162), and specific heat ($\Delta \sim 3.1$ meV and 5.4 meV for x = 0.028) (175).

The superconducting gap symmetry and strength of pairing in $NaFe_{1-x}Co_xAs$ are controversial. First, initial ARPES measurement on $NaFe_{0.95}Co_{0.05}As$ and specific heat

measurement on $NaFe_{0.72}Co_{0.028}As$ have suggested two nodeless isotropic $s_{\pm}$-wave superconducting gaps ruling out a nodal gap symmetry, and strong coupling ratio ($2\Delta \sim 8\ k_BT_c$) and ($2\Delta \sim 6.1\ k_BT_c$), respectively (see Fig. 5.7(a)(b)) (161, 175). Furthermore, STM measurements on $NaFe_{0.972}Co_{0.028}As$ have also found a strong coupling ratio ($2\Delta \sim 6.4\ k_BT_c$) (see Fig. 5.7(c)) (168), and a recently reported thermal conductivity study on $NaFe_{0.972}Co_{0.028}As$ supports a nodeless isotropic gap (176). These features are similar to those in other families of iron-based superconductors. On the other hand, recent ARPES measurements on $NaFe_{0.95}Co_{0.05}As$ have suggested two isotropic superconducting gaps with a weak coupling ratio ($2\Delta \sim 4\ k_BT_c$) (162), similar to LiFeAs, in good agreement with a NMR study on $NaFe_{0.975}Co_{0.025}As$ (174). Finally, contrary to the isotropic nodeless gap, London penetration depth measurements on $NaFe_{0.972}Co_{0.028}As$ have suggested a highly anisotropic nodal gap (177).

The controversial experimental situation has stimulated a debate whether the pairing mechanism is phonon-mediated or not. A study of the coupling strength between electrons and phonons can provide further insights into the pairing mechanism. So far, no studies of the lattice dynamics that would allow a direct determination of the strength of the electron-phonon coupling have been reported for NaFeAs. This motivates the present work.

5.2 Sample Characterizations

Single crystals of $NaFe_{1-x}Co_xAs$ (x = 0, 0.03) were grown by Min et al. using a sealed tungsten crucible and a Bridgman method as described in Ref. (33, 128). Typical magnetic and superconducting transition temperatures were measured by a SQUID and PPMS. Furthermore, inelastic neutron scattering measurements where NaFeAs samples from the same batch were used, have determined the structural and magnetic transition temperatures (seen Fig. 5.8(b)(c) (33)). Sample preparations for Raman measurements were carefully carried out as NaFeAs crystals are extremely air sensitive. In particular, they were cleaved and mounted on the cold finger of a helium-flow cryostat in a glove box under Ar atmosphere.

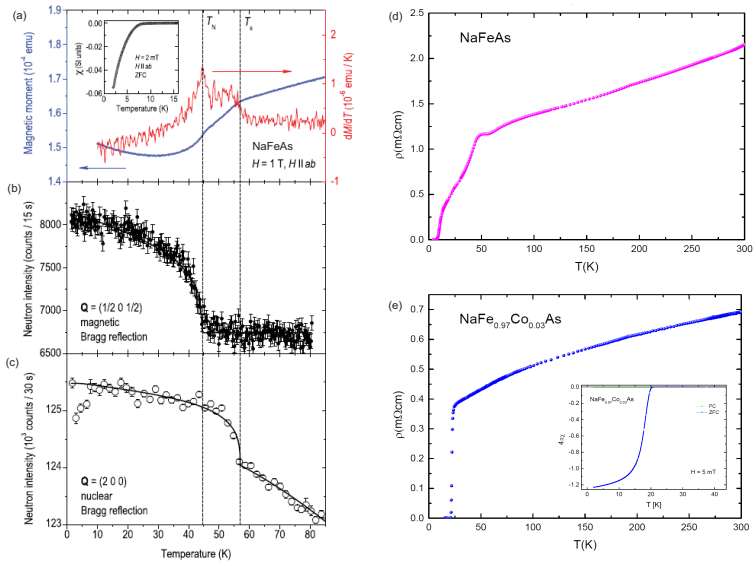

Figure 5.8: Characterization of $NaFe_{1-x}Co_xAs$ - Structural and AFM transition on parent NaFeAs from Ref. (33), where the same batch of the sample was used. (a) Magnetization curve (blue) and its derivative (red). Two kinks which correspond to T_N and T_S, respectively, are visible. The inset shows superconducting transition at ~ 8 K. (b) magnetic Bragg intensity, and (c) nuclear Bragg intensity. (d) Resistivity on NaFeAs. (e) Resistivity on $NaFe_{0.97}Co_{0.03}As$. The inset shows superconducting transition at ~ 20 K.

5.3 Experimental Results

5.3.1 Experimental Conditions and Data Analysis

All Raman light scattering experiments were performed on freshly cleaved surfaces and the samples were mounted in a helium-flow cryostat. Spectra were taken in backscattering geometry through a JobinYvon LabRam 1800 single grating spectrometer, and a linearly polarized He^+/Ne^+ mixed gas laser with $\lambda = 632.817$ nm has been used for excitation. The power of the incident beam was kept below 1 mW with a ~ 5 μm diameter spot on the sample surface.

In order to analyze the low energy phonon modes, the air spectrum has been recorded and subtracted from the raw data. Fig. 5.9 shows the raw data, the air spectrum and air-subtracted data. For data analysis, the air-subtracted data has been used for whole temperature range.

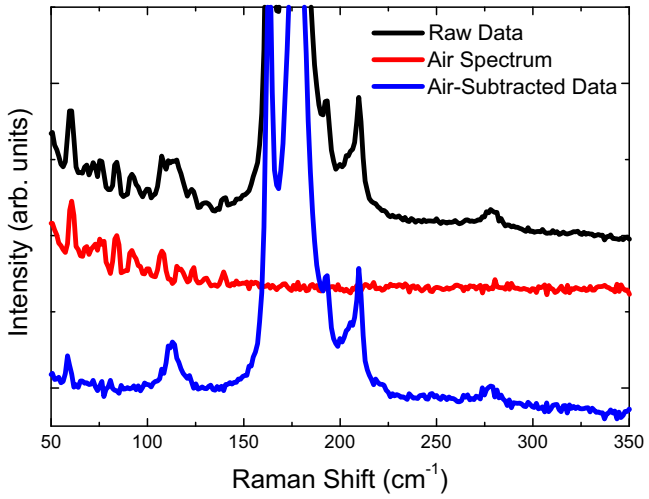

Figure 5.9: Raman spectra with air spectrum - Base-temperature Raman spectrum on NaFeAs with air spectrum. The air spectrum has been extracted from the raw data.

5.3.2 Mode Assignment

As the lattice symmetry of stoichiometric NaFeAs is in the space group $P4/nmm$ (D_{4h}^7), with Na, Fe and As atoms at 2c, 2b, and 2c Wyckoff positions, respectively, one would expect 18 zone-center phonon modes ($\Gamma_{NaFeAs} = 2A_{1g} + 1B_{1g} + 3A_{2u} + 3E_u + 3E_g$) from group symmetry analysis [note that E_u and E_g modes are doubly degenerated] (44). Among them, 3 modes ($1A_{2u} + 1E_u$) are acoustic modes, 6 modes ($2A_{2u} + 2E_u$) are IR active modes and 9 modes ($2A_{1g}$, $1B_{1g}$ and $3E_g$) are Raman active modes.

Fig. 5.10 shows the room temperature Raman spectra for several scattering geometries. The incident light wave vectors are along the c-axis [$z(xy)z$, $z(x'x')z$, $z(x'y')z$, $z(xx)z$ configurations], and along the b-axis [$y(zz)y$ and $y(xz)y$ configurations]. In the $z(xy)z$, $z(x'y')z$, $z(x'x')z$ and $z(xx)z$ configurations, the B_{2g}, B_{1g}, $A_{1g} + B_{2g}$ and $A_{1g} + B_{1g}$ symmetries are probed, respectively. As expected from group symmetry analysis, no phonon modes are active in B_{2g} symmetry. In $z(xx)z$ configuration, two phonon modes are observed at 163 cm^{-1} and 213 cm^{-1}, and the modes are well separated into A_{1g} and B_{1g} symmetries, individually. Therefore, the modes at 163 cm^{-1} and 213 cm^{-1} can be assigned to the A_{1g}(As) and B_{1g}(Fe) c-axis polarized vibrations of the FeAs planes. The proximity of the frequencies of the modes with the calculation and similar phonon in other families of iron-based superconductors (181 cm^{-1} and 223 cm^{-1}

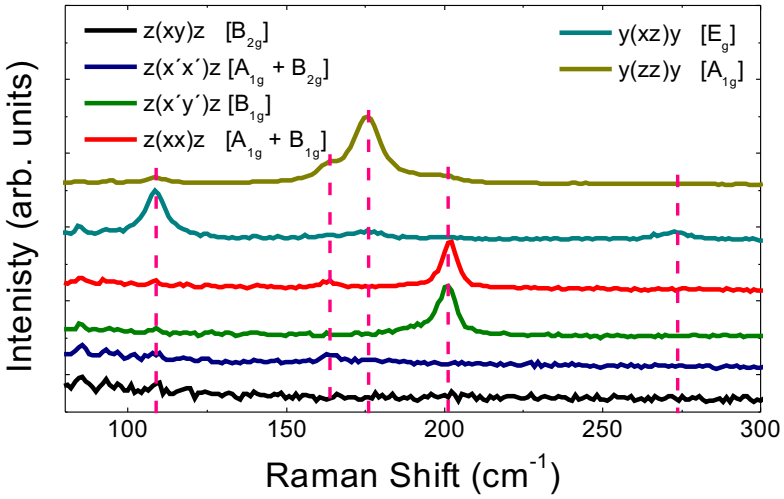

Figure 5.10: Mode assignment of NaFeAs - Room temperature Raman spectra in $z(xy)z$, $z(x'x')z$, $z(x'y')z$, $z(xx)z$, $y(xz)y$, and $y(zz)y$ configurations. Spectra have been shifted vertically for clarity. Starting from the left, the peaks are assigned to E_g(As), A_{1g}(As), A_{1g}(Na), B_{1g}(Fe), and E_g(Fe) vibrations.

in LiFeAs (109), 170 cm^{-1} and 208 cm^{-1} in the 1111 system (153), 182 cm^{-1} and 204 cm^{-1} in 122 system (154), and 155 cm^{-1} and 197 cm^{-1}) in the 11 system (155)) further confirms this assignment. In $y(zz)y$ and $y(xz)y$ configurations, the phonon modes are active in A_{1g} and E_g symmetries, respectively. The intense mode at 178 cm^{-1} in the $y(zz)y$ configuration is considerably suppressed in $y(xz)y$ configuration, and this phonon can therefore be assigned to the third c-axis polarized A_{1g}(Na) mode. Finally, the two remaining modes at 113 cm^{-1} and 281 cm^{-1} in $y(xz)y$ configuration can be attributed to the in-plane vibrations in E_g symmetry, in particular E_g(As) and E_g(Fe), respectively. It can be also confirmed as the frequencies of the modes are close to the calculated values (see Table. 5.1). In ac-plane measurement, the selection rules are not perfectly respected, possibly due to polarization leaks caused by the same reasons as already mentioned in 4.4.2. In the measurements, the E_g(Na) phonon mode predicted in the calculations, is not observed. The phonon assignments are summarized in Table. 5.1 with the fitting parameters obtained by the anharmonic phonon decay model.

5.3.3 Temperature Dependence of Phonon Modes

Fig. 5.11 shows the temperature dependence of the frequencies and linewidths of all observed phonon modes for NaFeAs and $NaFe_{0.97}Co_{0.03}As$ samples with the fits using a simple symmetric anharmonic phonon decay model (see Sec. 2.4.1) (45, 46). Several remarkable features can be pointed out in the data. First, in parent NaFeAs, no phonon anomalies are observed through phase transitions in c-axis polarized A_{1g}(As) and B_{1g}(Fe) modes. This is unusual case because most phonon studies have observed phonon renormalizations through phase transitions, in particular, the SDW transition (106, 107, 155, 178). Second, an unusual temperature dependence of the phonon linewidth has been observed. The in-plane E_g(As) and c-axis polarized A_{1g}(Na) phonon modes broaden with decreasing temperature in parent NaFeAs (see Fig. 5.11(f)(h)). Third, the E_g(As) mode starts to sharpen at $\sim$ 100 K, which is significantly higher than both transition temperatures of our sample (T_{SDW} = 45 K and T_S = 57 K), and the sharpening is suppressed in the Co-doped $NaFe_{0.97}Co_{0.03}As$ sample. Fourth, contrary to the case of $Fe_{1+y}Te_{1-x}Se_x$ where the unusual linewidth broadening disappear

Mode (atom)	Polarization	Selection Rule	Calc. Fre. (cm^{-1})		Exp. fitting parameters (cm^{-1})			
			Ref. (3)	Ref. (5)	ω_0	C	Γ_0	Γ
E_g (As)	in-plane	xz	110	126	113	0.8	-	-
A_{1g} (As)	c-axis	xx, $x'x'$ zz	176	174	163	0.1	1.9	1.0
B_{1g} (Fe)	c-axis	xx, $x'y'$	218	227	213	2.7	0.3	0.9
E_g (Fe)	in-plane	xz	241	256	281	3.8	-	-
E_g (Na)	in-plane	xz	187	203	-	-	-	-
A_{1g} (Na)	c-axis	xx, $x'x'$ zz	199	198	178 2	0.9	-	-

Table 5.1: Calculated Raman-active phonon frequencies and selection rules from Refs. (3) and (5) and comparison to our experimental results (see text for the definition of the parameters).

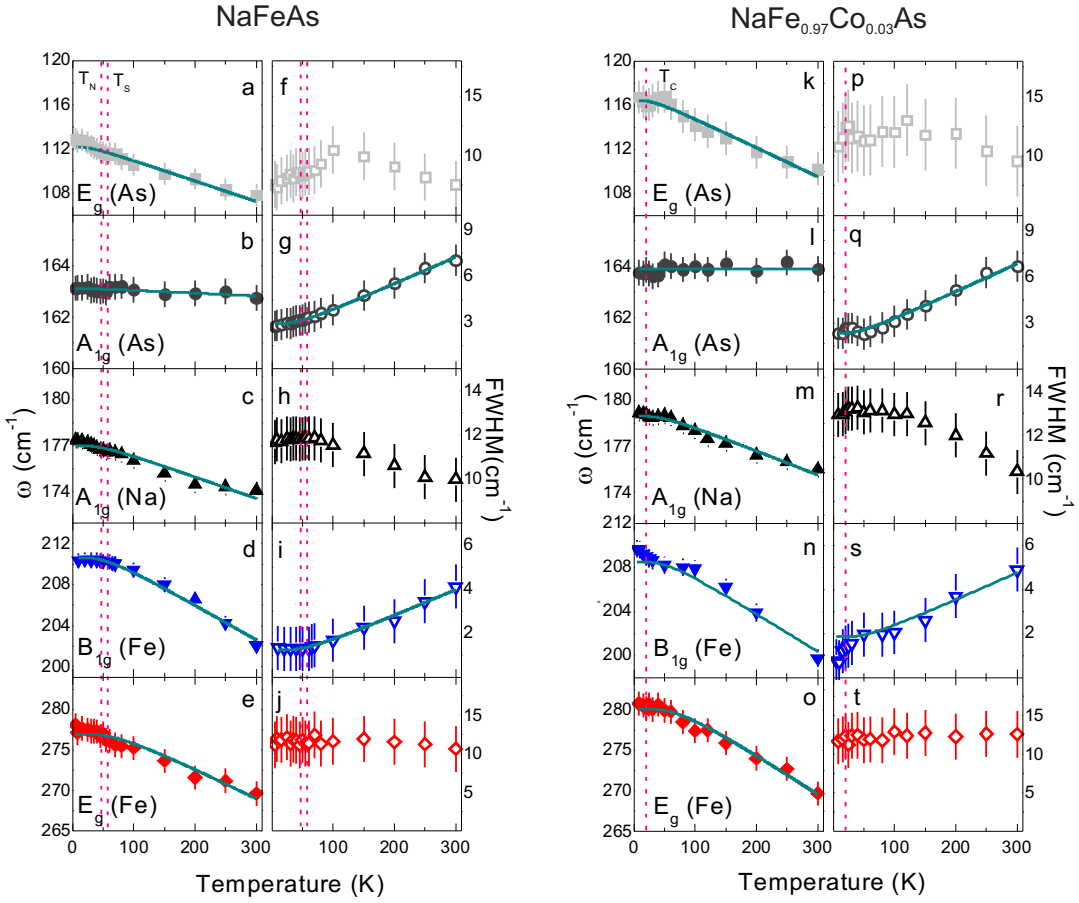

Figure 5.11: Temperature dependence of all phonon modes on $NaFe_{1-x}Co_xAs$ - ([Left panel: NaFeAs] Temperature dependence of the mode (a) - (e) frequencies, and (f) - (j) linewidths. Pink dashed lines correspond to T_{SDW} and T_S. [Right panel: $NaFe_{0.97}Co_{0.03}As$] Temperature dependence of the mode (k) - (o) frequencies, and (p) - (t) linewidths. Pink dashed line corresponds to T_c. The green line is the result of a conventional phonon anharmonic model.

upon doping, in the optimally doped $NaFe_{0.97}Co_{0.03}As$ sample, the irregular broadening essentially remains in the both modes (see Fig. 5.11(p)(r)), in particular, the low temperature linewidth of A_{1g}(Na) mode is much broader than that in parent NaFeAs (see Fig. 5.11(h)(r)). Finally, for the B_{1g}(Fe) mode, a slight superconductivity-induced phonon hardening and narrowing have been observed (see Fig. 5.11(n)(s)).

5.4 Discussion

5.4.1 Comparison with Other Families

- **Anisotropy of Raman tensor**

In NaFeAs, an anisotropy of the intensity of phonon modes in A_{1g} symmetry is observed. In the ab-plane measurement [$z(xx)z$ and $z(x'x')z$ configurations], the A_{1g}(As) is active, while in the ac-plane measurement [$y(zz)y$ configuration], both A_{1g}(As) and A_{1g}(Na) modes are active (see Fig. 5.10). Interestingly, the intensity of the A_{1g}(As) mode in the $y(zz)y$ configuration is stronger than the intensity in $z(xx)z$ and $z(x'x')z$ configurations, contrary to LiFeAs, where the same A_{1g}(As) mode is only visible in $z(xx)z$ and $z(x'x')z$ configurations. The intensity of the A_{1g} mode is proportional to $(2\alpha_{xx})^2$ and $(\alpha_{zz})^2$ in the $z(xx)z$ (or $z(x'x')z$) and $y(zz)y$ configurations, respectively, where α_{zz} and α_{xx} are the diagonal elements of the A_{1g} Raman tensor (see Sec. 2.3.2). Our observations indicate that the A_{1g} Raman tensor components of As and Na atoms are anisotropic: $0 < \alpha_{xx} < \alpha_{zz}$ for the A_{1g}(As) mode, while $\alpha_{xx} \sim 0 << \alpha_{zz}$ for the A_{1g}(Na) mode. In addition, there is also anisotropy in the Raman tensor components between NaFeAs and LiFeAs, as (i) α_{xx} for the A_{1g}(As) in NaFeAs is considerably weaker than that in LiFeAs, and (ii) in NaFeAs, the E_g(As) (E_g(Na)) mode is active (inactive), while in LiFeAs, the E_g(As) (E_g(Li)) mode is inactive (active). The comparison of Raman tensor components with LiFeAs are summarized in Table. 5.2.

- **Absence of phase transition-induced effects**

In most of phonon studies in iron-based superconductors, phase transition-induced phonon renormalization in either (both) frequency or (and) linewidth has been observed

Mode(atom)	NaFeAs	LiFeAs
A_{1g}(As)	$0 < \alpha_{xx} << \alpha_{zz}$ $\alpha_{xx}^{NaFeAs} << \alpha_{xx}^{LiFeAs}$	$\alpha_{zz} \sim 0 << \alpha_{xx}$
A_{1g}(Na/Li)	$\alpha_{xx} \sim 0 << \alpha_{zz}$	$\alpha_{xx} \sim 0 << \alpha_{zz}$
E_g(As)	$0 << \alpha_{xz}, \alpha_{yz}$	$\alpha_{xz}, \alpha_{yz} \sim 0$
E_g(Na/Li)	$\alpha_{xz}, \alpha_{yz} \sim 0$	$0 << \alpha_{xz}, \alpha_{yz}$

Table 5.2: The comparison of Raman tensor components for the phonon modes of As and Na/Li atoms between NaFeAs and LiFeAs.

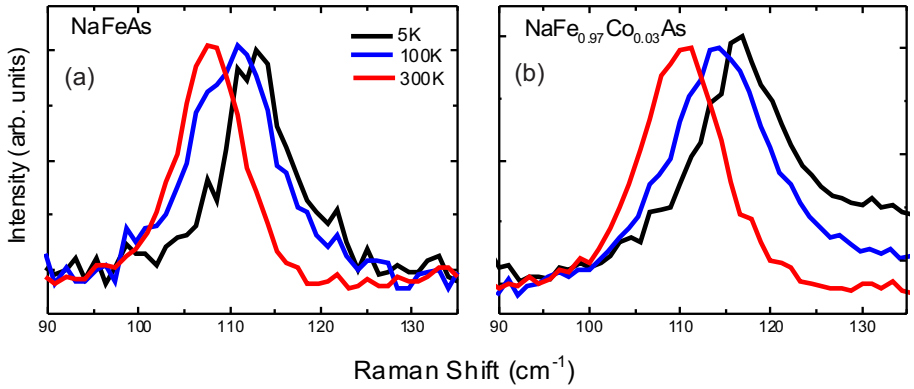

Figure 5.12: Normalized Raman spectra of E_g(As) mode for several temperatures on parent NaFeAs and $NaFe_{0.97}Co_{0.03}As$ - (a) E_g(As) phonon in parent NaFeAs for selected temperatures (room temperature, $T \sim 100K$ and base temperature). The spectrum at 100 K is broader than the spectrum at room and base temperatures. (b) Same plot for $NaFe_{0.97}Co_{0.03}As$. The spectrum at 100 K is broader than the spectrum at room temperature, but similar to the spectrum at base temperature.

in the c-axis polarized modes (106, 107, 155, 178). In particular, when the SDW gap opens, the phonon linewidth usually narrows following the reduction of the electronic DOS at the Fermi level. However, such phase transition-induced effects are absent in NaFeAs, although the structural and magnetic transitions are obviously present and the SDW gap has been observed (168).

5.4.2 Possibility of Pseudogap-like feature

In parent NaFeAs, the narrowing of the E_g(As) mode has been observed, but such narrowing starts not at the phase temperatures ($T_{SDW} = 45$ K and $T_S = 57$ K) but at ~ 100 K, which is well above both transition temperatures. Such linewidth narrowing starting at 100 K is clearly visible in the raw data. Fig. 5.12(a) shows the E_g(As) phonon spectra of parent NaFeAs for selected temperatures (room temperature, $T \sim 100K$ and base temperature). The spectrum at 100 K is obviously broader than the spectrum at base temperature.

The narrowing linewidth in the phonon spectrum of a metallic system usually implies the gap opening which changes the electronic DOS at the Fermi level. The narrowing linewidth then reflects the increasing phonon lifetime. However, it seems that the

opening of SDW gap is not sufficient to explain the observed narrowing of E_g(As) mode, because according to a recent report the SDW gap in parent NaFeAs closes completely at 40 K (168). So far, there is no available report of the presence of the gap above this temperature yet, but theoretically it has been proposed that a pseudogap-like phase can be driven by a nematic order induced by a thermal magnetic fluctuations (179), and experimentally it has been suggested that thermal magnetic fluctuations induce a Fermi surface reconstruction in parent NaFeAs (160). Furthermore, recently in the in-plane resistivity measurements, a kink has been observed at 100 K (169, 170, 180) which might imply a change of the electronic DOS at the Fermi level. The kink disappears in the Co-doped sample. However, in our resistivity data, we could not observe clear evidence of a kink at this temperature, although the raw data behaves similar to the reported one (see Fig. 5.8(d)). As a consequence, the origin of the observed effect remains unresolved.

5.4.3 Presence of Magnetic Fluctuation

As already discussed, in both parent NaFeAs and Co-doped $NaFe_{0.97}Co_{0.03}As$, an anomalous temperature dependence of phonon linewidths has been observed for E_g(As) and A_{1g}(Na) modes (see Fig. 5.11(f)(h) and (p)(r)). This effect is clearly visible in the raw data. First, as shown in Fig. 5.12, the linewidth of the E_g(As) mode at 100 K is broader than that at room temperature in both compounds, and the linewidth of the A_{1g}(Na) mode at 5 K is also broader than the one at room temperature (see Fig. 5.13(a)(b)).

In the most of materials, the phonon linewidth decreases with decreasing temperature as the phonon linewidth is inversely proportional to its lifetime. To our knowledge, the only Fe-based compound in which an anomalous broadening in the Raman phonon has been observed is $Fe_{1+y}Te_{1-x}Se_x$, and this has been interpreted as a coupling between phonon and magnetic fluctuation (see Sec. 3.7.3). In the case of NaFeAs, this interpretation is also relevant, where impurity scattering including the non-stoichiometric Na concentration effect is expected to induce temperature-independent broadening, a possible additional damping channel for phonon modes can be the coupling between phonons and thermal magnetic fluctuations. Indeed, DFT phonon calculations suggested a strong electron-phonon coupling via the spin channel in NaFeAs (5, 181). Spin

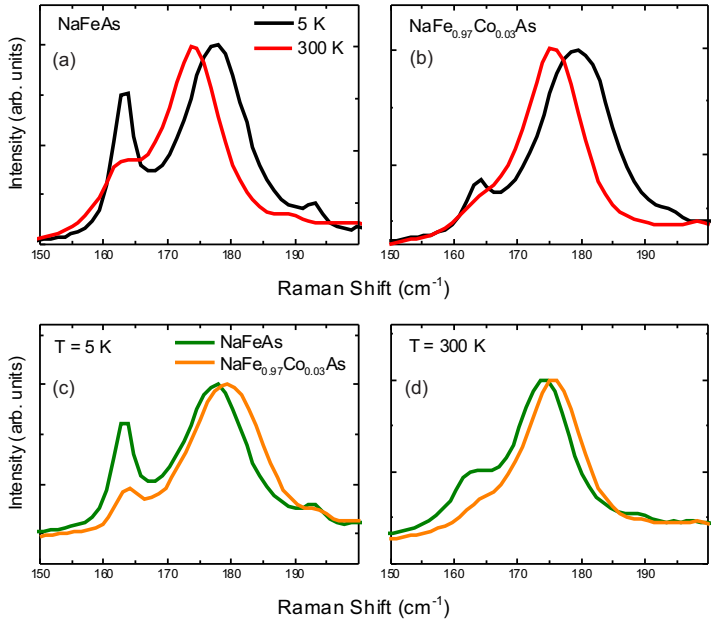

Figure 5.13: Normalized Raman spectra of A_{1g}(Na) mode for room and base temperatures on parent NaFeAs and $NaFe_{0.97}Co_{0.03}As$ - (a) A_{1g}(Na) phonon spectra in parent NaFeAs for room and base temperatures. The spectrum at 5 K is broader than the spectrum at room temperature. (b) Same plot for $NaFe_{0.97}Co_{0.03}As$. The spectrum at 5 K is also broader than the spectrum at room temperature. (c) A_{1g}(Na) phonon spectra for parent NaFeAs and $NaFe_{0.97}Co_{0.03}As$ at 5 K. The spectrum of $NaFe_{0.97}Co_{0.03}As$ is broader than the spectrum of parent NaFeAs. (d) Same plot at room temperature. Both spectra have similar linewidth.

fluctuations have also been reported in a 3% Co-doped compound, although static magnetic order is no longer present (see Fig. 5.13(c)(d)). In contrast, the unconventional phonon linewidth broadening in $Fe_{1+y}Te_{1-x}Se_x$ is suppressed upon doping, following the behavior of the static magnetic order. Hence, the remaining spin fluctuations might be related to either (both) a different amount of dopant or (and) a different doping mechanism between 3% of Co-substituted $NaFe_{0.97}Co_{0.03}As$ and $Fe_{0.95}Te_{0.56}Se_{0.44}$.

5.4.4 Superconductivity-induced Effects

So far, most of the Raman studies could not observe the superconductivity-induced phonon renormalization through T_c (106, 121, 154) and we also did not observe such effect in $Fe_{1+y}Te_{1-x}Se_x$ and LiFeAs (see Sec. 3 and Sec. 4). This is expected, because

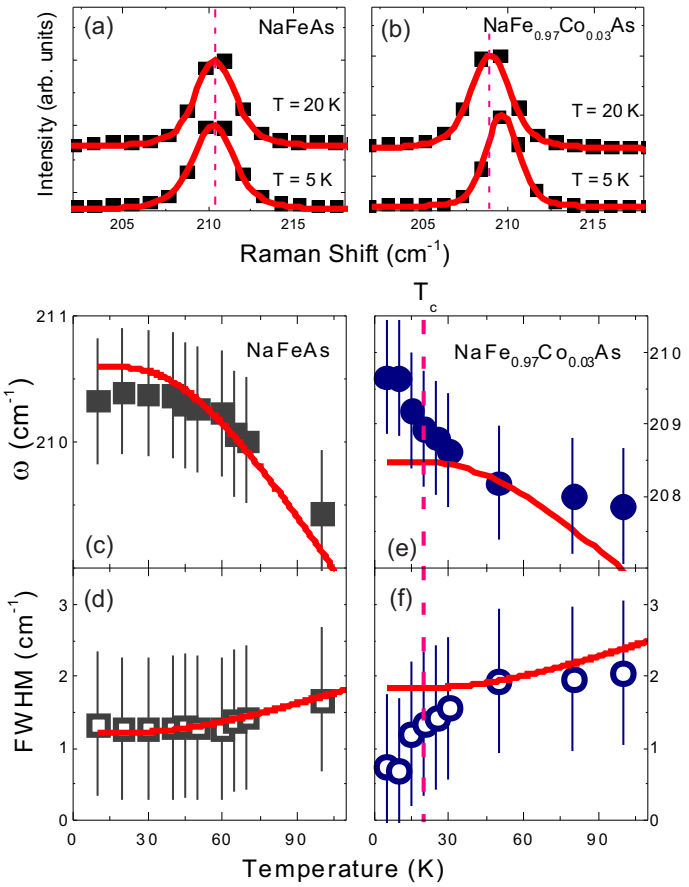

Figure 5.14: B_{1g}(Fe) mode for parent NaFeAs and $NaFe_{0.97}Co_{0.03}As$ - (a) Normalized Raman spectra of the B_{1g}(Fe) for 5 K and 20 K for NaFeAs. Black squares are the raw data, red line is the fit. The spectra have been shifted vertically for clarity. (b) Same plot for $NaFe_{0.97}Co_{0.03}As$. (c) (d) Low temperature frequency and linewidth of B_{1g}(Fe) mode for NaFeAs, respectively. The red line is the result of a conventional phonon anharmonic model. (e) (f) Same plot for $NaFe_{0.97}Co_{0.03}As$. The pink dashed line marks T_c of $NaFe_{0.97}Co_{0.03}As$.

the superconducting gap amplitude is much smaller than the phonon frequencies, as discussed in Sec. 3.7.1. Nevertheless, a small hardening of the B_{1g} phonon through T_c has been reported in some 122 systems (107, 108).

In the case of optimally doped $NaFe_{0.97}Co_{0.03}As$, although the reported superconducting gap amplitude (2Δ = 11 meV ($\sim$ 88 cm^{-1})) from STM (168), 2Δ = 10.72

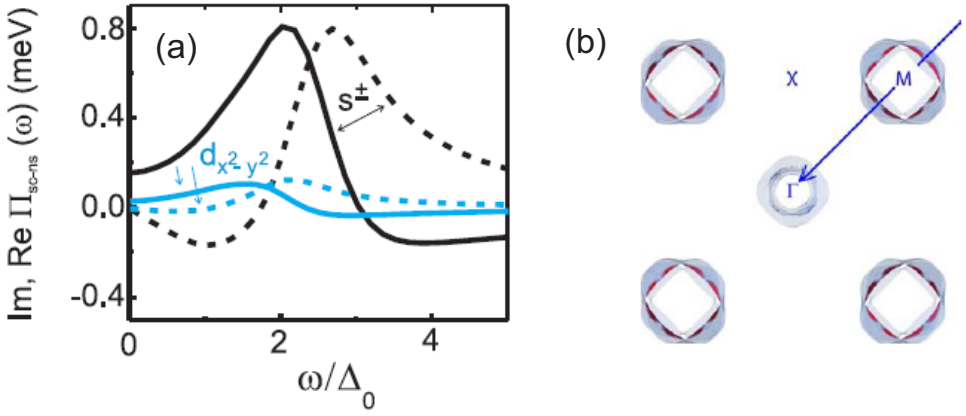

Figure 5.15: Superconductivity-induced phonon self-energy and B_{1g} Raman vertices - (a) Calculated superconductivity-induced phonon self-energy for single band $d_{x^2-y^2}$-wave and multiband $s_{\pm}$-wave symmetries from Ref. (107). (b) Calculated Raman vertices for B_{1g} symmetry from Ref. (182). The shaded parts are Fermi surfaces and dark red is the place where maximal values of the B_{1g} vertex appear.

meV ($\sim$ 86.5 cm^{-1})) from the specific heat (175), and $2\Delta = 13.6$ meV ($\sim$ 109.7 cm^{-1})) from ARPES (161)) is also much smaller than the energy of the mode (26.4 meV), the B_{1g} phonon is affected by superconducting transition. The superconductivity-induced effects can be seen clearly in Fig. 5.14, where the low temperature frequency and linewidth behaviors of the B_{1g}(Fe) mode for NaFeAs and $NaFe_{0.97}Co_{0.03}As$ are presented. As shown in Fig. 5.14(a)(b), in parent NaFeAs, the spectrum at 5 K is almost identical to the spectrum at 20 K, while in $NaFe_{0.97}Co_{0.03}As$, the hardening and narrowing clearly occur through T_c.

Choi et al. in Ref. (107) have calculated the superconductivity-induced phonon self-energy effect based on a four-band model for the $s_{\pm}$-wave gap symmetry: two hole and electron pockets at the Γ and M points, respectively. As shown by Fig. 5.15(a), they obtained the following results: (i) in the case $\omega_{ph} < 2\Delta_{SC}$, where ω_{ph} and Δ_{SC} denote phonon energy and superconducting gap energy, respectively, the phonon mode softens and narrows, as the phonon energy is not sufficient to break Cooper pairs, (ii) in the case $\omega_{ph} > 2\Delta_{SC}$, the phonon mode hardens and broadens, because the phonon breaks Cooper pairs. The obtained results are same as the results based on the d-wave single band model (49). The only difference is the relative intensity of the phonon renormalization. The hardening of the B_{1g} phonon frequency in $NaFe_{0.97}Co_{0.03}As$ is

in good agreement with the calculation, as its energy (26.4 meV) is obviously higher than the reported highest superconducting gap energy ($2\Delta = 13.6$ meV). On the other hand, the observed linewidth narrowing of the B_{1g} phonon mode is more puzzling.

Related with the superconductivity-induced effect in phonon spectrum, two main issues can be assigned:

(i) Why does the superconductivity-induced effect occur only for the B_{1g} mode?

(ii) Why does the B_{1g} phonon narrow below T_c, although the energy of the phonon is higher than the superconducting gap energy?

The first question is related to the symmetry dependent electron-phonon coupling discussed in Ref. (182). The A_{1g} and B_{1g} symmetries do not couple to the electron pockets at the M point (π, π). They rather probe Γ (0,0) and X (π,0) points, respectively. Only phonons of B_{2g} symmetry couple to the electron pockets. However, as shown by Fig. 5.15(b), when vertices for electronic Raman scattering are considered, one is led to conclude that the B_{1g} symmetry couples to the electron pockets, while the A_{1g} symmetry probes the Γ point. As a consequence, the B_{1g} phonon is the most likely candidate for superconductivity-induced effect, because no B_{2g} phonon is available in this system. In addition, further insights can be gained from the Ref. (39), where a large isotope effect on the iron site has been observed. The isotope effect in T_c is directly related to the role of phonons in the superconducting state. The observed large isotope effect on the Fe atom may therefore imply that phonon modes of Fe atoms play an important role in the superconducting state.

The answer to issue (ii) is more difficult, because the available data is limited. Nevertheless, what we know is (i) a single band approach does not explain our observation, and (ii) a simple multiband approach without considering intra- and inter-band scattering also does not work. One should therefore take into account both intra-band and inter-band scattering in future calculations. Theoretically, it has been pointed out such intra- and inter-band scattering play important roles not only in superconducting gap anisotropy but also in the issue of pair breaking by impurities (18). However, it has not been investigated in this work how the intra- and inter-band scattering affects the scattering between phonons and Cooper pairs, and a further study of this point is therefore required.

5.5 Conclusions

The first study of the lattice dynamics in the parent compound NaFeAs and in optimally doped $NaFe_{0.97}Co_{0.03}As$ has been reported. Five of the six expected phonon modes were observed and the phonon frequencies are in good agreement with the frequencies obtained from density functional calculations. In NaFeAs, indications of a pseudogap-like phenomenon and an unconventional temperature dependence of the phonon linewidths have been found. They might be caused by phonon-spin fluctuation coupling, in E_g(As) and A_{1g}(Na) modes. This unusual behavior persists in the optimally doped $NaFe_{0.97}Co_{0.03}As$ and becomes even stronger. Finally, a clear superconductivity-induced effect in the frequency and linewidth of the B_{1g}(Fe) mode has been observed, which can not be understood within a single band and simple multiband approaches. Further work is required to access whether an interplay between intra- and inter-band scattering might explain these observations.

6

Summary

We have investigated the lattice dynamics of the 11 ($Fe_{1+y}Te_{1-x}Se_x$) and 111 (LiFeAs /$NaFe_{1-x}Co_xAs$) families of iron-based superconductors, by means of Raman spectroscopy. In this chapter, the main experimental results will be summarized.

- **SDW-induced effect**

Spin-density-wave (SDW) is a common state of the parent compounds of iron-based superconductors. Previous phonon studies of the parent 122 system have revealed manifestation of the SDW gap opening, which reduces the electronic density-of-states (DOS) at the Fermi level, and thus renormalizes the phonon energy and lifetime (hardening and narrowing) (106, 107, 115). Similar to the parent 122 system, we have observed that the SDW transition affects the phonon self-energy in the parent 11 compound ($Fe_{1.02}Te$). However, at the same time, we have also found the SDW-induced phonon renormalization can be possibly suppressed by magnetic fluctuations (see the results on parent $Fe_{1.09}Te$ (Sec. 3.5) and NaFeAS (Sec. 5.3)).

- **Spin fluctuation-induced effect**

The most remarkable feature we observed in the 11 and 111 systems is the broadening of the phonon linewidth with decreasing temperature, even in the normal state. In most materials, the phonon linewidth narrows with decreasing temperature, as phonon-phonon interactions are reduced with decreasing temperature. The anomalous broadening we found in both 11 and 111 compounds implies the existence of an additional phonon decay channel. Since we observed that the anomalous broadening disappear

when magnetic order is suppressed in the 11 compound, we conclude that the additional phonon decay channel is of magnetic origin.

- **Superconductivity-induced effect**

In iron-based superconductors, most Raman studies could not observe any superconductivity-induced phonon renormalization through T_c (106, 121), presumably because the superconducting energy gap is much smaller than the phonon energies. This is also the case for the 11 and 111 (LiFeAs) compounds. However, some Raman studies of 122 compounds (107, 108) have found that superconductivity can affect the phonon frequency although the superconducting gap energy is much smaller than the phonon energy. Similar to those 122 compounds, we also found a superconductivity-induced effect on the $NaFe_{1-x}Co_xAs$ 111 compound. The most interesting observation was, unlike the d-wave cuprate case and a calculation based on simple multiband $s_{\pm}$-wave model (107), the B_{1g} phonon narrows below T_c, although its energy exceeds the superconducting gap energy. We have conjectured that both intra- and inter-band scattering might play an important role in the superconductivity-induced phonon anomalies in iron-based superconductors.

References

[1] C. Thomsen, G. Kaczmarczyk, *Vibrational Raman Spectroscopy of High-temperature Superconductors* (John Wiley & Sons Ltd, Chichester, 2002). ix, 23

[2] D. Einzel, R. Hack, *JOURNAL OF RAMAN SPECTROSCOPY* **27**, 307 (1996). ix, 27, 28

[3] R. A. Jishi, H. M. Alyahyaei, *Advances in Condensed Matter Physics* **2010**, 804343 (2010). ix, x, 77, 79, 80, 81, 83, 91, 100

[4] G. Q. Huang, *et al.*, *Physical Review B* **82**, 014511 (2010). ix, 77, 78, 81, 83, 85

[5] S. Deng, *et al.*, *Physical Review B* **80**, 214508 (2009). x, 100, 104

[6] J. G. Bednorz, K. A. Müller, *Zeitschrift für Physik B Condensed Matter* **64**, 189 (1986). 1

[7] Y. Kamihara, *et al.*, *Journal of the American Chemical Society* **130**, 3296 (2008). 1, 70

[8] H. Takahashi, *et al.*, *Nature* **453**, 376 (2008). 1

[9] R. Zhi-An, *et al.*, *Chinese Phys. Lett.* **25**, 2215 (2008). 1

[10] M. Rotter, *et al.*, *Physical Review Letters* **101**, 107006 (2008). 1

[11] M. Tegel, *et al.*, *Journal of Physics: Condensed Matter* **20**, 452201 (2008). 1

[12] J. H. Tapp, *et al.*, *Physical Review B* **78**, 060505 (2008). 1, 70, 74

[13] D. R. Parker, *et al.*, *Chemical Communications* p. 2189 (2009). 1, 90, 93

REFERENCES

[14] F. C. Hsu, *et al.*, *Proc Natl Acad Sci U S A* **105**, 14262 (2008). 1, 36, 42, 74

[15] K.-W. Yeh, *et al.*, *Europhysics Letters* **84**, 37002 (2008). 1, 36, 42, 65

[16] M. H. Fang, *et al.*, *Physical Review B* **78**, 224503 (2008). 1, 36, 42

[17] C. W. Chu, *Nature Physics* **5**, 787 (2009). 2

[18] P. J. Hirschfeld, *et al.*, *Reports on Progress in Physics* **74**, 124508 (2011). 3, 108

[19] J. Paglione, R. L. Greene, *Nature Physics* **6**, 645 (2010). 2, 6

[20] D. J. Singh, M. H. Du, *Physical Review Letters* **100**, 237003 (2008). 3, 4, 38

[21] D. H. Lu, *et al.*, *Nature* **455**, 81 (2008). 3, 4

[22] A. A. Kordyuk, *Low Temperature Physics* **38**, 888 (2012). 3, 4

[23] J. Dong, *et al.*, *Europhysics Letters* **83**, 27006 (2008). 3, 5

[24] I. I. Mazin, *et al.*, *Physical Review Letters* **101**, 057003 (2008). 3

[25] M. D. Lumsden, A. D. Christianson, *J Phys Condens Matter* **22**, 203203 (2010). 5

[26] C. de la Cruz, *et al.*, *Nature* **453**, 899 (2008). 4, 5, 38

[27] R. McQueeney, *et al.*, *Physical Review Letters* **101**, 227205 (2008). 5

[28] R. Klingeler, *et al.*, *Physical Review B* **81**, 024506 (2010). 5

[29] G. M. Zhang, *et al.*, *Europhysics Letters* **86**, 37006 (2009). 5

[30] T. Yildirim, *Physical Review Letters* **101**, 057010 (2008). 5

[31] C. Fang, *et al.*, *Physical Review B* **77**, 224509 (2008). 5

[32] C.-C. Lee, *et al.*, *Physical Review Letters* **103**, 267001 (2009). 5

[33] J. T. Park, *et al.*, *Physical Review B* **86**, 024437 (2012). 6, 92, 93, 96, 97

[34] H. Ding, *et al.*, *EPL (Europhysics Letters)* **83**, 47001 (2008). 6, 7

[35] H. Fong, *et al.*, *Physical Review Letters* **75**, 316 (1995). 7, 42

[36] D. S. Inosov, *et al.*, *Nature Physics* **6**, 178 (2010). 7, 42

[37] Mazin, *Nature* **464**, 183 (2010). 7

[38] L. Boeri, *et al.*, *Physical Review Letters* **101**, 026403 (2008). 7, 8, 86

[39] R. H. Liu, *et al.*, *Nature* **459**, 64 (2009). 7, 9, 108

[40] M. Cardona, G. Giüntherodt, *Light Scattering in Solids II: Basic Concepts and Instrumentation* (Springer-Verlag Berlin Heidelberg, 1982). 16

[41] P. Y. Yu, M. Cardona, *Fundamentals of Semiconductors* (Springer Heidelberg Dordrecht London New York, 2010). 17, 18, 19

[42] M. H. Bakr, *Electronic and Phononic Raman Scattering in Twin-Free* $YBa_2Cu_3O_{6+x}$ (Dissertation, 2010). 19

[43] F. A. Cotton, *Chemical Applications of Group Theory, 3rd ed.* (New York: Wiley, 1990). 23

[44] D. L. Rousseau, *et al.*, *Journal of Raman Spectroscopy* **10**, 253 (1981). 23, 53, 80, 98

[45] P. Klemens, *Physical Review* **148**, 845 (1966). 24, 56, 58, 100

[46] J. Menendez, M. Cardona, *Physical Review B* **29**, 2051 (1984). 24, 33, 56, 58, 100

[47] U. Fano, *Physical Review* **124**, 1866 (1961). 25

[48] M. Rahlenbeck, *Raman light scattering study on phonon anomalies in unconventional superconductors* (Dissertation, 2010). 26

[49] R. Zeyher, G. Zwicknagl, *Zeitschrift für Physik B Condensed Matter* **78**, 175 (1990). 25, 107

[50] V. G. Hadjiev, *et al.*, *physica status solidi (b)* **215**, 183 (1999). 26

[51] T. P. Devereaux, *Reviews of Modern Physics* **79**, 175 (2007). 27

[52] G. Blumberg, *et al.*, *Physica C: Superconductivity* **456**, 75 (2007). 28

[53] J. R. Ferraro, *et al.*, *Introductory Raman Spectroscopy* (Academic Press, 2003). 33

[54] E. Pomjakushina, *et al.*, *Physical Review B* **80**, 204517 (2009). 36, 47

[55] J. Wen, *et al.*, *Reports on Progress in Physics* **74**, 124503 (2011). 36, 47

[56] E. Uchida, H. Kondoh, *Journal of the Physical Society of Japan* **10**, 357 (1955). 36

[57] P. Terzieff, K. L. Komarek, *Monatshefte für Chemie* **109**, 651 (1978). 36

[58] W. Schuster, *et al.*, *Monatshefte für Chemie* **110**, 1153 (1979). 36

[59] D. Fruchart, *et al.*, *Materials Research Bulletin* **10**, 169 (1975). 36, 40

[60] M. Bendele, *et al.*, *Physical Review B* **82**, 212504 (2010). 36, 37, 45, 46, 62

[61] S. Li, *et al.*, *Physical Review B* **79**, 054503 (2009). 36, 37, 38, 40, 45, 65

[62] W. Bao, *et al.*, *Physical Review Letters* **102**, 247001 (2009). 36, 37, 45

[63] G. F. Chen, *et al.*, *Physical Review B* **79**, 140509 (2009). 36, 37, 38, 64

[64] R. Khasanov, *et al.*, *Physical Review B* **80**, 140511 (2009). 36, 37, 41, 42, 45, 66, 67

[65] T. L. Xia, *et al.*, *Physical Review B* **79**, 140510 (2009). 36, 46, 47, 48, 53, 54

[66] Y. Xia, *et al.*, *Physical Review Letters* **103**, 037002 (2009). 36, 38, 39, 40, 64

[67] T. Klein, *et al.*, *Physical Review B* **82**, 184506 (2010). 36, 42, 51, 65

[68] A. Martinelli, *et al.*, *Physical Review B* **81**, 094115 (2010). 36, 45, 64, 65

[69] Y. Zhang, *et al.*, *Physical Review B* **82**, 165113 (2010). 36, 38, 39, 40, 45

[70] Y. Liu, C. T. Lin, *Journal of Superconductivity and Novel Magnetism* **24**, 183 (2010). 37, 51

[71] C. Stock, *et al.*, *Physical Review B* **84**, 045124 (2011). 37, 45, 46, 67

[72] A. Subedi, *et al.*, *Physical Review B* **78**, 134514 (2008). 38, 39, 62, 65

[73] K. Nakayama, *et al.*, *Physical Review Letters* **105**, 197001 (2010). 38, 42, 43

[74] H. Gretarsson, *et al.*, *Physical Review B* **84**, 100509 (2011). 38, 74

[75] I. Zaliznyak, *et al.*, *Physical Review Letters* **107**, 216403 (2011). 40, 46

[76] F. Ma, *et al.*, *Physical Review Letters* **102**, 177003 (2009). 40

[77] M. J. Han, S. Y. Savrasov, *Physical Review Letters* **103**, 067001 (2009). 40

[78] Y. Mizuguchi, *et al.*, *Journal of the Physical Society of Japan* **78**, 074712 (2009). 41, 42

[79] Y. Mizuguchi, *et al.*, *Applied Physics Letters* **94**, 012503 (2009). 41, 42

[80] A. S. Sefat, *et al.*, *Physical Review Letters* **101**, 117004 (2008). 41

[81] H. Chen, *et al.*, *Europhysics Letters* **85**, 17006 (2009). 41

[82] D. R. Parker, *et al.*, *Physical Review Letters* **104**, 057007 (2010). 41, 93, 94

[83] M. D. Lumsden, *et al.*, *Nature Physics* **6**, 182 (2010). 42, 44

[84] A. D. Christianson, *et al.*, *Nature* **456**, 930 (2008). 42

[85] M. Lumsden, *et al.*, *Physical Review Letters* **102**, 107005 (2009). 42

[86] T. Hanaguri, *et al.*, *Science* **328**, 474 (2010). 42, 43, 44, 65

[87] Y. Noat, *et al.*, *J Phys Condens Matter* **22**, 465701 (2010). 42, 65

[88] T. Kato, *et al.*, *Physical Review B* **80**, 180507 (2009). 42, 65

[89] D. Arcon, *et al.*, *Physical Review B* **82**, 140508 (2010). 42, 65

[90] J. E. Hoffman, *A Search for Alternative Electronic Order in the High Temperature Superconductor* $Bi_2Sr_2CaCu_2O_{8+d}$ *by Scanning Tunneling Microscopy* (Dissertation, 2003). 43

[91] T. Hanaguri, *et al.*, *Science* **323**, 923 (2009). 43, 44

[92] S. Medvedev, *et al.*, *Nature Materials* **8**, 630 (2009). 44, 45

[93] N. C.Gresty, *et al.*, *Journal of the American Chemical Society* **131**, 16944 (2009). 44, 45, 51

[94] Z. Xu, *et al.*, *Physical Review B* **84**, 052506 (2011). 45

[95] J. Wen, *et al.*, *Physical Review B* **80**, 104506 (2009). 45, 66

[96] T. J. Liu, *et al.*, *Physical Review B* **80**, 174509 (2009). 45, 46

[97] A. S. Pine, G. Dresselhaus, *Physical Review B* **4**, 356 (1971). 47, 54

[98] A. S. Pine, G. Dresselhaus, *Physical Review B* **5**, 4078 (1972). 47, 54

[99] P. Kumar, *et al.*, *Solid State Communications* **150**, 557 (2010). 47, 48

[100] Z. Qin, *et al.*, *Solid State Communications* **150**, 768 (2010). 47, 48

[101] V. Gnezdilov, *et al.*, *arXiv* **1301**, 1960v1 (2013). 47, 48, 53

[102] V. Gnezdilov, *et al.*, *Physical Review B* **83**, 245127 (2011). 48, 49, 53, 57

[103] K. Okazaki, *et al.*, *Physical Review B* **83**, 035103 (2011). 48, 49, 53

[104] C. S. Lopes, *et al.*, *Superconductor Science and Technology* **25**, 025014 (2012). 48, 49

[105] A. Tamai, *et al.*, *Physical Review Letters* **104**, 097002 (2010). 51

[106] M. Rahlenbeck, *et al.*, *Physical Review B* **80**, 064509 (2009). 53, 64, 85, 86, 100, 103, 105, 111, 112

[107] K. Y. Choi, *et al.*, *J Phys Condens Matter* **22**, 115802 (2010). 53, 64, 85, 100, 103, 106, 107, 111, 112

[108] A. Litvinchuk, *et al.*, *Physical Review B* **84**, 092504 (2011). 53, 64, 106, 112

[109] Y. Um, *et al.*, *Physical Review B* **85**, 012501 (2012). 53, 64, 99

[110] L. Zhang, *et al.*, *Physical Review B* **79**, 012506 (2009). 62

[111] L. Boeri, *et al.*, *Physical Review B* **82**, 020506 (2010). 63

[112] T. Fukuda, *et al.*, *Physical Review B* **84**, 064504 (2011). 63

[113] S. Hahn, *et al.*, *Physical Review B* **79**, 220511 (2009). 63

[114] D. Reznik, *et al.*, *Physical Review B* **80**, 214534 (2009). 63

[115] L. Chauviere, *et al.*, *Physical Review B* **80**, 094504 (2009). 64, 85, 111

[116] N. Ni, *et al.*, *Physical Review B* **78**, 014523 (2008). 64

[117] N. Ni, *et al.*, *Physical Review B* **78**, 014507 (2008). 64

[118] A. Akrap, *et al.*, *Physical Review B* **80**, 180502 (2009). 64

[119] A. V. Boris, *et al.*, *Physical Review Letters* **102**, 027001 (2009). 64

[120] M. Mansson, *private communication*. 64

[121] Y. Gallais, *et al.*, *Physical Review B* **78**, 132509 (2008). 64, 105, 112

[122] R. Juza, K. Z. Langer, *Zeitschrift für Anorganische und Allgemeine Chemie* **361**, 58 (1968). 70

[123] X. C. Wang, *et al.*, *Solid State Communications* **148**, 538 (2008). 70, 74

[124] M. J. Pitcher, *et al.*, *Chemical Communications* p. 5918 (2008). 70

[125] M. J. Pitcher, *et al.*, *Journal of the American Chemical Society* **132**, 10467 (2010). 70, 74, 75

[126] A. S. Sefat, *et al.*, *Physical Review B* **78**, 104505 (2008). 71

[127] M. Rotter, *et al.*, *Physical Review B* **78**, 020503 (2008). 71

[128] Y. J. Song, *et al.*, *Applied Physics Letters* **96**, 212508 (2010). 71, 79, 96

[129] D. J. Singh, *Physical Review B* **78**, 094511 (2008). 71, 72

[130] S. Borisenko, *et al.*, *Physical Review Letters* **105**, 067002 (2010). 71, 72, 74, 76

[131] A. Kordyuk, *et al.*, *Physical Review B* **83**, 134513 (2011). 71, 78, 82, 83, 86

[132] K. Umezawa, *et al.*, *Physical Review Letters* **108**, 037002 (2012). 71, 76, 77

[133] C. Putzke, *et al.*, *Physical Review Letters* **108**, 047002 (2012). 71

[134] Z. Li, *et al.*, *Physical Review B* **80**, 092503 (2009). 71, 72, 73

[135] M. Wang, *et al.*, *Physical Review B* **83**, 220515 (2011). 73, 74

[136] Y. F. Li, B. G. Liu, *The European Physical Journal B* **72**, 153 (2009). 71, 72

[137] P. Jeglic, *et al.*, *Physical Review B* **81**, 140511 (2010). 74

[138] L. Ma, *et al.*, *Physical Review B* **82**, 180501 (2010). 74

[139] L. W. Harriger, *et al.*, *Physical Review B* **84**, 054544 (2011). 74

[140] M. Gooch, *et al.*, *Europhysics Letters* **85**, 27005 (2009). 75

[141] S. Zhang, *et al.*, *Physical Review B* **80**, 014506 (2009). 75

[142] D. S. Inosov, *et al.*, *Physical Review Letters* **104**, 187001 (2010). 76

[143] U. Stockert, *et al.*, *Physical Review B* **83**, 224512 (2011). 76

[144] Y. Imai, *et al.*, *Journal of the Physical Society of Japan* **80**, 013704 (2011). 76

[145] H. Kim, *et al.*, *Physical Review B* **83**, 100502 (2011). 76

[146] Z. Li, *et al.*, *Journal of the Physical Society of Japan* **79**, 083702 (2010). 76

[147] S. V. Borisenko, *et al.*, *Symmetry* **4**, 251 (2012). 77

[148] T. Hänke, *et al.*, *Physical Review Letters* **108**, 127001 (2012). 77

[149] P. M. R. Brydon, *et al.*, *Physical Review B* **83**, 060501 (2011). 77

[150] K. Mydeen, *et al.*, *Physical Review B* **82**, 014514 (2010). 77

[151] Z. Deng, *et al.*, *Europhysics Letters* **87**, 37004 (2009). 77

[152] B. Li, *et al.*, *Applied Physics Letters* **98**, 072506 (2011). 78, 85

[153] C. Marini, *et al.*, *Europhysics Letters* **84**, 67013 (2008). 81, 99

[154] A. P. Litvinchuk, *et al.*, *Physical Review B* **78**, 060503 (2008). 81, 85, 99, 105

[155] Y. J. Um, *et al.*, *Physical Review B* **85**, 064519 (2012). 81, 85, 99, 100, 103

[156] G. Chen, *et al.*, *Physical Review Letters* **102**, 227004 (2009). 90, 92

[157] C. W. Chu, *et al.*, *Physica C: Superconductivity* **469**, 326 (2009). 90

[158] S. Li, *et al.*, *Physical Review B* **80**, 020504 (2009). 90, 91, 93

[159] K. Kusakabe, A. Nakanishi, *Journal of the Physical Society of Japan* **78**, 124712 (2009). 91, 92

[160] C. He, *et al.*, *Physical Review Letters* **105**, 117002 (2010). 91, 92, 93, 104

[161] Z. H. Liu, *et al.*, *Physical Review B* **84**, 064519 (2011). 92, 95, 96, 107

[162] S. Thirupathaiah, *et al.*, *Physical Review B* **86**, 214508 (2012). 92, 95, 96

[163] M. Yi, *et al.*, *New Journal of Physics* **14**, 073019 (2012). 92

[164] J. D. Wright, *et al.*, *Physical Review B* **85**, 054503 (2012). 93

[165] L. Ma, *et al.*, *Physical Review B* **83**, 132501 (2011). 93

[166] Q. Huang, *et al.*, *Physical Review Letters* **101**, 257003 (2008). 93

[167] K. Kaneko, *et al.*, *Physical Review B* **78**, 212502 (2008). 93

[168] X. Zhou, *et al.*, *Physical Review Letters* **109**, 037002 (2012). 93, 94, 95, 96, 103, 104, 106

[169] M. A. Tanatar, *et al.*, *Physical Review B* **85**, 014510 (2012). 94, 104

[170] N. Spyrison, *et al.*, *Physical Review B* **86**, 144528 (2012). 94, 104

[171] S. J. Zhang, *et al.*, *Europhysics Letters* **88**, 47008 (2009). 94

[172] A. F. Wang, *et al.*, *New Journal of Physics* **14**, 113043 (2012). 94

[173] H. Yang, *et al.*, *Physical Review B* **86**, 214512 (2012). 94

[174] S. Oh, *et al.*, *arXiv* **1302**, 1429v1 (2013). 95, 96

[175] A. F. Wang, *et al.*, *Physical Review B* **85**, 224521 (2012). 95, 96, 107

[176] S. Y. Zhou, *et al.*, *Europhysics Letters* **101**, 17007 (2013). 96

[177] K. Cho, *et al.*, *Physical Review B* **86**, 020508 (2012). 96

[178] K. Y. Choi, *et al.*, *Physical Review B* **78**, 212503 (2008). 100, 103

[179] R. M. Fernandes, *et al.*, *Physical Review B* **85**, 024534 (2012). 104

[180] A. F. Wang, *et al.*, *arXiv* **1207**, 3852v3 (2012). 104

[181] B. Li, *et al.*, *Journal of Applied Physics* **111**, 033922 (2012). 104

[182] I. I. Mazin, *et al.*, *Physical Review B* **82**, 180502 (2010). 107, 108

Acknowledgements

I am the vine; you are the branches. If a man remains in me and I in him, he will bear much fruit; apart from me you can do nothing. John 15:5

I thank my Lord. I believe I am in you, and I supplicate you are in me.

I would like to express my deepest gratitude to all those who supported and encouraged me during my PhD thesis. Without supports of many people in many places, this thesis could not have been possible.

I am very grateful, first of all, for my family: my beloved wife Myeongsook Kim who encouraged me, my two children Yejee Um and Jihoon Um, my parents, parents-in-law, and my sister and her husband for supporting me in every possible way they could.

I am also grateful to Prof. Harald Giessen and Prof. Alejandro Muramatsu being a committee members of my thesis.

It was a great pleasure working with our Raman group members: Armin Schulz for his technical support and careful assistance during the Raman experiments, and Dr. Mohammed Bakr, Dr. Santiago Blanco Canosa, Dr. Martin Rahlenbeck, Michaela-Sofia Souliou, Nadir Driza and Matthias Hepting for many informative discussions and experimental assistance.

I am thankful to all of my collaborators: Dr. Lilia Boeri and Dr. Alaska Subedi at MPI for phonon calculation, Christof Busch for EDX measurement, Prof. Yong Seung Kwon, Dr. Byeong Hun Min and Dr. Yoo Jang Song at DGIST Korea and Sungkyunkwan University, Dr. Pierre Toulemonde, Dr. S. J. E. Carlsson and Dr. André Sulpice at CNRS, Prof. Matthew Rosseinsky and Dr. Alexey Ganin at University of Liverpool,

Dr. Chengtian Lin and Dr. Yong Liu at MPI for providing me with high-quality single crystals. Especially, I am very grateful for all crystal growers, as without good crystals my measurement could not be carried out.

I thank all our group members: Dr. Giniyat Khaliullin, Dr. George Jackeli, Dr. Jungwha Kim, Dr. Hoyoung Jang, Dr. Aliaksei Charnukha, Dr. Darren Peets, Dr. Jitae Park, Dr. Alex Fraño Pereira, Gerd Friemel, Toshinao Loew, Meng Wu, Daniel Pröpper for friendship and a great time together, and Heiko Uhlig for technical support. In particular, I am thankful to my office mates Ayman Akil and Christopher Dietl for funny stories, useful discussions and good mood.

I have pretty enjoyed talking to my Japanese friend Kazuhiro Kawashima who started carrier together with me.

I am grateful to Korean friends at the MPI for their personal support to my family and interesting scientific discussions and advices, Korean Christians at Korean evangelical mission community in Stuttgart.

I would like to thank to our secretary Mrs.Sonja Balkema and Mrs.Birgit King for helping with administrative tasks, and I would also like to acknowledge the European project SOPRANO, which provided me with two years of financial support.

Finally, I owe my biggest debt of gratitude to my two supervisors: Prof. Bernhard Keimer who encouraged me in my scientific motivation in high T_c superconductors and gave the opportunity to carry out my PhD research in his group, and Dr. Mathieu Le Tacon who supervised Raman spectroscopy as well as other experimental activities, for fruitful physical discussions and correcting my poor English grammar. Without them, none of this would be possible.